ISBN 978-82-326-2848-3 (printed version)
ISBN 978-82-326-2849-0 (electronic version)
ISSN 1503-8181

Doctoral theses at NTNU, 2018:17

Ctirad Sousedik

Presentation Attack Resistant Fingerprint Biometrics

using Optical Coherence Tomography

Doctoral Thesis

Ctirad Sousedik

Doctoral theses at NTNU, 2018:17

NTNU

Norwegian University of Science and Technology

NTNU
Norwegian University of Science and Technology
Faculty of Information Technology and Electrical Engineering
Department of Information Security and Communication Technology

NTNU

Norwegian University of Science and Technology

Ctirad Sousedik

Presentation Attack Resistant Fingerprint Biometrics

using Optical Coherence Tomography

Thesis for the degree of Philosophiae Doctor

Gjøvik, January 2018

Norwegian University of Science and Technology
Faculty of Information Technology
and Electrical Engineering
Department of Information Security and Communication
Technology

NTNU
Norwegian University of
Science and Technology

NTNU
Norwegian University of Science and Technology

Thesis for the degree of Philosophiae Doctor

Faculty of Information Technology
and Electrical Engineering
Department of Information Security and Communication
Technology

ISBN 978-82-326-2848-3 (printed version)
ISBN 978-82-326-2849-0 (electronic version)
ISSN 1503-8181

Doctoral theses at NTNU, 2018:17

Printed by Skipnes Kommunikasjon as

Kites rise highest against the wind, not with it.

(Winston Churchill)

Declaration of Authorship

I, Ctirad Sousedik, hereby declare that this thesis and the work presented in it is entirely my own. Where I have consulted the work of others, this is always clearly stated.

Signed:

(Ctirad Sousedik)

Date:

Preface

Fingerprints are one of the best investigated biometric characteristics with a long history of person identification regarding law enforcement. A wide range of automated fingerprint sensing and recognition solutions exist, reliable in terms of identification of individuals.

However, the existing solutions still suffer from significant weaknesses regarding the problem of detecting artefact fingerprint representations, which greatly limit their applicability for unsupervised identification scenarios such as automated border control.

In this thesis, we investigated Optical Coherence Tomography as a novel scanning technology for fingerprint sensing, with the aim of developing a fingerprint sensor that is very difficult to deceive with artefact fingerprints and as such would offer a solution to the problem.

Acknowledgments

I would like to thank my supervisor Christoph Busch for providing an exceptional opportunity for personal growth. I would also like to thank my co-supervisor Patrick Bours for help and support with the thesis. Very importantly, I would like to thank Ralph Breithaupt for the opportunity to work on this exciting topic and broaden my range of technical and scientific skills. Many thanks also to the many volunteers, willing to provide their data as scanned with our OCT fingerprint scanner prototype.

Contents

List of Figures

List of Tables

List of Algorithms

Chapter 1

Introduction

1.1 Motivation

In the recent years, biometrics are on the rise as a convenient alternative authentication mechanism. Unlike passwords, which can be easily forgotten, and access cards or keys, which can be easily lost, biometrics provide a means of authentication that is always readily available.

Among the many existing biometric modes, such as iris, face, retina and others, fingerprint stands among the best known and most widely applied.

However, despite the three-decade-long history, fingerprint sensing solutions still struggle with a number of challenges, which limit their applicability especially for unsupervised scenarios such as border control:

- Worn out fingers - For persons whose fingertip skin has been subjected to a lot of stress, the fingerprint can be abraded or significantly damaged (guitar players, construction workers, chemists etc.)
- Wet or greasy fingers - liquids on the surface of the fingerprint tend to diffuse into the fingerprint valleys when the finger is pushed against the sensor surface, which makes the acquisition difficult
- Dry fingers - If the fingerprint skin is too dry, it does not come into good contact with the fingerprint sensor surface, which results in low quality
- Infant fingerprints - the fingerprint skin of infants is very soft and fine, and if pressed against a sensor surface, the fingerprint pattern will not be observable, unless specialized solutions are employed [53, 59] - this limits the usage of fingerprinting in fight against child trafficking

Similarly to other biometric modes, a significant challenge comes also with the susceptibility of fingerprinting to spoofing attacks [81, 102].

A large body of research exists addressing this challenge of Presentation Attack Detection (PAD) for 2D fingerprint sensors. However, no single solution as of yet provides for a good level of security, especially considering resistance against novel materials and production techniques regarding the artefact fingerprints [102]. The existing approaches in the industry typically focus on combining a larger number of additional single-purpose sensors and features extracted from the 2D image to take the PAD decision. Considering

the variability of properties of genuine human fingers, this requires machine learning approaches, which inherently depend on the training data, and as such are vulnerable against novel approaches not considered before [102].

1.1.1 OCT fingerprinting

Due to the above mentioned shortcomings of the existing fingerprint sensors, the community has been looking for an alternative solution.

A promising path is offered by the Optical Coherence Tomography (OCT). The OCT is a light-beam-based scanning technology that is capable of penetrating the fingerprint skin up to the depth of 2-3mm and acquiring a 3D volumetric representation of the surface fingerprint along with the sub-surface structure. Contact with a surface is not necessary, and as such many of the challenges such as dry, wet, greasy or infant fingers can be easily overcome. In addition, the OCT is able to spot a second representation of the fingerprint in the subsurface data - the master template responsible for the stability of fingerprint during a person's lifetime. In addition to the inner fingerprint, presence of which could readily be used for the PAD purposes, the OCT is also able to spot sweat glands - fine spiral structures which end as sweat pores on the surface on the fingers. And last but not least, the volumetric measurements from the OCT readily provide a general scattering profile of the underlying material.

However, along with the significant promise, a rather significant challenge comes also associated with the step up from 2D to 3D scanning. The amounts of data generated by the OCT are very significant, and require novel scanning and processing approaches in order to achieve the practical speeds of a few seconds as required by many applications, such as border control.

1.2 Research goals

The main goal of this research was to progress towards an OCT-based fingerprint sensor, capable of robustly distinguishing between fake and genuine fingerprints - equipped with a reliable Presentation Attack Detection (PAD). Such a capability would allow for the application of fingerprints in unsupervised scenarios, allowing for convenient and secure usage of the OCT fingerprinting for automatic border control, considering that fingerprint scans are among the mandatory information stored in the current standard electronic passports. The main questions addressed in this research are focused on the challenges of handling the transition from 2D fingerprint scans to 3D volumetric fingerprint imaging, along with the associated massive increase in the amount of data to be processed:

- How can the fingerprints from the surface (outer fingerprint) and from underneath the skin surface (inner fingerprint) be reliably extracted in

a matter of a few seconds from a volumetric OCT scan of size that can easily reach multiple GB ?

- Is the inner fingerprint from underneath the skin surface consistently present in the capture subjects, considering the variations in the population?
- Would the ability to scan the inner fingerprint allow to perform fingerprint identification in case of damaged/abraded outer fingerprints?
- Can the sweat glands, visible as spiral structures in high-resolution volumetric OCT fingerprint scans, be detected in a matter of a few seconds given the amounts of data to be analyzed?
- What are the differences between the amount of sweat glands, their size, shape and other properties, considering the variations in the population?
- Is the massively-parallel processing on GPUs suitable in order to address the challenge of handling large amounts of volumetric fingerprint OCT data?

1.3 Contributions

The main contributions of the thesis are the following:

- An innovative approximate technique for 1D narrow cluster detection is proposed and utilized to detect the positions of the fingerprint on the surface and the second fingerprint underneath the skin surface on partial fingerprint OCT scans. Metrics for identification of unsuccessful acquisition of a partial fingerprint OCT scan due to excessive shaking or lifting the finger too early are proposed.
- A proof of concept of a specific-purpose OCT fingerprint sensor, developed in the BSI project OCT-Finger-II [12] in parallel with the research described in this thesis, has been significantly improved in the framework of this thesis. By exchanging multiple electronic and optical components, the scanning quality has been significantly improved. In addition, the scanning quality and stability of the design has been further improved by a full re-design and re-write of the control & visualization software.
- A 6.6TB dataset of 3D OCT scans of size 1024x1408x1408 voxels from 720 fingers - 72 capture subjects, all ten fingers - has been collected. In addition, from a sub-set of 50 capture subjects, 2D fingerprints acquired by standard 2D fingerprint sensors have been collected, in order to allow for testing of compatibility between the OCT and the standard 2D fingerprinting.

- A novel technique for filter-size independent single-pass approximate Gaussian filtering has been proposed. In addition, a technique for fast filter-size-independent implementation of edge detection filters has been proposed.
- Using the above mentioned fast filter-size-independent edge detection filter as a building block, a GPU-based pipeline for extraction of the fingerprints from the OCT volumetric scan has been proposed. The method is able to extract the fingerprint from the skin surface (outer fingerprint) as well as from underneath the skin surface (inner fingerprint) in less than 1s on modern GPUs. The applicability of the extracted fingerprints, as well as their compatibility with standard 2D fingerprint sensors, is tested by cross-comparison between the OCT extracted fingerprints and the standard 2D fingerprints.
- Utilizing the above mentioned approximate fast filter-size-independent Gaussian filtering technique, an approach for fast filter-size-independent filtering with the 3D Difference of Gaussians (DoG) operator on the volumetric data is proposed, both for the CPU and the GPU scenario. The proposed novel approach allows to calculate 3D DoG with a very small memory footprint suitable for the processing on GPUs.
- The above mentioned GPU-based 3D DoG filtering pipeline together with the above mentioned fingerprint extraction pipeline is used to propose a sweat glands candidate detector from underneath the fingerprint surface.

1.4 Thesis structure

This thesis is structured as follows. Chapter 2 contains a survey of the existing methods for distinguishing between genuine and fake fingerprints (PAD), both as based on additional analysis of standard 2D fingerprint scans as well as based on addition of extra single-purpose sensors. Chapter 2 discusses the weaknesses of these approaches, especially against novel, previously unknown, artifact fingerprints, and suggests OCT fingerprinting as a possible solution. In Chapter 3, methods for segmentation of the OCT scans taken from a partial fingerprint area are proposed along with quality metrics for detection of non-compliant capture subject behavior, such as lifting the fingers too early, excessive shaking, etc. Chapter 4 describes the specific-purpose OCT fingerprint sensor, significantly improved in terms of scanning quality and stability in terms of this research by exchange of multiple electronic and optical components and a full re-design and re-write of the control & visualization software. Chapter 4 also describes the dataset collected with the improved OCT fingerprint scanner. Chapter 5 proposes the fast approximate filter-size-independent single-pass Gaussian filtering technique, utilized later on for sweat-glands detection based on 3D Difference of Gaussians (DoG).

Chapter 5 also proposes a fast filter-size-independent technique for edge detection, which is later utilized for extraction of the fingerprints from the volumetric fingerprint OCT scans. Chapter 6 describes the proposed method for extraction of outer and inner fingerprints from a volumetric OCT scan. The proposed method is tested by cross-comparison of the extracted OCT fingerprints with standard 2D fingerprints. Chapter 7 describes the proposed novel 3D DoG filtering approach with small memory footprint and its application for detection of sweat glands. Finally, Chapter 8 offers conclusions and ideas for future work.

1.5 Publication list

The material in this thesis is based on the following papers:

SOUSEDIK, C., AND BUSCH, C. Presentation attack detection methods for fingerprint recognition systems: a survey. *IET Biometrics 3*, 4 (2014), 219–233

SOUSEDIK, C., BREITHAUPT, R., AND BUSCH, C. Volumetric fingerprint data analysis using Optical Coherence Tomography. In *International Conference of the Biometrics Special Interest Group (BIOSIG)* (2013), p. 16

SOUSEDIK, C., AND BUSCH, C. Quality of fingerprint scans captured using optical coherence tomography. In *IEEE International Joint Conference on Biometrics* (Sept 2014), pp. 1–8

BREITHAUPT, R., SOUSEDIK, C., AND MEISSNER, S. Full fingerprint scanner using optical coherence tomography. In *Biometrics and Forensics (IWBF), 2015 International Workshop on* (March 2015), pp. 1–6

SOUSEDIK, C., AND BREITHAUPT, R. Full-fingerprint volumetric subsurface imaging using fourier-domain optical coherence tomography. In *Biometrics and Forensics (IWBF), 2017 International Workshop on* (2017)

SOUSEDIK, C., BREITHAUPT, R., AND BOURS, P. Classification of fingerprints captured using optical coherence tomography. In *Scandinavian Conference on Image Analysis (SCIA), 2017* (2017)

Chapter 2

State of the Art

2.1 Summary

This chapter, based on an updated version of the paper by Sousedik & Busch [102], discusses the state-of-the-art in fingerprint Presentation Attack Detection (PAD), with a special focus on PAD applications of Optical Coherence Tomography (OCT). It discusses the strengths & weaknesses of the existing approaches and suggests the OCT as a promising research direction regarding fingerprint PAD.

2.2 Introduction

For over a century now, fingerprints have been widely used as a biometric characteristic by forensic sciences. Nowadays, large national and international databases contain millions of records, at disposal of forensic investigations and migration control. Fingerprints are also being used for access control concerning security sensitive environments such as access to protected facilities or sensitive data. Recently, fingerprint recognition systems have been deployed as access control to rather common facilities like recreation areas, fitness-centres, etc. Fingerprint capture devices are widely available on the market, which provides for a variety of applications.

The fingerprint is a well-known biometric characteristic, which is valued for its uniqueness even in cases of identical twins [46]. No other biometric characteristic has probably been so well tested in real-world situations for such a long time. State-of-the-art automatic fingerprint recognition algorithms perform with high recognition accuracy on databases containing hundreds of millions of records.

Nevertheless, the state-of-the-art fingerprint sensors can be a significant security problem. Even though the current comparison algorithms are very mature in terms of searching records for an appropriate match, the entire system can be spoofed by an accurate imitation of the ridge/valley structure of the fingertip, which could have for instance been generated with low cost resources from the signal that has been derived from a latent fingerprint [36, 38, 41, 57, 73, 108, 111, 116].

Numerous approaches to solve the problem of liveness detection for fingerprint sensors have been published. The hardware-based solutions suggest

a new sensing technology, which would be difficult to deceive due to the nature of the fingerprint capture process. The software-based methods on the other hand try to use data that can be obtained from currently existing sensors, and add a software liveness detection module. Although the software methods do have limited possibilities due to the fixed hardware, they also have the advantage of lower costs that are limited to the deployment costs of a software update.

Another possible way of deceiving the fingerprint sensor is the fingerprint alterations. The impostor alters or damages his fingerprint pattern in order to avoid automatic identification based on his enrolled fingerprints. The Fingerprint Alteration Detection along with Liveness Detection belong to the group of Presentation Attack Detection (PAD) methods (Fig. 2.3).

2.3 Fingerprint sensing technologies

Numerous principles have been utilized in order to develop a sensor capable of capturing the ridge/valley structure of a fingerprint. The fingerprint sensing technologies can be divided into two groups as illustrated by Fig. 2.1.

The technologies that belong to the optical sensor group generally utilize a system of light sources, lens, prisms or optical fibres along with a photosensitive surface to capture the fingerprint pattern. The solid state sensors are usually developed as a single chip solution, where the sensing mechanism is integrated on the silicon chip. Typically, solid state sensors can be produced in smaller sizes than optical sensors, yielding the possibility of integration into portable devices. Alternatively, the fingerprint sensing technologies can be classified into "swipe", "touch", and "touchless" categories. The swipe sensors require the biometric capture subjects to swipe their finger over the sensor surface. The fingerprint is captured from the time-series acquired. Although this approach can lead to higher failure-to-acquire (FTA) rates, it allows the sensor area to be of much smaller size than that of the touch sensors, which can reduce the production costs. The touch sensors provide a sensor surface large enough to capture the fingerprint using a single static scan. The touchless sensors do not require the capture subject to press his finger against a flat surface. The fingerprint is scanned in its original condition. These sensors do not suffer from problems of touch-based sensors, such as skin deformation, latent fingerprints on the surface or hygienic issues [60].

One of the first fingerprint sensing technologies has been the Frustrated Total Internal Reflection (FTIR). The technology utilizes a prism, a LED light source, and a CCD/CMOS camera as illustrated by Fig. 2.1(a). The finger is put onto the prism surface and another side of the prism is illuminated by the LED light source. Fingerprint ridges that are in contact with the prism surface absorb the light, while the surface under the valleys reflects the light towards the CCD/CMOS camera. This way of the fingerprint surface analysis makes it difficult to deceive the sensor with a fake 2D representation of the fingerprint

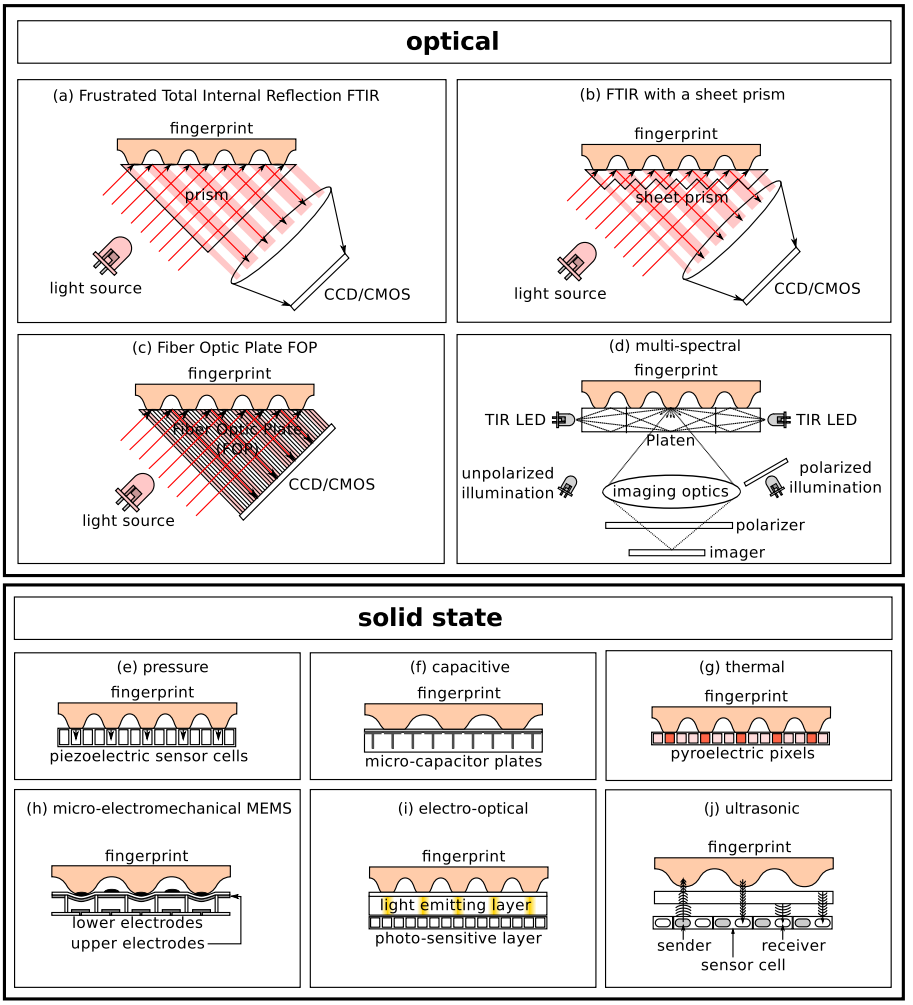

Figure 2.1: Fingerprint sensing technologies [78, 95, 96]

such as a photo [63, 78].

The FTIR technology suffers from disadvantages of larger size, particularly due to the presence of the prism. In order to solve this problem, the sheet prism FTIR technology replaces the single large prism with a large number of small adjacent prisms as illustrated by Fig. 2.1(b). This approach reduces the size of the sensors, however, it also somewhat reduces the final image quality [63, 78].

Another way of dealing with the size constraints caused by the presence of the prism is the Fiber Optic Plate (FOP) method. In this case, the single large prism from the classical FTIR design is replaced with a grid of optical fibres

as shown by Fig. 2.1(c). The fingerprint ridges are in contact with the optical fibres, and scatter the light emitted by a LED light source. The optical fibres under the valleys reflect the light to a CCD/CMOS photosensitive surface [63, 78].

A relatively new approach to fingerprint sensing is the multi-spectral technology (Fig. 2.1(d)). This technology enables capturing of multiple images of the fingertip under various illumination conditions, as regards the wavelength, orientation, and polarization of the light emitted. The captured images depict the fingertip at various depths and with variations depending on the different absorption of the individual wavelengths in the fingertip [95]. The aggregative analysis of these images improves FTA rates of the sensor in difficult conditions (dirty fingers, damaged surface fingerprint).

In contrast to the optical technologies, the solid state fingerprint sensors (Fig. 2.1) can typically be integrated in a single chip, decreasing the resulting size and costs.

The pressure based fingerprint sensors are based on the piezoelectric effect. Piezoelectric materials produce small amounts of voltage when pressure is applied. The sensing technology makes use of a grid of piezoelectric cells that yield different amount of voltage depending on whether or not they are in contact with the ridges on the fingertip surface. From the differences, the fingerprint pattern can be captured (Fig. 2.1(e)) [78].

The capacitive fingerprint sensing technology utilizes a grid of micro capacitor plates. The finger that is put onto the sensor acts as a second plate for each of the micro capacitors. The ridges that are in closer contact with the surface yield different resulting capacitance than the valleys. Using these differences, the fingerprint pattern is captured (Fig. 2.1(f)) [63, 78].

The thermal technology utilizes a 2D array of thermo-sensitive cells made of pyroelectric materials. When the finger is put onto the sensor, the fingerprint pattern is captured as it depends on the temperature differences between the ridges and the air in the valleys (Fig. 2.1(g)) [63, 78].

Another approach that has been based on the pressure differences between ridges and valleys of a fingerprint is the micro-electromechanical (MEMS) technology. The sensor consists of a 2D sensor cell array as illustrated by Fig. 2.1(h). If the fingerprint ridge is put on a sensor cell, the upper electrode is pushed down causing capacitance change of the cell capacitor. The differences between capacitance of the cell capacitors under the ridges and valleys are used to obtain the fingerprint pattern (Fig. 2.1(h)) [96].

The electro-optical technology makes use of a photosensitive layer and a light emitting layer as shown by Fig. 2.1(i). The light emitting layer emits light based on electric potential on its surface. Since the fingerprint ridges touch the surface and the valleys do not, the electric potential varies across the surface, generating a fingerprint representation that is captured by the photosensitive layer [63].

In the ultrasonic fingerprint sensing technology, the differences of the acoustic impedance between the ridge skin and the air in the valleys are utilized in

order to capture a fingerprint pattern. The acoustic signal is transmitted towards the fingertip surface, and the reflected echo is captured to reproduce the ridge/valley structure. This acoustic technology is also capable of analysing sub-surface layers of the skin, enabling lower FTA rates (Fig. 2.1(j)) [78].

The radio frequency technology analyses changes of the electromagnetic field of the radio frequencies due to the presence of the fingertip. Every cell of the detector grid acts like a micro antenna and detects variations due to presence of the fingerprint pattern. The technology can analyse also sub-surface information in the fingertip, yielding better functionality in difficult conditions [78].

A summary of the design properties of the above discussed fingerprint sensing technologies is provided by the Tab. 2.1.

2.4 Fingerprint sensor spoofing methods

In general, the fingerprint spoofing methods can be divided into two classes. If the actual finger of the genuine enrolled individual is available during the fake[1] fabrication process, the fabrication methods are called "cooperative" [9, 41, 112] or "direct casts" [36, 37, 38]. On the other hand, if the original finger is not directly available, the methods are called "non-cooperative" [9, 41, 112] or "indirect casts" [36, 37, 38]. It is worth noting that these terms can be somewhat misleading because the methods either do or do not require the original finger to be present during the fake finger fabrication process. It is not important in what manner the original finger was available - it could be possible to get physical control of the original finger by means of violence, drugs, blackmailing, etc. Fig. 2.2 summarizes various fingerprint faking approaches.

The "direct casting" methods make use of the availability of the original finger to create a fake fingerprint. The fake fingerprint is created by means of a mould made of materials like thermoplastic [36, 38], silicone [36, 38], plasticine [111], candle wax [111], etc. The mould material needs to be sufficiently soft so that the original finger can be pressed against it to create a negative of the original fingerprint. The finger needs to be pressed against the mould in a very careful fashion so that all of the fingerprint details are being preserved and lifted back; and the mould needs to be able to harden, providing the negative for the fake fingerprint fabrication. Afterwards, the actual fake finger is created using the mould. Various materials like latex [36, 38], silicone [41, 57, 108, 111], gelatin [57, 73], etc. are possible to use, but it is necessary to take the mould material into consideration as well. The mould and fake fingerprint material must not join together during the fake fingerprint hardening process, neither must they chemically react so that the quality of the resulting finger would be impaired. It must also be possible to remove the hardened

[1] In the International Standardisation project ISO/IEC 30107, instead of the term fake, the term artefact is defined as follows: artificial object or representation presenting a copy of biometric characteristics or synthetic biometric patterns.

Table 2.1: Fingerprint sensing technologies [78, 95, 96]

type	sensing method	
optical miniaturization limitations	FTIR	larger size due to the prism and optics
	FTIR with a sheet prism	more compact, reduced prism size
	Fiber Optic Plate	compact design, prism and optics replaced by optical fibers
	multi-spectral	multi-spectral scanning, better functionality in difficult conditions
	electro-optical	measurement of difference in electric potential caused by the fingerprint pattern
solid state single-chip design	radio frequency	measures changes in electromagnetic field in the fingertip, better functionality in difficult conditions
	capacitive	capacitance measurement, susceptible to electrostatic discharge
	ultrasonic	measures acoustic impedance of the ridges and the air in the valleys
	pressure	measurement of pressure caused by the ridges using the piezoelectric effect
	micro-electromechanical	measurement of pressure caused by the ridges by the capacitance change in cell capacitors
	thermal	measures temperature of ridges and valleys air, environment-dependent

fake fingerprint from the mould without having bits of the mould stuck in the resulting 3D fingerprint pattern [111].

The "indirect casting" methods take advantage of other ways how to obtain the fingerprint pattern indirectly. Latent fingerprints left by the genuine enrolled individual on various surfaces can be exploited. Initially, it is necessary to visualize the latent fingerprint, since it is not directly visible in most cases. Various methods to perform this visualization step are known from

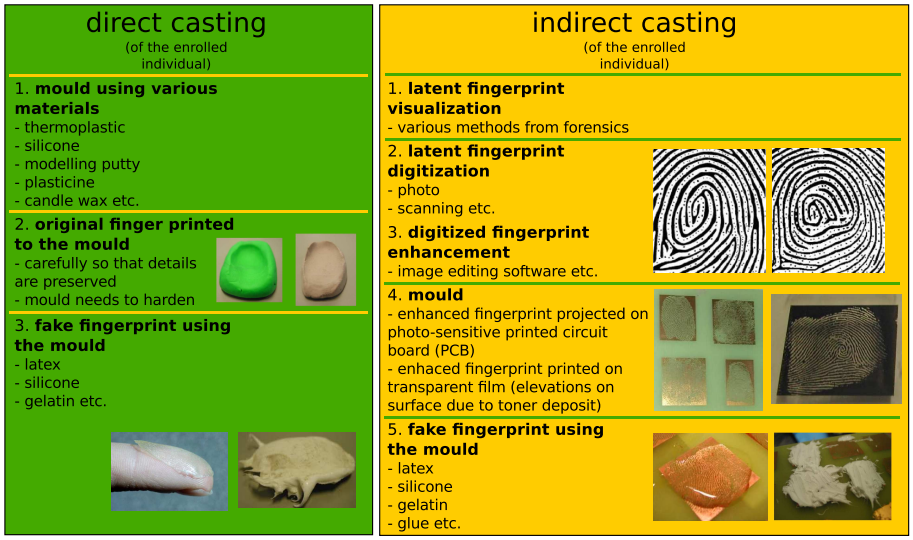

Figure 2.2: Fingerprint sensor spoofing methods [36, 38, 41, 57, 73, 108, 111]

forensics. One of the methods is application of very fine-grained powders on the latent fingerprint. The powder sticks to the latent fingerprint and the rest of the powder that did not get stuck can be gently removed. In such way, the latent fingerprint becomes clearly visible and can even be lifted off the surface by using special tape that glues the visualized fingerprint on its surface. The visualized latent fingerprint is then digitized by means of photographing or scanning and digitally enhanced in order to compensate for the loss of quality that is present due to the usage of latent fingerprints. The digitized fingerprint is also converted to black and white mask that is used in further steps. Afterwards, the mask is printed on a thin transparent film. It is possible to use this film directly as a mould because the toner deposit creates elevations on the surface of the film [36, 38, 111]. Alternatively, the mould can be created using printed circuit board (PCB) technology. The film with the fingerprint on-print is put on the PCB and illuminated with UV light. The parts of the PCB exposed to the UV light can be then etched away in order to create a mould with the fingerprint pattern [41, 73, 108, 111]. Finally, the fake fingerprint is created using the film or the etched PCB as a mould. Various materials are possible to use, such as latex [36, 38], silicone [41, 108, 111] gelatin [73, 111], plasticine [111], wood cement [111], glue [36, 38], etc. The material is put in the mould and after hardening, the fake fingerprint is removed from it and ready to use.

In addition to the above mentioned group of methods, the mould for the fake fingerprint or the fake fingerprint itself can be produced by any other means that can provide for sufficient detail (ordered rubber stamp, 3D printers, etc). The range of possible fake fabrication materials is rather large and

difficult to predict, which poses a great challenge on finding an effective countermeasure.

2.5 Presentation Attack Detection for fingerprint sensors

In order to satisfy security requirements for a biometric fingerprint recognition system, it should not be possible to deceive a fingerprint sensor. The sensor should reject any fake fingers created from any material as well as a dead cut-off finger. In addition to usage of fake or cut-off fingers, the impostors can change their fingerprint patterns so that they would be able to escape their identification in terms of the fingerprint identification pipeline. Ideally, the sensor should be equipped with a Presentation Attack Detection (PAD) capability in order to correctly handle the above mentioned impostor scenarios. As illustrated by Fig. 2.3, the PAD methods for fingerprints include Liveness Detection and Fingerprint Alteration Detection. The term PAD is defined by the standardization project, ISO/IEC 30107 [50], and, in addition to detection of fake or altered biometric characteristics, it includes also detection of coercion, non-conformity, and obscuration. The Liveness Detection methods can be further divided into hardware and a software-based groups [24]. The hardware-based methods try to add Liveness Detection to existing fingerprint sensor designs by addition of new hardware components, or even try to create a new sensing technology that would be difficult to deceive due to the scientific principles used in the fingerprint acquisition process. The software-based methods, on the other hand, process the image signal provided by the existing fingerprint sensors, and add Liveness Detection capability by augmenting the software architecture with a dedicated attack detection algorithm that is capable of distinguishing the patterns between genuine living fingers and fake or even cut-off fingers. Thus the software-based methods enable limited costs but at the same time they imply less universal applicability. The main challenge of a liveness detection method is to cope with widely varying properties of a living finger. Due to the large variations of properties of living fingers, it is typically possible to create a fake representation with the correct attributes, as long as the number of the properties verified is rather small. It is difficult to predict and consider all possible fake fingerprint fabrication methods and artefact materials and thus many of the fake detection approaches can be circumvented, as soon as the right novel artefact material and fabrication method have been identified.

2.5.1 Software based Liveness Detection

The software based methods of Liveness Detection try to make use of the existing hardware designs, and add the Liveness Detection capability by updating the software part of the fingerprint sensor design. Software based methods have the potential to differentiate a captured genuine living finger from the signal stemming from a fake finger when the captured sample was generated

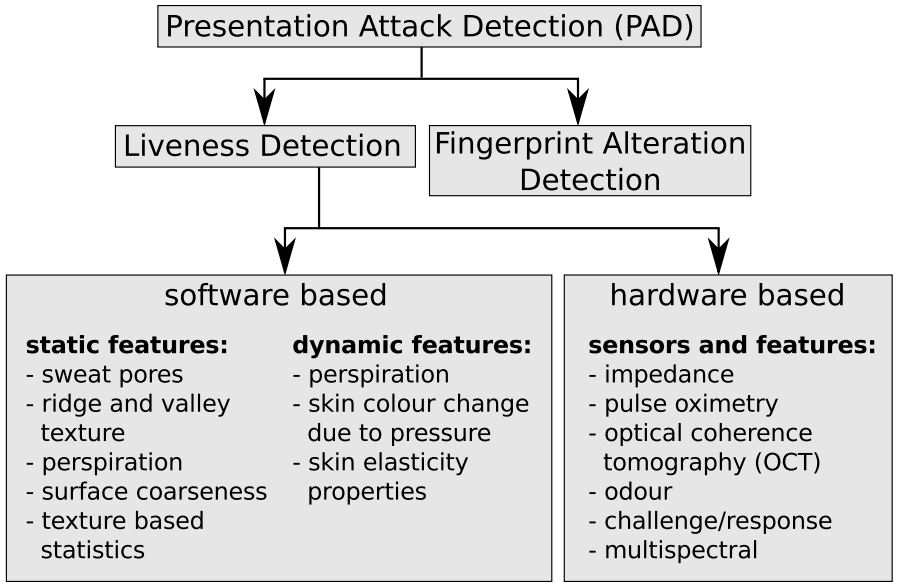

Figure 2.3: Presentation Attack Detection (PAD) methods

at high resolution. Some categorization of the methods has been proposed in the literature [24, 63]. The methods can be divided into two categories based on whether they work with a single static 2D scan, or need multiple 2D scans at different time points during the acquisition process that support the observation of dynamic properties.

2.5.1.1 Static Methods

The static software-based liveness detection methods make use of a single 2D scan available from the classical 2D sensors. The methods analyse various differences between scans of genuine and fake fingers that are caused by differences in elastic properties, inaccurate reproduction of the genuine fingers, absence of skin perspiration, etc.

sweat pores - One of the ideas applied is the detection and analysis of sweat pores. The sweat pores are very small circular structures present in the fingerprint ridges of living fingers that are endings of internal skin structures called sweat glands (Fig. 2.4).

The sweat glands are responsible for production of sweating fluid. The Liveness Detection methods based on analysis of sweat pores usually expect that such small structures would be very difficult to reproduce with sufficient quality when the fake finger is produced. Espinoza and Champod [37] claim that even though it is possible to replicate sweat pores using the fake fingerprint fabrication methods, the quantities of pores differ in fingerprints gener-

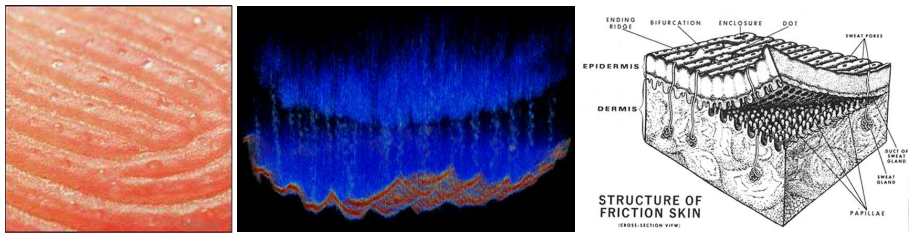

Figure 2.4: (a) sweat pores [67], (b) OCT scan of the sweat glands [101], (c) fingertip skin structure (courtesy of the FBI)

ated by real living fingers compared to fingerprints generated by fake fingers and the difference can be used as a measure of Liveness Detection. Manivanan et al. [65] suggest a method for static detection of active sweat pores in fingerprint scans that have been captured by sensors of higher resolutions than typically available ($>$ 800 dpi). They suggest integration of this method into fingerprint sensors in order to perform Liveness Detection. Choi et al. [20] suggest a method that analyses sweat pores and uses a statistic based on their distances from one another (individual pore spacing) as one of the features to distinguish between genuine and fake fingers. The method has been presented on a dataset of 500 dpi images.

ridge and valley texture - Another possibility is to analyse the highly detailed textures of the fingerprint scans and look for differences due to inaccurate reproduction of the original finger or differences in elastic properties of genuine and fake fingers. Tan and Schuckers [105] use an approach based on extraction of the signal in the valleys of the scanned fingerprint. The valleys are thinned to obtain a skeleton that determines the valley signal and the signal is then analysed in a multi-resolution fashion using wavelets in order to perform Liveness Detection. Tan and Schuckers [105] claim that the valley signal has a distinct noise distribution in fake fingerprints as compared to fingerprints obtained from genuine living fingers. Jin et al. [56] suggest that middle ridge and middle valley signals are interesting features that can be used to distinguish living and fake fingers. They skeletonise the fingerprint and its inverted version in order to obtain skeletons of the ridge and valley structures. Afterwards, they analyse the 1D signals extracted from underneath the skeletons - the middle ridge signal and the middle valley signals. They claim that due to problems with achieving high-quality replication of the sweat pores in the fake fingerprints, a middle ridge signal generated from a fake fingerprint scan is generally less periodic than a middle ridge signal generated by a genuine living finger. They also observed living fingers usually yield scans with less noisy middle valley signals than the fake fingers. In addition, their method uses the overall clarity of the ridge/valley structure examined in the spectral domain as one of the classification features. Marasco and Sansone [66] also analyse the ridge signal determined by the ridge skeleton as one of

the features for their Liveness Detection method.

perspiration - When a living finger is put on the surface of a fingerprint sensor, the sweat fluids start to spread along the ridge/valley structure and the changes are observable in matter of seconds. Even though this phenomenon of perspiration can be used in dynamic methods by observing changes in the scan over time, there are also suggestions that this phenomenon is important even in case of a single 2D scan of a fingerprint. Jin et al. [56] observed that even in a single 2D scan, the pores obtained by using a living finger look different than pores obtained by using a fake finger due to the perspiration phenomenon. The perspiration phenomenon is utilized by Tan and Schuckers in [104]. The authors obtain a skeleton of the ridge structure and afterwards extract the ridge signal determined by this skeleton. The signal is later analysed using wavelets and classified in order to distinguish between fake and living fingers. In their other work, Tan and Schuckers [106] also analyse the middle ridge signal obtained from centres of the ridges by means of the ridge structure skeleton. Due to the perspiration phenomenon, the middle ridge signal obtained from a living finger is of periodic nature determined by the periodic occurrence of the active sweat pores. Due to absence of the sweating process, middle ridge signals obtained from fake and cut-off fingers do not exhibit this significantly periodic nature. In addition to middle ridge signal analysis, the method analyses the middle valley signal that has also been observed to differ between living and fake fingerprint scans. Marasco and Sansone [67] propose an approach that combines multiple static features based both on perspiration and differences between morphology of living and fake fingers. They extract features based on multiple first-order image statistics, spacing between the sweat pores, gray-level intensity ratios and the noise residue that is acquired by subtraction of the original and denoised fingerprint scan. In addition to ridge signal analysis as discussed above, Marasco and Sansone [66] use several first-order statistics as features for the classification process. They also use multiple features based on pixel gray-level intensities. Their approach is based on the assumption that living fingers have less uniform gray-levels along ridges compared to fake fingers and also the contrast between ridges and valleys is higher in case of genuine living fingers. They also calculate ratios between brighter and darker pixels of the acquired fingerprint scan and analyse the noise residue obtained by application of wavelet based approach.

surface coarseness - Moon et al. [80] suggest an approach based on another difference between fingerprint scans obtained from living fingers in comparison to fake fingerprint scans. They claim that the large molecules of materials used to produce fake fingerprints tend to agglomerate causing the surface of the resulting fake to be somewhat coarser compared to the original living finger. They apply wavelet-based denoising procedure on the fingerprint scan, and calculate the noise residue by subtracting the original and the denoised image from each other. Properties of this noise residue are analysed for Liveness Detection purposes. A similar approach was taken by Pereira et al. [91]. The authors tried to apply the surface coarseness analysis for the classical fin-

gerprint scanner resolution of 500 dpi.

general texture analysis and feature fusion - Nikam and Agarwal have published several methods based on statistical analysis of the fingerprint scans. They have experimented with features based on combination of gray level co-occurrence matrices (GLCM) and the Wavelet Transform [86], the Ridgelet Transform [13, 87], Gabor filters [84] and the Curvelet Transform [83]. In addition, they tried to obtain features by application of local binary patterns along with the Wavelet Transform [85]. By using the above mentioned approaches, they obtained a large number of features that could be used to distinguish between live and fake fingers. They reduce the number of features by means of the Principal Component Analysis or Sequential Forward Floating Selection (SFFS) and classify the fingerprint scans into live and fake by using a hybrid classifier based on Neural networks, Support Vector Machines or the AdaBoost technique. Pereira et al. [92] have combined a number of features that have been suggested by the previous research. They use individual pore spacing, residual noise, multiple features based on first-order image statistics, features based on ratios between darker and brighter pixels and features based on strength and clarity of the ridge structure. The initial variety of features is reduced by application of the SFFS technique and the classification is performed using a MLP neural network and a support vector machine. Coli et al. [23] also analyse fingerprints in the spectral domain. They report that energies of high frequency bands are useful to distinguish between fake and genuine living fingers, because the fake fingers do not preserve high frequency details of the living fingers. Galbally et al. [40] propose a detection method based on analysis of multiple quality oriented features in fingerprint scans. They extract features based on continuity and smoothness of the ridge flow in good quality fingerprints along with features describing overall and local clarity of the ridge structure. The classification is done using Linear Discriminant Analysis method.

2.5.1.2 Dynamic methods

Another group of software-based Liveness Detection methods try to distinguish between living and fake fingers by analysing time-series of the fingerprint images acquired during the scanning phase, rather than analysing a single 2D scan only. These methods can make use of any of the above discussed static features, but they also utilize differences between the frames in the time-series.

skin distortion - Antonelli et al. [4] have proposed a dynamic Liveness Detection approach based on skin distortion. During the fingerprint acquisition, the biometric capture subject is required to slightly rotate the finger in counter-clockwise direction. Series of images are obtained during the rotation process. Optical flows are calculated in the acquired sequence and distortion maps are obtained. They compare distortion codes acquired in the enrollment phase with distortion codes obtained in the identification phase in order to

Figure 2.5: Time-series of fingerprint scans [55]

identify whether a finger of the enrolled individual was used. Jia et al. [55] use an approach that does not require any special behaviour from the capture subject. A series of images is acquired when the subject puts his finger onto the sensor as illustrated by Fig. 2.5. The authors extract features based on area of the fingerprint that is in contact with the sensor. The features describe how the scan of the contact area changes in size and brightness when the finger is being put on the sensor. They use a classifier based on Fisher Linear Discriminant analysis. Zhang et al. [115] have published a dynamic software Liveness Detection method based on fingerprint deformation analysis by using the thin-plate spline (TPS) model. The method requires the capture subject to put the finger on the sensor surface, and then apply some pressure in four different directions. The method uses a minutia based algorithm to detect corresponding minutiae between the distorted fingerprint images and the undistorted fingerprint. Distortions of the minutia positions are used to calculate TPS models of the distortions and bending energy vectors are extracted. The bending energy vectors are compared to pre-trained fuzzy sets of bending energies in order to distinguish genuine living fingers from fake ones.

perspiration - A relatively widely researched approach to dynamic software-based Liveness Detection is the analysis of the perspiration phenomenon that was already mentioned above for the static approaches. When a living finger is put on the surface of a fingerprint sensor, the fingerprint scan slightly changes in time due to moisture produced by the sweat glands. This moisture pattern is analysed across scans obtained in multiple time-points in order to verify that a genuine living finger is put on the sensor. This phenomenon is a possible means of separation, because fake and even cut-off fingers do not produce similar patterns when scanned by the sensor. One of the early research works on the perspiration phenomenon for Liveness Detection was done by Derakhshani et al. [30] with emphasis on the capacitive fingerprint sensors. They capture two fingerprint images at time-points $0s$ and $5s$ and compare the middle ridge signals extracted from them. They observed that the middle ridge signal of the first scan is of much more wavy nature due to spreading of the moisture. They extract features based on these differences along with a feature that describes the amount of energy of the expected frequency of pore occurrence. Finally, they use a classifier based on back-propagation neu-

ral network in order to distinguish between genuine living fingers and cut-off and fake ones. The method is further improved by Parthasaradhi et al. [90] by addition of features that deal with the situation when a fingerprint signal gets out of the dynamic range of the sensor due to extreme dryness/moisture. They tested the method with electro-optical and optical sensing technologies in addition to capacitive sensing technology only. They have carried out further experiments with classifiers based on neural networks, discriminant analysis and OneR method.

Figure 2.6: Fingerprint images acquired (a) immediately (b) after 2 seconds [2]

Abhyankar and Schuckers [2] have also utilized wavelet analysis for perspiration based Liveness Detection. They capture two consecutive images at $0s$ and $2s$ and analyse the differences between them (Fig. 2.6). They decompose the low-frequency content of the image using the multiresolution analysis (MRA) and the high-frequency content using the wavelet packet analysis. From all the resulting sub-bands, they filter out the low-energy coefficients to keep only the most significant information. Afterwards, they compute the difference between the transformation of the first fingerprint image and the transformation of the last fingerprint image in order to get a representation of the changes due to the perspiration phenomenon. From this representation of the difference between the two images, only significant coefficients representing larger changes are kept. The classification is done based on the total energy of the remaining coefficients. Jia and Cai [54] have combined features based on skin elasticity with features determined by the perspiration phenomenon. The method operates with a series of multiple fingerprint images taken in a time period of few seconds. They extract one feature analysing the energies of the spatial frequencies of the pore occurrences in the middle ridge signal in a way similar to [30]. The second static feature is based on gray-level distributions. The first two dynamic features are based on change of the fingerprint area in contact with the sensor surface during the time-sequence, and the third dynamic feature is based on the comparison of "bumpiness" between middle ridge signal of two consecutive fingerprint scans as in [30]. Decann et al. [29] have published a fingerprint Liveness Detection algorithm that utilizes an adaptation of the standard computer vision region labeling technique. In the first step, they obtain skeletons of the fingerprint ridge structure and the fingerprint valley structure. Afterwards, the difference image

between the scans that have been acquired at subsequent points in time, is computed. Using the mask, the region labeling algorithm is run starting from the points along the fingerprint skeletons. The result of this step is a set of small regions along the ridges and valleys in the difference image as based on image intensities. The region labeling approach can be applied also to a single binarised fingerprint image rather than a difference image. The extracted features used for classification are based on numbers of such small regions, their size distribution, etc. Nikam and Agarwal [88] have published a method of distinguishing between live and fake fingers as based on wavelet analysis of the middle ridge signal. They compute the middle ridge signals of the two consecutive fingerprint images as determined by skeleton of the ridge structure, and then apply the wavelet analysis on the two obtained signals. Various classification features are extracted as based on differences between the coefficients in the obtained sub-bands. Marcialis et al. [70] have proposed a method based on detection of sweat pores in two consecutive fingerprint scans captured at $0s$ and $5s$. They extract a skeleton of the ridge structure and along this skeleton they search for sweat pores by using the template comparison method. The pore extraction is done both for the first and the second fingerprint scan. The classification features are based on differences of pore quantities between the two scans and on distances of the pores from each other. Standard fingerprint quality measures are also added to the classification feature set. Memon et al. [77] suggest a method for detection of active sweat pores in high-resolution fingerprint sensors ($>$ 800 dpi). They filter the fingerprint image using a high-pass filter to obtain high frequency information associated with the small patterns expressed by the active sweat pores. The resulting image is then correlated with a correlation filter that represents a usual response of an active sweat pore. The obtained local maxima that are higher than a given threshold are considered to represent the active sweat pores. Abhyankar and Schuckers [3] have proposed a Liveness detection method based on analysis of signal changes between the so called singular points that can be detected in a fingerprint scan. The singular points are points in a fingerprint scan that have specific properties in the spatial domain and in different scales when analysed by wavelet analysis. The singular points are detected in two consecutive fingerprint scans taken at $0s$ and $2s$. Afterwards, the singular points are linked across the two images. The linking is mapped into time domain using B-spline interpolation and further analysed using the Empirical Mode Decomposition (EMD) method. The classification is based on energies of the decomposed signals.

2.5.2 Hardware based Liveness Detection

Various ideas have been behind introduction of an improved fingerprint sensing technology or an update to existing hardware designs in order to make the sensors difficult to deceive.

challenge/response - Yau et al. [113] have proposed a challenge/response

based Liveness detection method for fingerprint sensing technologies. The sensor is equipped with an electrode array that is capable of generating electric pulses that are transferred into the fingertip of the biometric capture subject. Depending on what electrodes are activated, the array can make the subject feel an impression of a tactile pattern underneath his finger. In order to successfully accept the finger, the capture subject must verify the pattern by choice of an offered visual pattern on a screen. The idea is that using fake fingers, the electro-tactile pattern will not be perceivable making the authentication impossible.

odour - Baldisserra et al. [7] have suggested usage of an electronic noise to distinguish between live and fake fingers. Living fingers are expected to express different odour than fake fingers, rendering the odour analysis a suitable means of separation. The authors have experimented with electronic noses in order to distinguish between genuine fingers and fake fingers made of latex, gelatin and silicone.

pulse oximetry - Another idea about how to perform Liveness Detection using special hardware is to use the pulse oximetry approach. For the living fingers, blood circulates through the tissues. The oxygenated hemoglobin in the blood carries oxygen to the cells, and becomes deoxygenated afterwards. New oxygenated hemoglobin is periodically brought to the tissues with every heartbeat. The research has shown that oxygenated hemoglobin strongly absorbs light of wavelengths around 940nm, while the deoxygenated hemoglobin has strongest light absorption around 660nm [94]. Pulse oximetry is based on an analysis of the periodic changes in absorption of light of the two wavelengths, that take place in the tissue due to blood circulation as illustrated by Fig. 2.7. The principle of absorption of the two wavelengths by hemoglobin is also utilized in biometric vein imaging.

Reddy et al. [94] have proposed a pulse oximetry based method of fingerprint Liveness Detection. In their design, the finger is illuminated by two LEDs of wavelengths of 660nm and 940nm. The light is captured by a single sensor. In order to distinguish between the responses as determined by the two light sources, the activity of the LEDs is modulated in time. Periodical changes in the absorption of light from the two sources are analysed in order to identify whether a genuine living finger is being scanned. Hengfoss et al. [48] have analysed absorption of light of various wavelengths in living and fake/cadaver fingers using a spectrometer. They have also analysed periodic changes of light absorption in time, due to blood circulation. The have observed that fake/cadaver fingers do not express this periodic pattern.

multispectral properties - Analysis of fingertips under multi-spectral circumstances is another way of dealing with the problem of fingerprint Liveness Detection. The genuine living finger is made of tissues that generally do not have the same properties as fake/cut-off fingers when illuminated by various wavelengths of light. Analysis of fingerprint scans obtained by using multiple wavelengths of light is a possible classification approach. The multi-spectral design described by Rowe et al. [95] is utilized in the LUMIDIGM technol-

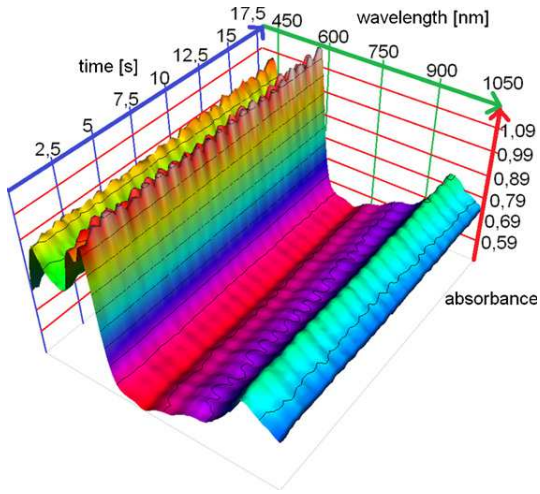

Figure 2.7: Changes of light absorption due to blood circulation [48]

ogy [62]. The sensor acquires multiple images of the fingertip under various illumination conditions, as regards the wavelength, orientation, and polarization of the light emitted. The captured images depict the fingertip at various depths and with variations depending on the different absorption of the individual wavelengths in the fingertip [95]. The Liveness Detection is performed by analysis of these scans. Another possibility is to illuminate the finger by multi-spectral light source, and analyse the whole transmission/reflectance signature in the range of the spectrum. Hengfoss et al. [48] have published an extensive analysis of multi-spectral signatures of living vs. fake/cadaver fingers. They emphasize another interesting phenomenon that is a possible means of classification. When a living finger is put on the surface of the sensor and some pressure is applied, the blood is pressed away from the tissues. This process is observable on the change of the multi-spectral signature in time. The authors report that this phenomenon appears only for genuine living fingers and not for fake or cadaver ones. The multi-spectral signature also changes in time due to blood circulation in the tissues. These two dynamic features are possible means of separation along with static features extracted from a single multi-spectral signature. Chang et al. [15] acquire multiple fingerprint images using light of wavelengths in $400 - 850nm$. Edge detection is performed on each of these images. Energies of the fingerprint scans obtained using various wavelengths and the edges detected in the images are used as features for classification.

heartbeat movements - Some research has been done on detection of fine movements of the living fingers due to heartbeat. These approaches utilize the fact that the heartbeat causes periodic slight volumetric changes of the tissues [34]. Drahansky et al. [34] suggest usage of a high-resolution camera

to detect distances between specific points on the fingerprint as they change in time, and use the resulting signal as a Liveness Detection measure. As another possibility of making use of the same principle of periodic volumetric changes, they propose distance measurements by using a laser.

electrical properties - Another idea is to use the difference in electrical properties of the living skin compared to the fake materials. Martinsen et al. [72] have used an electrode array to measure impedance of the fingerprint tissue. The system performs Liveness Detection by means of multiple measurements using different electrodes on the array. Additionally, the frequency properties of the signal to which the tissue is exposed vary during the measurement process. The authors claim that electrodes that are farther apart from each other on the array cause the internal tissues to have larger influence on the resulting impedance. In this way, by comparison of results from different electrodes with different distances from each other, they can indicate the presence of a living fingertip with multi-layer structure of the living skin. Shimamura et al. [98] suggest a way how to integrate a fake fingerprint detection module into a capacitive fingerprint sensor. Their fraud detection method is based on impedance measurements.

OCT - Some research has been done on the application of the Optical Coherence Tomography (OCT) for the fingerprint sensing scenario. The OCT is a medical imaging method widely used for retina scanning. The technology utilizes interference of beams of light of low coherence length in order to measure reflectance of the scanned material at different positions and depths. In this way, a volumetric scan of the material can be acquired. Due to general scattering of the light as it travels deeper into the tissue, this method can penetrate the surface to the maximum depth of around $3mm$. Cheng and Larin [19] have applied the OCT for fingerprint Liveness Detection by using the autocorrelation analysis. They obtained 2D scans of a part of the fingertip in a lateral ($2.4mm$) and the depth ($2.2mm$) directions. Afterwards, they computed autocorrelation function in the depth direction. They have demonstrated that the obtained autocorrelation function is very different for the case of living and fake fingers. Cheng and Larin [18] were also among the first to obtain 3D density representations of real and fake fingerprints obtained by the OCT technology, and to experiment with these scans. In their work, they also publish a 3D OCT scan of a fake fingerprint surface on a real living finger. The dimensions of the scanned volume is $1.6 \times 2.4 \times 10mm$. Peterson and Larin [93] have experimented with various neural network based approaches in order to perform classification of the fingertip OCT scans into living and fake samples. They use features based on various first-order image statistics and Gabor filter responses. Dimensionality of the vector of Gabor filter responses is reduced using the self-organizing maps (SOM) approach. Application for of the OCT technology for the fingerprint Liveness Detection scenario is summarized in [15]. Cimalla et al. [22] have developed a high-resolution Fourier Domain OCT (FD-OCT) setup capable of capturing a volumetric representation from small area of the fingerprint. They have clearly visualized the helix structure

of the sweat-glands, observable with their high-resolution OCT. Bossen et al. [11] have demonstrated that the inner and outer fingerprint extracted from an OCT scan can be used for classification using the standard fingerprint comparison methods. Liu and Buma [61] have experimented with a FD-OCT setup capable of capturing a 3D OCT volume from a partial fingerprint area, and suggested the positions of sweat glands as a possible biometric characteristic. Nasiri-Avanaki et al. [82] have published a work that demonstrates usability of OCT scanning for distinguishing between genuine living fingers and the fake ones. In the framework of the OCT-I project organized by German Federal Office for Information Security, Meissner et al. [74] have used an FD-OCT setup to collect a large scale dataset of genuine and fake volumetric fingerprint OCT scans from a small area of 4x4mm and carried out a manual classification study to assess the PAD potential of the OCT for various fake materials & production techniques. On the collected dataset, Menrath [79] experimented with automatic methods for detection of sweat glands, as well as an approach for extraction of the outer and inner fingerprint from an OCT scan. Khutlang et al. [58] have used a commercially available FD-OCT scanner to capture a partial fingerprint area and experimented with internal fingerprint detection and subsequent feature extraction. Promising recent studies by Darlow et al. [26, 27, 28] focus on the fast extraction of the 2D inner and outer fingerprints from 3D volumetric fingerprint scans. Their studies are carried out using a commercially available FD-OCT setup capable of scanning in a 15x15mm fingerprint area. In the framework of the INGRESS project [1], Auksorius & Boccara [5, 6] have developed a fingerprint sensor prototype based on Full-Field OCT (FF-OCT). Their approach requires the fingerprint to be pressed against a glass surface.

2.6 Liveness Detection performance

A benchmark of the previously mentioned methods is difficult. While metrics needed for such a benchmark are now introduced by the international standardization project ISO/IEC 30107 [50], there is not yet a ground truth database. Most of the authors have produced their own databases of fake and living fingers as a part of their research work. The databases vary in size of the sets, in the methods used to create fake fingers, and in usage of cadaver fingers. Some authors evaluate their methods using fake fingers created by using the ”direct casting” methods, some add also fakes produced by means of the ”indirect casting” methods. Usage of materials for fabrication of the fake fingerprints and mould materials also vary between authors and publications. Since the quality of a fake fingerprint strongly influences performance of a Liveness Detection method, it is challenging to conduct a fair assessment based on results obtained on such widely varying data. The sensor that has been used for data acquisition is another variable in the evaluation datasets. Only some of the software-based methods have been tested with multiple sen-

sor technologies. Different detection rates on different sensing technologies suggest that the sensor technology that has been used for data acquisition is of significant importance. It is difficult to say whether the features would perform well on another sensing technology.

In addition, the static and dynamic software approaches require different inputs - the static approaches make use of a single fingerprint scan, while the dynamic approaches need a time-series of images. Various static software-based methods have different requirements on the image resolution, and can relate to a specific sensor technology that produces patterns detected by the method. The dynamic approaches have to deal with different resolution requirements, and also with varying requirements on the time-sequence analysed. While some methods make use of two consecutive images (obtained at various intervals), other methods use a series of multiple images obtained at a given frame-rate.

These varying requirements on the input fingerprint data analysed make developing of a standard evaluation database rather difficult, even for the software-based approaches. The development of a database that would be applicable to testing of hardware-based approaches would be even more difficult.

Nevertheless, there have been attempts to create such standardized dataset for evaluation of the software-based Liveness Detection approaches. In 2009, Marcialis et al. [69] organized the first international fingerprint Liveness Detection competition, LivDet 2009. The competition makes it possible for researchers and companies to submit their algorithms for evaluation on a large-scale standardized dataset of fingerprints obtained both from living and fake fingers. The dataset consists of large number of scans from three different optical fingerprint scanners. A subset of 25% of the data was made available as a training set before final submission and evaluation using the remaining 75% of the data. Detailed information about datasets used in LivDet 2009 is listed in Tab. 2.2. The single-scan nature of the dataset used in LivDet 2009 makes the competition relevant only for static software-based Liveness Detection approaches.

Table 2.2: Datasets used in LivDet 2009 [69]

Datatset	Scanner model	Res. (dpi)	Image size	Live Samples	Fake Samples
1	Crossmatch Verifier 300 LC	500	480x640	2000	2000
2	Identix DFR2100	686	720x720	1500	1500
3	Biometrika FX2000	569	312x372	2000	2000

Four different algorithm solutions were evaluated by LivDet 2009. The best performing algorithm was submitted by Dermalog Identification Systems GmbH. The second was an academic solution from Galbally et al. [40]; and the two last algorithms were from two anonymous sources. In this chapter, the results are presented in terms of ISO/IEC 30107 metrics, namely False Non-Live Detection Rate (FNLDR) and False Live Detection Rate (FLDR). The FNLDR metric represents the proportion of live presentation characteristics incorrectly classified as being non-live, while the FLDR metric represents the proportion of non-live presentation characteristics incorrectly classified as being live. The paper published by LivDet 2009 [69] mentioned unusually high FNLDR of the evaluated algorithms on the set of genuine living fingers from the Biometrika sensor (Tab. 2.3). The lower number of distinct live subjects in the training set for the Biometrika dataset, was mentioned as a possible explanation (Tab. 2.4). Tab. 2.3 also demonstrates the large impact of the sensor on the classification accuracy. Even though all of the sensors were optical, large differences in Liveness Detection performance of the same methods were recorded.

Table 2.3: Classification results of algorithms submitted to LivDet 2009 [69] reported with *FNLDR* and *FLDR*

Submitted algorithms	Identix		Crossmatch	
	FNLDR	FLDR	FNLDR	FLDR
Dermalog	2.7%	2.8%	7.4%	11.4%
ATVS	9.8%	3.1%	8.8%	20.8%
Anonymous	15.2%	11.5%	27.1%	18.9%
Anonymous2	9.8%	11.3%	14.4%	15.9%
	Biometrika		Average	
	FNLDR	FLDR	FNLDR	FLDR
Dermalog	74.1%	1.9%	20.1%	5.4%
ATVS	71.7%	3.1%	30.1%	9.0%
Anonymous	56.0%	17.6%	32.8%	16.0%
Anonymous2	15.6%	20.7%	13.2%	16.0%

Another run of the Liveness Detection competition was organized by Yambay et al. [112] in 2011. This time, the competition consisted of two parts - algorithms and systems. Similarly to LivDet 2009, the algorithm part allowed academics and companies to submit their static Liveness Detection solution for fingerprints. The new system part of the competition provided a framework for evaluation of hardware-based solutions. Competitors could submit their hardware solution to the competition, and the performance of the system was evaluated using a unified protocol that allowed for a fair benchmark of the systems' performance.

The software-based part of the competition was evaluated using a large-scale dataset obtained by using four different fingerprint sensing devices -

Table 2.4: Number of unique subjects in LivDet 2009 (Indentix and Crossmatch samples acquired in multiple sessions, Biometrika samples acquired in a single session) [69]

Scanners	# of Training Subjects	# of Testing Subjects	Aver Images / subject
Identix	35	125	18.75
Crossmatch	63	191	15.75
Biometrika	13	37	40.0

Biometrika, Digital Persona, Italdata and Morpho (formerly Sagem). More detailed description of the dataset is given in Tab. 2.5.

4000 fingerprint images per fingerprint device were acquired (2000 spoof samples and 2000 live samples). The fake fingerprints used for collecting of the dataset were made of gelatin, latex, PlayDoh, silicone, and wood glue for the Digital Persona sensor and the Morpho sensor. The fake fingerprints used with Biometrika and ItalData sensors were made of gelatine, latex, ecoflex (platinum-catalysed silicone), silicone, and wood glue. Details about numbers of samples obtained using genuine living fingers per sensing device are given in Tab. 2.6.

Table 2.5: Datasets used in LivDet 2011 [112]

Dataset	Sensor	Sensor Model	Resolution (dpi)	Image Size
#1	Biometrika	FX2000	500	315×372
#2	Digital Persona	4000B	500	355×391
#3	ItalData	ET10	500	640×480
#4	Morpho	MSO300	500	352×384

Table 2.6: Datasets used in LivDet 2011 [112]

Dataset	Sensor	Live Training Samples	Live Testing Samples	Number of Fingers
#1	Biometrika	1000	1000	200
#2	Digital Persona	1000	1000	200
#3	ItalData	1000	1000	200
#4	Morpho	1000	1000	112

Three software-based Liveness Detection solutions were submitted to the algorithm part of the LivDet 2011 competition. The solutions were provided

by the Chinese Academy of Sciences, Institute of Automation (CASIA); Federico II University (Federico); and Dermalog Identification Systems GmbH (Dermalog). Detailed information about performance of these algorithms on the large-scale datasets collected for the LivDet 2011 is listed in Tab. 2.7. The results again demonstrate strong variation in classification accuracy depending on the sensor that was used for data acquisition. The benchmarks from LivDet 2009 and 2011 do not demonstrate improvement of the Liveness Detection capabilities. The results suggest that the quality of the fake finger and its fabrication technique has a very significant influence on the performance of the methods, rendering the methods vulnerable to novel fake fabrication techniques and approaches.

Table 2.7: Classification results of algorithms submitted to LivDet 2011 [112] reported with *FNLDR* and *FLDR*

	FNLDR			FLDR		
	Dermalog	Federico	CASIA	Dermalog	Federico	CASIA
Biometrika	11%	38%	29.7%	29%	42%	38.1%
ItalData	15.10%	39.90%	50.6%	28.50%	40.10%	2.8%
Morpho	15.10%	13.80%	22.1%	12.50%	13.10%	23.6%
Digital Persona	66%	6.20%	16.1%	6.20%	11.60%	34.7%
Average	35.30%	26.60%	29.625%	17.60%	24.50%	24.8%

Performance evaluation of Liveness Detection capabilities of the fingerprint recognition systems submitted to LivDet 2011 is shown by Tab. 2.8. The FLDR Known represents False Live Detection Rate for fake fingerprints produced by using recipes published in the competition description. The FLDR Unknown represents False Live Detection Rate for fake fingerprints produced by using recipes that were not published in the competition description. The error rates in Tab. 2.8 suggest that the performance of the methods is strongly affected by the particular fake fingers used for the spoofing attempt. The fake finger fabrication techniques that were unknown prior to the development of the methods or variations of the known techniques could pose a significant security risk.

Table 2.8: Classification results of systems submitted to LivDet 2011 [112] reported with *FNLDR* and *FLDR*

Submitted Systems	FLDR	FNLDR	FLDR Known	FLDR Unknown
Dermalog	0.8%	42.5%	0.4%	1.3%
Greenbit	39.5%	38.8%	19.1%	70%

Ghiani et al. [43] have used the large-scale database produced in scope of the LivDet 2011 competition to evaluate performance of several existing Liveness Detection algorithms on a single dataset. They have benchmarked performance of the methods based on local local binary patterns, detection of pores [70], power spectrum [23], wavelet energy signature [85], wavelet analysis of the ridge signal [104], valley noise analysis [105], curvelet energies [83], and GLCMs [83]. The benchmark results for the analysed methods are shown by Tab. 2.9 and Tab. 2.10.

Table 2.9: FLDR of the methods as evaluated by Ghiani et al. [43]

	Biometrika	Italdata	Digital Persona	Morpho
LBP	16.40%	15.10%	8.70%	4.34%
Pores Detection [70]	27.80%	22.00%	30.50%	49.90%
Power Spectrum [23]	23.90%	29.40%	23.50%	21.81%
Wavelet Energy [85]	73.00%	51.80%	15.10%	16.22%
Ridges Wavelet [104]	47.10%	63.10%	37.00%	18.15%
Valleys Wavelet [105]	48.60%	39.10%	12.40%	55.12%
Curvelet Energy [83]	55.10%	40.70%	27.40%	39.58%
Curvelet GLCM [83]	16.40%	25.20%	22.00%	25.00%

Table 2.10: FNLDR of the methods as evaluated by Ghiani et al. [43]

	Biometrika	Italdata	Digital Persona	Morpho
LBP	5.90%	22.00%	12.60%	12.70%
Pores Detection [70]	26.90%	35.30%	41.70%	30.40%
Power Spectrum [23]	37.40%	56.20%	30.80%	41.20%
Wavelet Energy [85]	27.40%	41.80%	13.00%	27.90%
Ridges Wavelet [104]	30.50%	50.80%	18.10%	22.90%
Valleys Wavelet [105]	9.40%	8.20%	13.70%	9.00%
Curvelet Energy [83]	35.30%	55.10%	16.40%	17.50%
Curvelet GLCM [83]	29.40%	36.30%	14.70%	31.10%

Marcialis et al. [68] have done additional testing of the above mentioned Liveness Detection approaches with various regions of interest (ROI) and under various data acquisition conditions. Coli et al. [25] have experimented with various Liveness Detection features and evaluated their classification performance.

For the cases when the self-declared performance scores could be interpreted in terms of the ISO/IEC 30107 FNLDR and FLDR metrics, the self-declared scores of the above discussed methods are included in Tab. 2.11.

Table 2.11: Scores obtained from the results as declared by the authors reported as *FNLDR* and *FLDR*

Method		FNLDR	FLDR
Nikam and Agarwal [83]		1.62%	2.08%
Nikam and Agarwal [86]		2.16%	2.5%
Nikam and Agarwal [84]		2.16%	2.5%
Espinoza and Champod [37]		8.3%	21.2%
Galbally et al. [40]	Biometrika	1.54%	2.12%
	CrossMatch	11.94%	10.3%
	Identix	7.07%	6.4%
Pereira et al. [92]	DB 1	7.35%	2.42%
	DB 2	13.68%	4.52%
Marasco and Sansone [66]	Biometrika	12.2%	13.0%
	CrossMatch	17.4%	12.9%
	Identix	8.3%	11.0%
Nikam and Agarwal [87]		1.62%	3.33%
Nikam and Agarwal [85]		1.62%	3.33%
Tan and Schuckers [105]	Precise	0%	1.6%
	Secugen	0%	9%
	Ethentica	0%	7.4%
	Biometrika	9.1%	0%
Marasco and Sansone [67]	Biometrika	12.2%	13.0%
	CrossMatch	17.4%	12.9%
	Identix	8.3%	11.0%
Decann et al. [29]		1.2%	1.2%
Tan and Schuckers [106]		0.9%	0.9%
Nikam and Agarwal [88]		2.08%	0.9%
Jia and Cai [54]		4.49%	4.49%
Antonelli et al. [4]		11.24%	11.24%
Zhang et al. [115]		4.5%	4.5%
Jia et al. [55]		4.78%	4.78%

A relatively large performance gap can be observed if the performance scores reported by the authors are compared to the results that were reported by independent evaluations as carried out by Ghiani et al. [43], LivDet 2009 [69], and LivDet 2011 [112]. The results of LivDet 2013 [44] confirm that the Liveness Detection methods are vulnerable against high-quality fake fingerprints that were created using the "direct casting" fake fabrication methods.

An overview of the results of the most most recent study in terms LivDet 2015 [81] competition is listed in Tab. 2.13. The study involved 4 different optical fingerprint sensors - Green Bit, Biometrika, Digital Persona and Crossmatch - Tab. 2.12. For the Green Bit, Biometrika and Digital Persona sen-

sors, the fingerprint artifacts were made of Ecoflex, gelatine, latex, woodglue, liquid Ecoflex and RTV (a two-component silicone rubber). For the Crossmatch sensor, the artifacts were composed of Playdoh, Body Double, Ecoflex, OOMOO (a silicone rubber) and a form of Gelatin [81]. Prior to the competition evaluation phase, the authors of the competing algorithms were provided with a training set that allowed them to adapt and train their PAD solutions. The testing set, used during the evaluation phase, contained scans of artifacts made of two 'unknown' materials - artifact materials not included in the training set [81]. For the Green Bit, Biometrika and Digital Persona sensors, the 'unknown' materials were liquid Ecoflex and RTV. For the Crossmatch sensor, the 'unknown' materials were OOMOO and Gelatin [81].

Table 2.12: Properties of the sensors used in LivDet 2015 [81]

Scanner	Model	Resolution [dpi]	Image Size [px]	Format Format
Green Bit	DactyScan26	500	500x500	PNG
Biometrika	HiScan-PRO	1000	1000x1000	BMP
Digital Persona	U.are.U 5160	500	252x324	PNG
Crossmatch	L Scan Guardian	500	640x480	BMP

Both the authors and the independent evaluators report on the Liveness Detection performance concerning all the fake fabrication techniques, materials and individual fake fingerprints. The authors do not specify whether some individual fake fingerprints produced by specific techniques are generally more successful than others. Since the attacker typically needs only a single fake fingerprint to be able to deceive a specific Liveness Detection method successfully, such information is of crucial importance. Performance of the methods has been evaluated in terms of resistance against well-known, low-cost fake fingerprint fabrication techniques, rather than against a targeted effort to spoof a specific fingerprint recognition system.

The performance of the state-of-the-art software fingerprint Liveness Detection methods suggests that additional hardware is necessary to develop a fingerprint Liveness Detection solution that would be resistant against targeted attacks. Due to large variety of possible artefact material and fabrication techniques, a single aspect dedicated liveness detection sensor can usually be deceived if an appropriate new combination of materials and techniques has been used [97]. In order to increase the difficulty of producing an artefact, some manufacturers try to include a larger number of supplementary sensors that would capture information on multiple aspects of the scanned characteristic. Even though this greatly increases difficulty of the artefact fabrication process, the large variety of properties of genuine fingers, as well as their artefact counterparts, requires application of machine learning approaches to process information from all of the sensors and take the final decision whether a genuine characteristic has been presented. Since performance of machine

Table 2.13: Scores of different algorithm submitted to LivDet 2015 [81], reported as FNLDR and FLDR

sensor	Green Bit			Biometrika		
algorithm	FNLDR %	FLDR known %	FLDR unknown %	FNLDR %	FLDR known %	FLDR unknown %
COPILHA	36.7	19.2	24.4	22.5	17.0	42.8
CSI	16.6	16.1	24.0	15.0	17.4	19.2
CSI_MM	10.9	13.8	17.8	11.0	13.7	11.4
hbirkholz	3.6	8.8	18.4	8.0	5.4	6.2
hectorn	11.2	7.4	12.8	13.1	8.0	16.8
anonym	9.1	3.5	13.6	6.9	3.5	14.6
jinglian	7.5	2.5	7.8	3.8	7.6	6.8
UFPE I	18.9	6.2	37.0	41.8	26.7	41.4
UFPE II	20.8	1.8	16.4	37.3	20.6	28.0
nogueira	3.5	4.3	7.4	8.5	2.7	5.8
titanzhang	8.6	5.8	12.4	10.2	6.4	5.0
unina	6.5	2.0	4.0	10.9	0.4	1.4
sensor	Digital Persona			Crossmatch		
algorithm	FNLDR %	FLDR known %	FLDR unknown %	FNLDR %	FLDR known %	FLDR unknown %
COPILHA	17.7	17.1	30.6	60.0	0.5	1.7
CSI	28.2	19.2	24.2	3.1	13.6	30.3
CSI_MM	25.9	21.8	26.8	2.5	9.4	29.8
hbirkholz	12.6	10.0	14.8	6.3	10.7	18.6
hectorn	9.3	15.6	29.2	6.9	16.6	23.5
anonym	7.7	8.8	29.2	2.6	4.5	4.0
jinglian	10.7	9.2	19.4	1.9	8.1	11.6
UFPE I	32.8	14.0	14.6	29.2	53.8	47.6
UFPE II	21.8	25.8	27.6	22.6	56.8	54.1
nogueira	8.1	4.6	6.0	0.9	2.1	4.0
titanzhang	9.6	10.0	15.6	3.6	9.2	19.3
unina	35.7	0.4	0.6	1.1	2.2	13.9

learning based classifiers depends on the training data, the sensor can still be vulnerable if an entirely new material and fabrication technique has been used to produce the artefact characteristic.

A 3D scanning technology, such as OCT, can provide for a large amount of high-resolution data that would capture both outer and inner structure of the scanned finger. A reliable method that could verify the genuine structure of the fingertip scan could render the fake fabrication process extremely difficult or even practically impossible. Initial research on the potential of the OCT

technology suggests that an OCT scan contains highly detailed representation of the structure of the scanned fingertip that is sufficient to clearly distinguish genuine and fake fingers [75].

2.7 Conclusion

Even though the authors often claim very high performance scores allowing for possibilities of direct practical application of their specific Liveness Detection method, the results of testing on large-scale datasets in scope of the LivDet 2009 [69], 2011 [112], 2013 [44] and 2015 [81] suggest that fingerprint Liveness Detection cannot be considered a solved problem yet. The results suggest that the performance of the methods strongly depends on the knowledge of the fake fabrication techniques and materials during development of the method. So far, the methods have been tested rather in terms of resistance against low-cost, well-known faking techniques than in terms of resistance against targeted spoofing attacks.

The security of a system is given by the amount of effort needed to circumvent it. So far, most authors have reported liveness detection performance of their methods as universal rates for all the fakes, their method has been tested with. However, the detection performance can vary greatly as it depends on the specific fake type, and the mere quantities do not yield accurate information on the case.

The LivDet 2009 [69], 2011 [112], 2013 [44] and 2015 [81] provide for publicly available, large-scale standard datasets, which are nevertheless applicable only for static software-based Liveness Detection methods. Apart from that, the methods tested on these datasets must be capable of working with the scan resolutions of the samples as those yielded by the sensors of the LivDet projects.

What more, the methods tested on this dataset must be able to work with the scan resolutions of the samples yielded by the sensors used in the LivDet projects. Further initiative is necessary to create datasets of high-resolution images obtained in time-series, to provide for a standardized dataset for testing of the dynamic software-based Liveness Detection methods. The results are very sensitive to the quality and fabrication method of the fake fingerprints used to spoof the sensor. Therefore, the standard dataset should contain a large number of scans captured by using high-quality fake fingerprints.

The development of a database for hardware-based Liveness Detection methods is difficult due to very large variations in the sensing methods. Possibly, a fake fingerprint toolbox could be developed and shared by the research community in order to be able to perform a more reliable benchmarking of the hardware-based methods.

The performance of the liveness detection methods might be improved if some liveness related information were stored in the biometric template itself. In this way, the variations of the finger properties would be reduced and it

might also be more difficult to acquire the additional information for the fake fabrication.

The metrics used by the Presentation Attack Detection (PAD) research community are rather arbitrary and in need of standardization. Attempts have been made to introduce standards to the field of the Presentation Attack Detection (PAD) in scope of the international standardization project, ISO/IEC 30107. The development of a standardized framework for the evaluation of the Liveness Detection capabilities of biometric systems constitutes a part of the projects, BEAT - Biometrics Evaluation and Testing [10], and TABULA RASA - Trusted Biometrics under Spoofing Attacks [107].

In conclusion, in spite of the significant research effort so far, the state-of-the-art methods cannot be considered reliable in the environments that require high security levels. A 3D scanning technology, such as the OCT, can provide for highly detailed representations of the structure of a scanned fingertip and thus significantly increase the amount of information available for liveness detection purposes. A reliable method, which were able to verify the genuine structure of the scan, would render the fake fabrication process extremely difficult. The development of such method has the potential to provide for a very secure fingerprint recognition solution.

Chapter 3

Partial OCT Fingerprint Analysis

3.1 Summary

The current chapter, based on the papers by Sousedik et al. [101] and Sousedik & Busch [103], describes the analysis of OCT scans taken from a partial fingerprint area. Techniques for efficient detection of the fingerprint's layered structure in the simpler scenario, when only a partial fingerprint is considered, are proposed and evaluated. Essentials of the extraction of a partial-area fingerprint into a 2D representation are introduced. In addition, a technique for detection of low quality fingerprint OCT scans, occurring due to involuntary muscle shaking of the capture subjects, is proposed.

3.2 Optical Coherence Tomography for Fingerprints

The Optical Coherence Tomography (OCT) is a 3D scanning technology that has originally been developed for medical purposes. It is capable of capturing volumetric representations of the scanned object up to depth of 2-3mm under the surface and the captured signal is a function of the scattering properties of the material. In the classical Time-Domain OCT (TD-OCT) design, a beam of light of low coherence length and wavelength of about 830nm is split into two separate beams. The first beam is targeted at the object and reflects back. The second beam is targeted by means of a reference arm in such manner that it interferes with the beam reflected from the object. Due to low coherence length of the light source, the interference takes place only with the light reflected from a certain depth under the object surface and the amount of the light reflected can be measured [16].

The classical TD-OCT design requires the reference arm to be positioned in all three axes x, y, z, in order to capture a single voxel, which makes it rather slow, if a full volumetric representation is to be acquired. The OCT based scanning devices exist in multiple adaptations of the original design, in order to achieve higher scanning speeds. Full-Field OCT (FF-OCT) makes use of a 2D array of detectors that can capture the entire (x, y) slice in a single measurement. The Fourier-Domain OCT (FD-OCT) and Swept-Source OCT (SS-OCT) utilize the properties of Fourier Transform to acquire full depth scans without movement of the reference arm along the axis, z [16].

The potential of the OCT technology for the fingerprint presentation attack detection scenario was researched by the project *OCT-Finger* [89]. The test group individuals were able to achieve almost 100% manual recognition rate on a large-scale database of OCT scans of genuine and artefact fingerprints. The study has demonstrated that, apart of the outer fingerprint pattern, the OCT technology has also the potential to capture the structure of the inner fingerprint tissues that are responsible for stability and regeneration of the outer fingerprint, as well as small internal skin structures such as sweat glands (Fig. 3.1).

The project has demonstrated that the OCT technology allows for analysis of multiple aspects that differentiate genuine and artefact fingers. The 3D representation of the outer fingerprint provides for more information than a classical 2D fingerprint scan. The sweat glands underneath could be detected and their helix-like structure, as well as other properties, verified. In genuine scans, the inner fingerprint pattern copies the pattern of the outer fingerprint and therefore successful comparison of the two patterns could provide for a strong evidence of a genuine finger scan. Other possibilities include verification of the scattering properties of the fingertip skin that potentially differs from the scattering properties of an artefact material. It can be assumed that replication of the internal structure and the scattering properties represented in an OCT scan by means of an artefact would be extremely difficult.

Nevertheless, an efficient liveness detection method based on volumetric scans of fingertips has to cope with a number of challenges. A volumetric OCT scan represents a significant amount of data that increases very quickly with its resolution. A scan of resolution $200 \times 200 \times 512$ voxels ($width \times height \times depth$) represents 19,5 MB of data and a scan of $1024 \times 1024 \times 512$ voxels 512 MB of data if a voxel is represented by a single byte. The acquisition time typically increases with the scanning resolution, which limits practically achievable resolutions. For practical applicability, all the data need to be captured and processed in a matter of a few seconds. As depends on the quality of the OCT scanner and the scattering properties of the fingertip skin, the resulting scan is subject to some amount of speckle noise along with a number of faulty measurements. The structure of the noise can vary slightly among the scanning devices, and the method should deal with the noise in device-independent fashion. The intra-class variability of properties of genuine human fingers is relatively large and an efficient classification method has to be able to reliably distinguish between the genuine structures and the structures achievable in artefact fingers. In order to reliably classify previously unknown artefacts, the method should validate properties of genuine fingers rather than try to detect anomalies caused by artefact fingers.

Based on the data collected in the framework of the *OCT-Finger* project, Menrath and Breithaupt [79] have proposed an automatic method for analysis and classification of the OCT scans into genuine and artefact ones. They preprocess the OCT volumetric scans by using 3D median filters to suppress the influence of the speckle noise and faulty measurements in the analysed

data. The filtered volume is then searched for the inner and outer fingerprint and sweat glands are attempted to be extracted. Due to 3D filtering of a large amount of data, the approach turned out to be an order of magnitude slower than required for practical application. Even though an attempt to perform massive parallelization of their method successfully resulted in a speed-up of an order of a magnitude, the method remains very computationally intensive, which limits its applicability to scans of larger resolutions.

3.3 Fingerprint Skin Layer Separation

3.3.1 Database

The OCT scan database used in this chapter has been composed within the framework of the *OCT-Finger* [89]. The OCT scanning device was based on the Fourier-Domain OCT (FD-OCT) technology with an acquisition time of $2.24s$ per scan and operating on a wavelength of $1300 \pm 55nm$. A scan represents $4 \times 4 \times 2.5mm$-large volume ($width \times height \times depth$) of the fingertip at a resolution of $200 \times 200 \times 512$ voxels.

The scans of genuine living fingers represent fingers of 226 subjects of which 96 (42%) were males and 130 (58%) females. The age structure has been as follows: 18 subjects (8%), 5-20 years; 172 subjects (76%), 20-60 years; 36 subjects (16%), 60-80 years. For each subject, at least the right thumb, the right index finger and the right little finger was scanned. Each finger instance was scanned 11 times, which provided for the minimum total amount of 7458 samples of genuine living finger scans.

The fake fingerprint scans represent 30 different classes of artefact fingerprints. The variation artefacts is caused by the mold material composition (gelatin, silicone, latex, window paint, wood glue etc.) and the artefact material composition (glycerol, graphite, window paint etc.). For each class, at least 9 artefact fingerprints were produced. Each of the artefact fingerprints was used to acquire at least 11 scans, yielding for minimum number of 2970 artefact fingerprint scans.

In addition to that, fingers of 5 male and 5 female dead bodies were scanned. For each body, 3 fingers were scanned, 11 times each, providing for 330 dead finger samples.

3.3.2 Scan Structure

As illustrated by Fig. 3.1, the OCT technology is able to capture the layered structure of the skin of human fingers. The scan captures a strong reflection from the boundary between the air and the outer fingerprint (Fig. 3.1b). The outer fingerprint layer is followed by a layer containing the sweat glands. Thickness of this layer as well as its scattering properties vary in the skin of different subjects. The amount of sweat glands also varies strongly among subjects. Some subjects can provide ten times more sweat glands than other

subjects and for some individuals the OCT scan is completely lacking any sweat glands. The layer containing sweat glands is followed by a layer that contains the inner fingerprint. The inner fingerprint (i.e. dermis boundary) is a cell structure responsible for stability and regeneration of the outer fingerprint. Unless the inner fingerprint is damaged, the outer fingerprint can fully regenerate to the original pattern. The structure of the outer fingerprint is typically a copy of the inner fingerprint (however, the thickness, clarity and strength of its reflection widely varies among subjects).

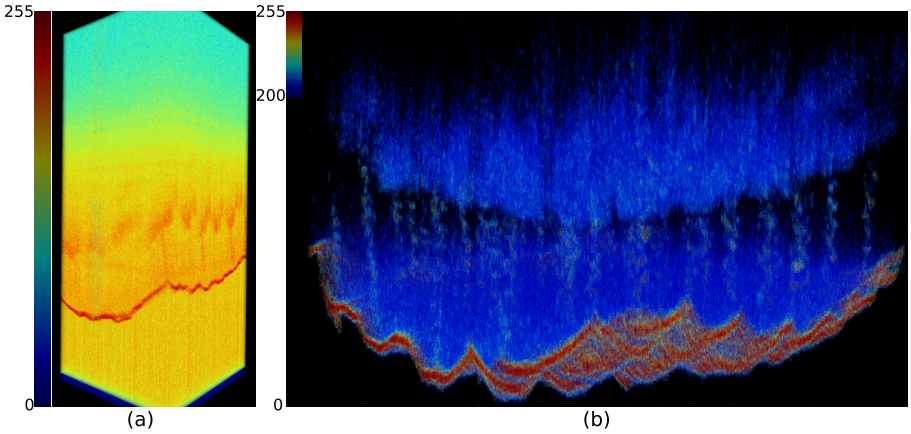

Figure 3.1: (a) OCT scan of a genuine finger (b) OCT scan of a genuine finger, thresholded 200+, heat-map scale change allows for clearer visualization of fine structures such as sweat glands

A typical structure of a scan of an artefact fingerprint differs in various aspects (Fig. 3.2) from the genuine counter piece. A thin layered artefact typically yields a strong reflection layer from its outer surface. The structure of the next layer depends on scattering properties and inner structure of the artefact fingerprint (Fig. 3.2a). Unless the artefact fingerprint is too thick or impenetrable for the OCT scanner, a second strong reflection of the boundary between the artefact and the genuine fingerprint appears. The following structure then copies the genuine fingerprint structure. If the artefact fingerprint is too thick or its material too difficult to penetrate for the OCT scanner, only an outer fingerprint reflection appears (Fig. 3.2b). The following layer of data represents scattering properties and inner structure of the artefact material (bubbles etc.). A second layer of the inner fingerprint does not appear, nor does it copy the pattern of the outer fingerprint.

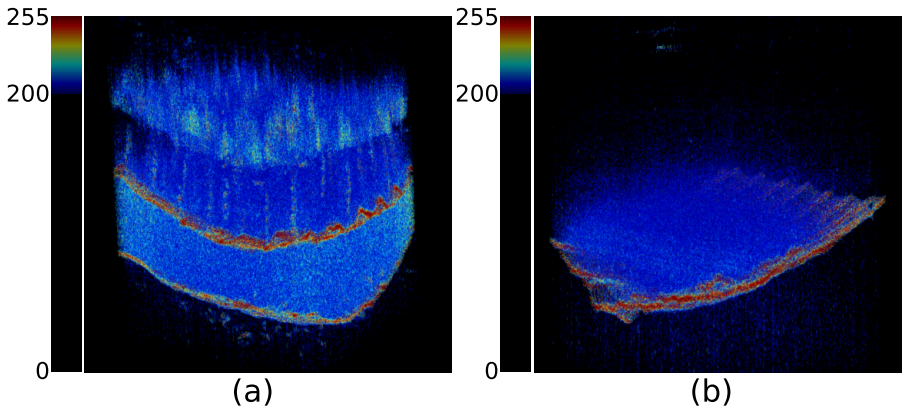

Figure 3.2: (a) OCT scan of a thin-layered artefact on a genuine finger (b) OCT scan of a thick artefact fingerprint

3.3.3 Automatic Method

In order to cope with the large amount of volumetric data in an OCT scan, the initial detection of positions of the specific layers in an OCT fingerprint scan should ideally avoid computationally expensive preprocessing of the data by 3D filtering. We propose a layer detection method robust to a certain degree of speckle noise and faulty measurements that can perform the initial layer detection directly. The volumetric scan, $V(x, y, z)$, of size, $w \times h \times d$, is analyzed as follows. A grid of size w_g and h_g is positioned over the (x, y) plane of the volume $V(x, y, z)$ (Fig. 3.3). Each grid cell yields a column volume, $C_{m,n}(x, y, z)$. From each of the columns, $C_{m,n}(x, y, z)$, a column accumulation function, $f_{m,n}(z)$, is computed as follows (Fig. 3.3):

$$f_{m,n}(z) = \sum_{x=0}^{\lfloor w/w_g \rfloor - 1} \sum_{y=0}^{\lfloor h/h_g \rfloor - 1} C_{m,n}(x, y, z) \tag{3.1}$$

For genuine living fingers, the shape of the column accumulation function $f_{m,n}(z)$ typically contains two intuitively observable peaks, one for the outer fingerprint and one for the inner fingerprint layer (Fig. 3.3). However, the two peaks are not always associated with the two main *global* maxima of the function. Due to noise in the volumetric data, one peak typically consists of multiple smaller peaks, while the actual center of the layer lies in the center of mass of the smaller peaks, rather than on one of them. A particular peak width range should be taken into consideration while searching for the peaks. In addition, the peaks themselves do not often form a maximum even in a smaller window of the function. They rather represent a sudden change on the shape of a function with an otherwise constantly growing or decreasing trend, typ-

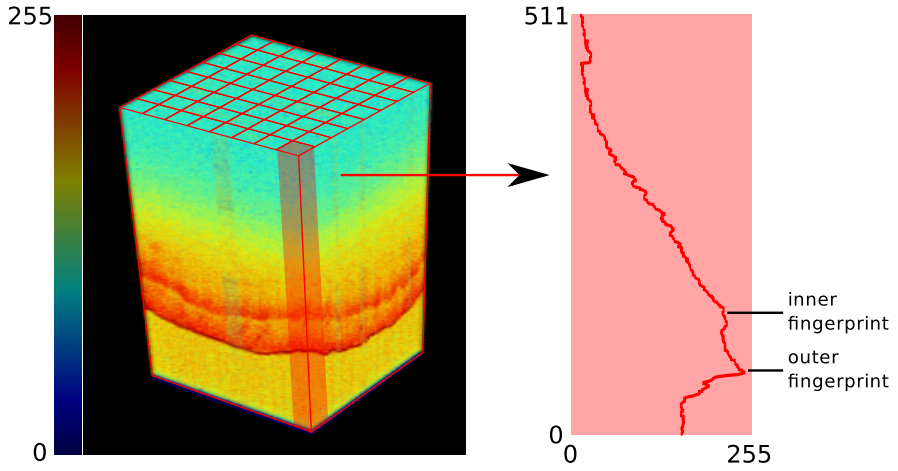

Figure 3.3: Extraction of the accumulation functions by means of a grid

ically a peak-like fluctuation that does not represent a maximum. Therefore, the peak localization method should look for the fluctuations taking the width range of the peaks into consideration and it should not be affected by the general slope of the function $f_{m,n}(z)$.

For an otherwise constant discrete function, $f(n)$, defined on interval, $[0, l-1]$, where l is a peak width parameter, a position p and an energy e of a single peak on its shape can be detected as the phase and amplitude of function f_p as follows (Fig. 3.4):

$$sn(n) = \sin(\frac{1}{2}\frac{2\pi}{l} + n\frac{2\pi}{l}) \tag{3.2}$$

$$cs(n) = \cos(\frac{1}{2}\frac{2\pi}{l} + n\frac{2\pi}{l}) \tag{3.3}$$

$$a = -\sum_{n=0}^{l-1} f(n)sn(n) \tag{3.4}$$

$$b = -\sum_{n=0}^{l-1} f(n)cs(n) \tag{3.5}$$

$$f_p = a \cdot sn(n) + b \cdot cs(n) \tag{3.6}$$

$$e = \sqrt{a^2 + b^2} \tag{3.7}$$

$$p = \begin{cases} \frac{atan2(a,b)}{pi}\frac{1}{2}l & atan2(a,b) \geq 0 \\ l + \frac{atan2(a,b)}{pi}\frac{1}{2}l & atan2(a,b) < 0 \end{cases} \tag{3.8}$$

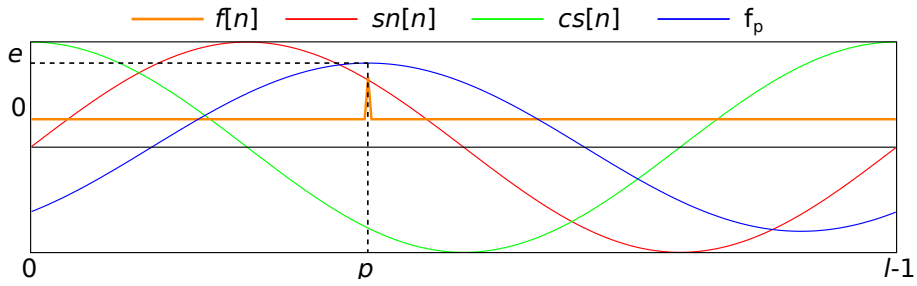

Figure 3.4: Peak detection for an otherwise constant function

However, if the discrete function, apart from the peak range, exhibits a constantly increasing or decreasing trend, the above mentioned method fails. Instead of pointing to the peak position, the method rather analyzes the strength of the global slope of the function $f(n)$. For an otherwise constantly increasing or decreasing function $g(n)$ defined on interval $[0, N-1]$ and $N = \frac{3}{2}l$, the following method can be used to detect a peak of energy e and position, p, as the phase and amplitude of function f_p (Fig. 3.5):

$$sn(n) = \sin(\frac{1}{2}\frac{2\pi}{l} + n\frac{2\pi}{l}) \tag{3.9}$$

$$cs(n) = \cos(\frac{1}{2}\frac{2\pi}{l} + n\frac{2\pi}{l}) \tag{3.10}$$

$$a = \sum_{n=0}^{l-1} g(n)sn(n) \tag{3.11}$$

$$b = \sum_{n=0}^{l-1} g(n)cs(n) \tag{3.12}$$

$$c = \sum_{n=0}^{l-1} g(n + \frac{1}{3}N)sn(n) \tag{3.13}$$

$$d = \sum_{n=0}^{l-1} g(n + \frac{1}{3}N)cs(n) \tag{3.14}$$

$$f_p = (c-a)sn(n - \frac{1}{3}N) + (d-b)cs(n - \frac{1}{3}N) \tag{3.15}$$

$$e = \sqrt{(c-a)^2 + (d-b)^2} \tag{3.16}$$

$$p = \begin{cases} \frac{atan2(c-a,d-b)}{pi}\frac{1}{2}l + \frac{1}{2}l & atan2(c-a,d-b) \geq 0 \\ l + \frac{atan2(c-a,d-b)}{pi}\frac{1}{2}l + \frac{1}{2}l & atan2(c-a,d-b) < 0 \end{cases} \tag{3.17}$$

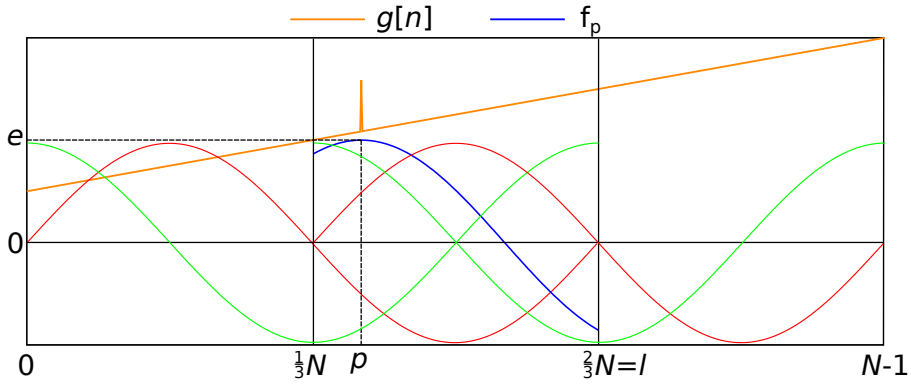

Figure 3.5: Peak detection an otherwise constantly increasing or decreasing function

The actual detection of positive fluctuations on the shape of a column accumulation function $f(n)$ defined on interval $[0, N_f - 1]$ is done by means of the following approach. The interval $[0, N_f - 1]$ is divided into overlapping windows $W_m = [m\frac{1}{4}l, m\frac{1}{4}l + \frac{3}{2}l - 1]$, where $m \geq 0$ (Fig. 3.6). For each window W_m the peak position p_m and energy e_m is computed using equations (3.9)-(3.17). Since $\sin(\alpha + \frac{\pi}{2}) = \cos(\alpha)$ and $\cos(\alpha + \frac{\pi}{2}) = -\sin(\alpha)$, the following set of equations can be used to efficiently compute a_m, b_m, c_m, d_m (eq. (3.11)-(3.14)) for a window W_m:

$$sns(o) = \sum_{n=o \cdot l/4}^{o \cdot l/4 + l/4 - 1} f(n) \sin(\frac{1}{2}\frac{2\pi}{l} + n\frac{2\pi}{l}) \tag{3.18}$$

$$css(o) = \sum_{n=o \cdot l/4}^{o \cdot l/4 + l/4 - 1} f(n) \cos(\frac{1}{2}\frac{2\pi}{l} + n\frac{2\pi}{l}) \tag{3.19}$$

if m is even:

$$a_m = \sum_{n=0}^{3} sns(m + n) \tag{3.20}$$

$$b_m = \sum_{n=0}^{3} css(m + n) \tag{3.21}$$

$$c_m = \sum_{n=0}^{3} sns(m + n + 2) \tag{3.22}$$

$$d_m = \sum_{n=0}^{3} css(m + n + 2) \tag{3.23}$$

if m is odd:

$$a_m = \sum_{n=0}^{3} -css(m+n) \tag{3.24}$$

$$b_m = \sum_{n=0}^{3} sns(m+n) \tag{3.25}$$

$$c_m = \sum_{n=0}^{3} -css(m+n+2) \tag{3.26}$$

$$d_m = \sum_{n=0}^{3} sns(m+n+2) \tag{3.27}$$

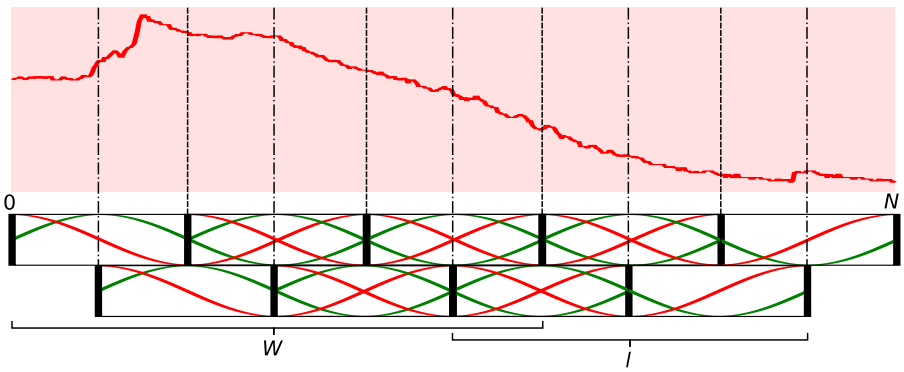

Figure 3.6: Overlapping windows for peak detection

Values of functions $sns(o)$ and $css(o)$ can be precomputed by a single multiplication of the analyzed function $f(n)$ with the function $sn(n)$ (eq. (3.9)), and the function, $cs(n)$ (eq. (3.10)), while storing the intermediate results. Each of the weights, a_m, b_m, c_m, d_m, can then be computed by adding 4 of these precomputed values. The method does not perform any convolution of any core function with the original function $f(n)$, which greatly reduces computational complexity as compared to a convolution based method. In addition the values of functions $sns(n)$ and $css(n)$ can be computed in parallel with no data overlap.

The windows W_m of length $\frac{3}{2}l$ are overlapping each other with an interval of $\frac{1}{4}l$. Consequently each of the windows W_m provides a reliable peak position p_m and peak energy e_m around its center in an interval of length, $\frac{1}{4}l$. If the detected peak position p falls outside of the central interval, it is discarded.

The peaks that are detected inside of the central interval of their detection window W_m are considered in the further processing. Depending on the settings, P peaks ($P = 2$ for detection of two layers) with highest energy e are stored.

By means of the above described method P peaks are detected for each column accumulation function $f_{m,n}(z)$ yielding for a sparse approximation of the position of the P most apparent layers in the scan volume $V(x, y, z)$.

3.4 Layer candidate points detection performance

Manual inspection of the genuine fingerprint scans has identified about 11% of the scans as being of insufficient quality due to non-compliant behavior of the capture subjects. Clearly visible anomalies such as sudden missing parts of the scans and discontinuities in the structure of the scans are related to the fact that the finger was not held still during the scanning period, it was put too close to the scanning surface or removed before the scanning was finished, etc.

An example of the results of the method applied to genuine fingerprint scans ($P = 2$) is shown in Fig. 3.7. For the genuine fingerprint scans without the anomalies related to the non-compliant subject behavior, the method successfully detected the outer and inner fingerprint layer in 90% of the scans (less than 5% outliers, sparsely distributed) with an average processing time of 0.02s in a single thread on a 3.6GHz 64bit CPU, as opposed to 56s in a single thread on a 2.5GHz CPU as reported by Menrath and Breithaupt [79]. The unsuccessful cases were caused by a very weak or completely missing representation of an inner fingerprint in the OCT scan. If the inner fingerprint was present to some extent, the method still did succeed to represent its position in most of the columns, generating more than 5% of outliers. In the scan, the inner fingerprint is represented as a scattered point cloud, rather than a continuous surface. The clarity and density of the point cloud varies among different subjects, from a very clear almost continuous representation to a complete lack of observable inner fingerprint, which causes the method to generate the largest number of outliers for the inner fingerprint layer.

Fig. 3.8 illustrates detection of 3 layers ($P = 3$) in a fake fingerprint scan.

3.4.1 Robust estimation of fingerprint layer positions

Using the above discussed approach, two sets of candidate points, S_{inner} and S_{outer}, are extracted from the original OCT scan, representing a densely assembled cloud of points that are - in a vertical perspective - centered around outer and inner fingerprint layers (Fig. 3.9a).

The resolution of $3 \times 3 \times 512$-voxel columns allows for obtaining the details of the fingerprint pattern captured by the OCT scan, both in terms of the outer and the inner fingerprint layers. However, the method by Sousedik et al. [101] generates a number of outliers. Especially for the inner fingerprint pattern, a large number of outliers is being generated, as some of the layer

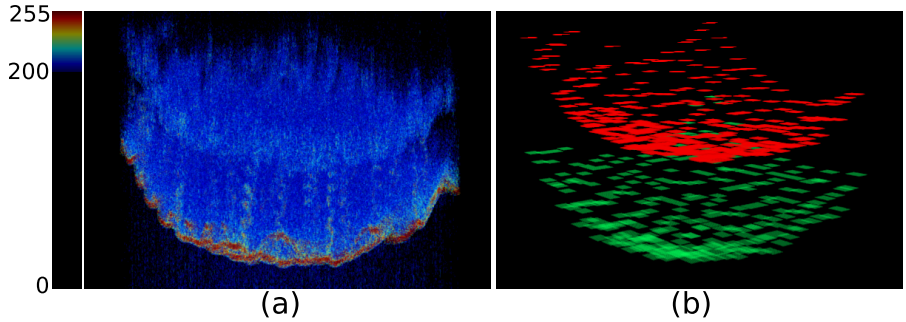

Figure 3.7: (a) OCT scan of a genuine finger, thresholded (b) Segmentation into 2 layers ($P = 2, l = 36$)

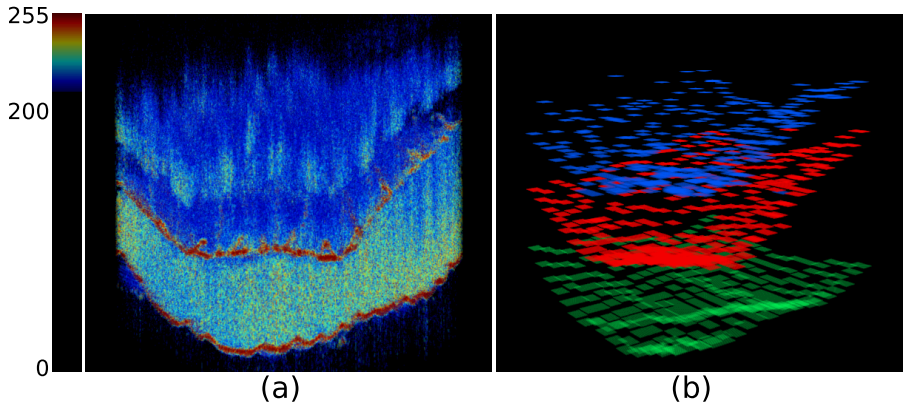

Figure 3.8: (a) OCT scan of an artefact finger, thresholded (b) Segmentation into 3 layers ($P = 3$, $l = 36$)

detection columns go through the fingerprint valleys, which, for the inner fingerprint, often do not generate significantly stronger responses as compared to the surrounding tissue (Fig. 3.9b). Nevertheless, a clearly sufficient number of correctly placed layer candidate points are found for both of the fingerprint layers, as long as the quality of the OCT scan is acceptable.

This fact suggests a statistical approach capable of fitting a smooth surface, $z = f^{(l)}(x, y)$, to the main cluster of the detected points, $\mathbf{x}^{(l)} = (x^{(l)}, y^{(l)}, z^{(l)}) \in S_{(l)} \wedge l \in \{inner, outer\}$.

However, there are number of challenges to cope with; Even though the strong and clear reflection from the outer fingerprint surface typically provides for a clearly identifiable layer, both of the candidate point sets, S_{outer} and S_{inner}, still contain a significant number of outliers whose influence on

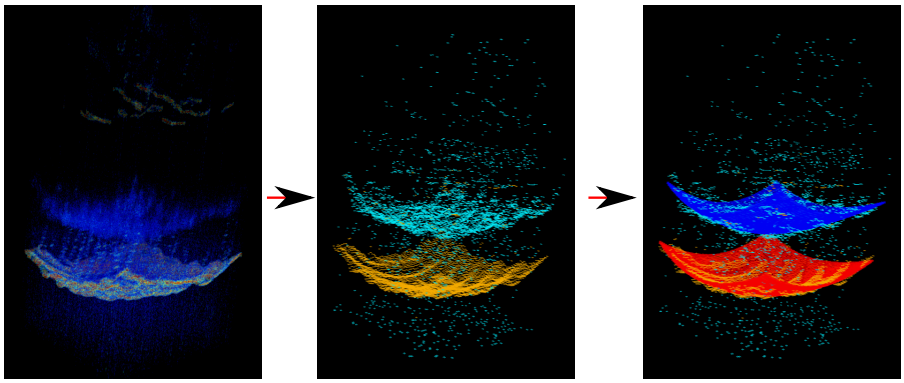

Figure 3.9: Pipeline of the estimation of the fingerprint layer positions (a) OCT scan of a genuine fingerprint (b) Initial candidate point sets; yellow $\rightarrow S_{outer}$, azure $\rightarrow S_{inner}$ (c) Smooth surfaces fitted to the main cluster of points in the candidate point sets; red $\rightarrow z = f^{outer}(x, y)$, blue $\rightarrow z = f^{inner}(x, y)$

the final smooth surface has to be eliminated (Fig. 3.9b). In addition, the non-outlier candidate points do not lie precisely on a smooth surface. For the outer fingerprint, the non-outlier candidate points, $\mathbf{x}_i^{outer} \in S_{outer}$, follow the 3D structure of the fingerprint, and hence these points vary around the desired smooth surface (Fig. 3.9c). For the inner fingerprint, the tissues are captured as a point cloud of stronger responses, providing for a somewhat randomly varying positions of the detected candidate points, $\mathbf{x}_i^{inner} \in S_{inner}$, after the initial layer estimation method has been applied at the higher resolution of 3×3 voxels wide columns (Fig. 3.9b). Given the strong time constraints required by practical applications, the resulting approach needs to provide for high accuracy of the fitting procedure at very limited computational costs.

The direct application of surface fitting methods, such as Levenberg-Marquardt [71], is sub-optimal, as this would yield inaccurate results due to the significant number of outliers present in the candidate points sets. The typically applied RANSAC-based approaches [21] are well-suited for dealing with outliers, however their efficiency and accuracy is sub-optimal if the non-outlier points do not lie very closely to the fitted surface. In addition, the RANSAC-based approaches require a clearly defined mathematical model of the fitted surface, with a limited number of degrees of freedom, if an efficient computation is expected. These properties do not support the application of the RANSAC-based approaches for this scenario, due to the number of degrees of freedom necessary to model the fingerprint surface, and the fact that the candidate points lie very rarely exactly on the fitted surface.

Followingly, we have developed a method for smooth surface estimation by means of an innovative procedure for neural network training. We have

modeled the smooth surface, $z = f^{(l)}(x, y) \wedge l \in \{inner, outer\}$, using a backpropagation neural network [39] with a single hidden layer containing 4 neurons, as illustrated by Fig. 3.10. The network consists of 2 input neurons, 4

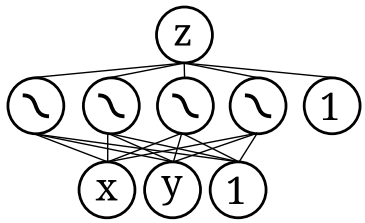

Figure 3.10: Structure of the fingerprint layer estimation neural network

hidden neurons, and one output neuron. Both the input layer and the hidden layer have each an associated bias neuron. This network is trained to effectively represent the smooth fingerprint surface as a function $z = f^{(l)}(x, y) \wedge l \in \{inner, outer\}$, where z represents the depth of the fitted surface at the point (x, y). All the hidden neurons consist of a Gaussian transfer function defined as $z = e^{-x^2 s^2}$, where s is the steepness value. The neural network's structure expresses the function $z = s(w_{12}e^{-(w_0 x + w_1 y + w_2)^2 s^2} + w_{13}e^{-(w_3 x + w_4 y + w_5)^2 s^2} + w_{14}e^{-(w_6 x + w_7 y + w_8)^2 s^2} + w_{15}e^{-(w_9 x + w_{10} y + w_{11})^2 s^2} + w_{16})$, and allows to represent the variations of the shape of the human finger surface, while disregarding the influences of the fingerprint pattern present in the outer fingerprint candidate point set, S_{outer}, or influences of the somewhat random variations present in the inner fingerprint candidate point set, S_{inner}. The limited number of neurons allow for a computationally inexpensive training procedure.

In order to successfully deal with the negative influences of the outlier candidate points, the neural network would have to converge to the main cluster of the candidate points, fitting an approximation surface to these points, while disregarding the influences of the outliers. This cannot be achieved by standard procedures for neural network training, as these standard procedures consider influences of all of the data points on the resulting surface.

We addressed the problem by developing the following training procedure:

1. Initialize the weights of the neural network such that it represents an average expected surface of the fingerprint
2. Perform k steps of the backpropagation training procedure in order to converge to a surface that represents all the candidate points, $\mathbf{x}_i^{(l)} \in S_{(l)}$, in a particular set, $l \in \{inner, outer\}$, including the outlier points ($k = 50$)
3. Perform one step of the backpropagation training procedure using the candidate point set $S_{(l)}$, with x and y normalized to $(0, 1)$

4. Evaluate the z-distance of the candidate points from the currently estimated surface, $d_i^{(l)} = |z_i^{(l)} - f^{(l)}(x_i^{(l)}, y_i^{(l)})|$, and remove the points whose distance is larger than d_{max} from the set $S_{(l)}$
5. Decrease the d_{max} by an amount Δd ($\Delta d = 0.075/n$)
6. Repeat the steps 3, 4 and 5, n times ($n = 50$)

The resulting functions denormalized into $[0, depth - 1]$, $z = f^{(l)}(x, y) \wedge l \in \{inner, outer\}$, represent the smooth surfaces fitted to the inner and outer fingerprint candidate points.

The above formulated algorithm represents a training procedure that causes the neural network gradually to disregard the influence of certain training data points as the training progresses. Thus the algorithm ensures that the surface, represented by the network, is converging to an approximation of the most significant cluster of the training data points. For the scenario analyzed in this paper, the network's surface converges to the main cluster of correctly identified candidate points, gradually disregarding the influence of the outliers in the course of the training (Fig. 3.9c). The detected outer and inner fingerprint of a good quality scan is shown in Fig. 3.11.

The above proposed approach for extraction of the layered structure of an OCT fingerprint scan provides a basis for automated assessment of its quality.

3.4.2 OCT scan quality estimation method

The agency that has kindly provided the *BSI-OCT-1-FINGER* database has indicated that OCT fingerprint scan quality problems were noted during the data collection [75]. Although high quality scans had typically been captured, a number of effects that are specific to the OCT fingerprint scanning procedure degraded the quality severely. A considerable subset of the capture subjects showed a tendency to lift their fingers too early from the sensor, or change their finger positions during the capture process. Especially, a pattern caused by irregular shaking of the fingers is commonly found in low-quality scans. For the current capture devices and their scanning durations, it is a challenge for the capture subject to hold the finger still during the scanning period, which can result in incomplete scans or strong distortions of the detected surfaces (see Fig. 3.12, 3.13). In addition, pressing the finger too hard against the scanner surface resulted in incomplete capturing of the layer surfaces in the acquired OCT fingerprint scans.

We have assigned the OCT-specific scan quality issues into two classes, namely $C_{strong-defect}$ and $C_{medium-defect}$. The first class takes into account large distortions, caused by lifting the fingers too early, strongly shaking the fingers and pressing them too hard against the surface of the OCT sensor. In such instances of non-compliant capture subject behavior, the OCT scans provide for sets of candidate points, S_{inner} and S_{outer}, where the distances, $d_{outlier}^{(l)}$, of the outlier points from the approximation surfaces, $f^{(l)}(x, y) \wedge l \in$

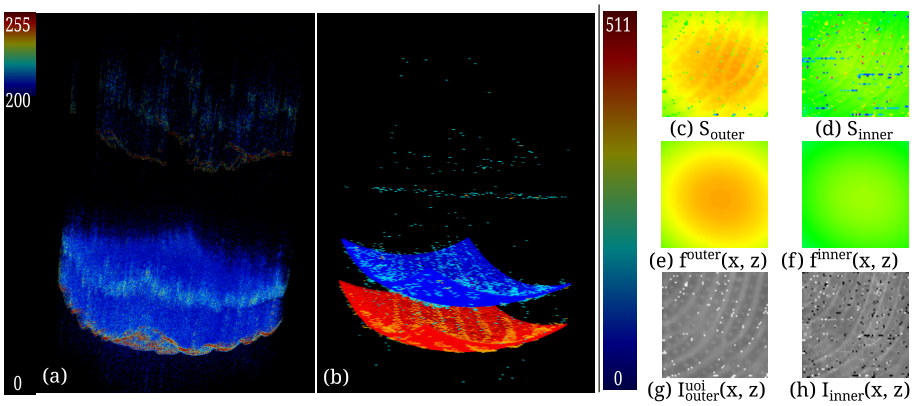

Figure 3.11: Visualization of the OCT quality estimation method for a a scan of excellent quality - outliers are caused almost solely by the OCT scan noise and the inherent unclarity of the inner fingerprint

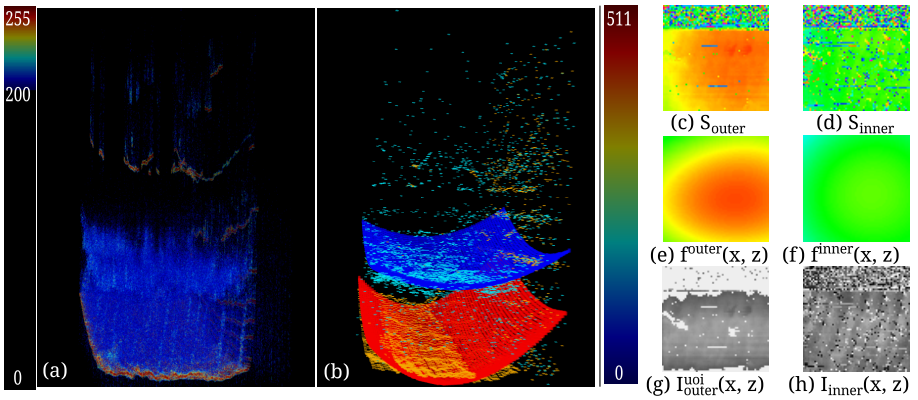

Figure 3.12: Visualization of the OCT quality estimation method for a scan, for which the scanned finger was lifted off too early from the sensor

$\{inner, outer\}$, will be much larger than the distances, $d^{(l)}_{inlier}$, caused by the presence of the fingerprint pattern in the outer fingerprint layer, or much larger than the random variations present due to the point-cloud nature of the inner fingerprint layer:

$$d^{(l)} = |z - f^{(l)}(x, y)| \wedge d^{(l)}_{outlier} > d^{(l)}_{inlier} \tag{3.28}$$

The second class of the scan quality problems, $C_{medium-defect}$, is related to slight shaking of the finger during the acquisition process (see an example in Fig. 3.14). In this case, the distances of candidate points, $d^{(l)}$, are within the

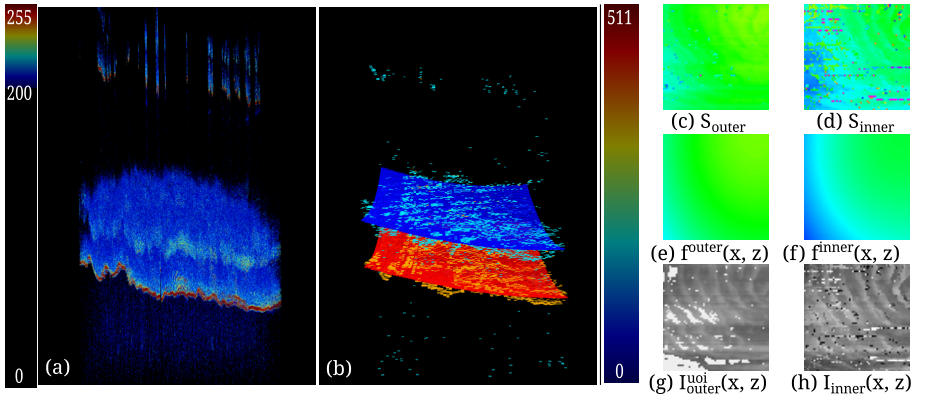

Figure 3.13: Visualization of the OCT quality estimation method for a scan that resulted from strong shaking the scanned finger

expected distance range:

$$d^{(l)} = |z - f^{(l)}(x, y)| \wedge d^{(l)} \leq d^{(l)}_{inlier} \tag{3.29}$$

Nevertheless, the variations can still be spotted due to the nature of the move-

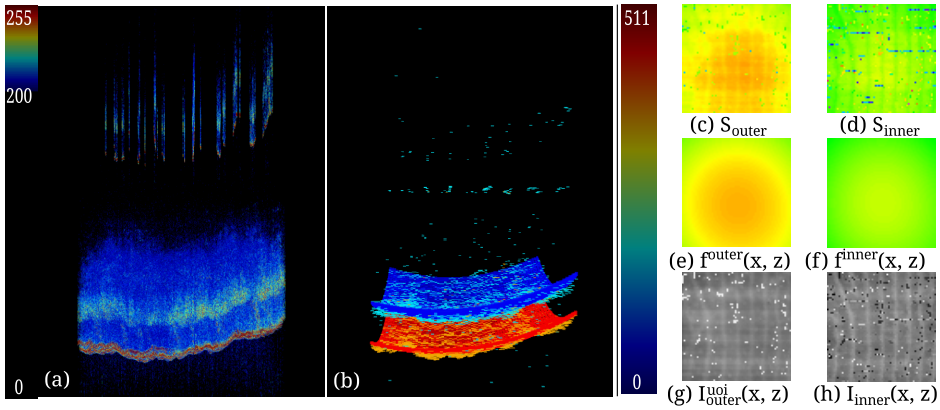

Figure 3.14: Visualization of the OCT quality estimation method for a scan that resulted from slight shaking the scanned finger

ment of the OCT scanning head. The scanning head moves very fast along one axis, but much slower along the opposite axis, as the latter's coordinate is adjusted upon completion of every single line scan. These variations can be approximated by the following equation that describes the z coordinate of the

layer candidate points, $(x, y, z) \in S_{(l)}$:

$$z_{LowQuality} = z_{real} + g(y) \tag{3.30}$$

where y is the coordinate that represents movement along the axis in which the scanning head moves slower, always upon completion of the scanning along the x axis. Due to the high speed of the head along the x axis, the resulting changes in positions of the layer candidate points can be approximated as being constant for every x coordinate. This provides for a shaking approximation function, $g(y)$, that describes the shaking pattern along the changes of the y coordinate.

For further analysis, we extract a 2D fingerprint estimation image for both the outer and the inner fingerprint, $I_{(l)}(x, y)$, as follows (Fig. 3.11(g) and (h)):

$$I_{(l)}(x, y) = z^{(l)} - f^{(l)}(x^{(l)}, y^{(l)}) \tag{3.31}$$

where $(x^{(l)}, y^{(l)}, z^{(l)}) \in S_{(l)} \wedge l \in \{inner, outer\}$.

Because the Fourier-Domain OCT (FD-OCT) scanning head captures the entire line-scan along the z axis at one point in time, the inner fingerprint estimation image, $I_{inner}(x, y)$, is subject to the same OCT-specific effects, caused by the non-compliant capture subject behavior, as the outer fingerprint estimation image, $I_{outer}(x, y)$. Due to the point-cloud nature of the inner fingerprint layer, the clearer, boundary-like outer fingerprint layer provides for a more reliable basis for the resulting OCT-specific quality estimation, while the inner fingerprint estimation image, $I_{inner}(x, y)$, can be used for further processing as regards fingerprint analysis and 2D-based quality detection methods.

The high-quality OCT scans can often be distinguished from the low-quality scans based on the number of outliers in $I_{outer}(x, y)$. However, these outliers typically represent various random depth values, which fact is not ideal in terms of considering the influences of the outliers equally. In order to unify the influences of the outliers, the image with uniform outlier influences, I^{uoi}_{outer}, is computed as follows:

$$I^{uoi}_{outer}(\mathbf{x}) = \begin{cases} I_{outer}(\mathbf{x}) & \text{if } |I_{outer}(\mathbf{x})| \leq \frac{1}{2} Fd_{max} \\ 250 & \text{if } |I_{outer}(\mathbf{x})| > \frac{1}{2} Fd_{max} \end{cases} \tag{3.32}$$

where $Fd_{max} = 30$ is the maximum depth of a human fingerprint, defined as slightly larger $(600\mu m)$ than the inter-ridge distance for the Caucasian population $(500\mu m)$ [64].

We define the first OCT-scan quality score, qs_1, that describes the class of more severe quality problems, related to lifting the fingers too early, pressing them too hard against the sensor surface or shaking them excessively. As our intention is to formulate a quality metric according [51], the qs_1 is defined as the amount of variations in y-axis frequencies lower than the frequency of the fingerprint, as follows:

$$qs_1 = 100 - \min(100, \frac{1}{2} \operatorname{std}(G_y(\frac{1}{width} \sum_{x=1}^{width} I^{uoi}_{outer}(x, y)))) \tag{3.33}$$

where G_y is a Gaussian filter, varying in y-axis only, ($\sigma = 7$) of size 1×11 pixels and std is the standard deviation.

The second quality score, qs_2, deals with the mild shaking of the fingers during the scanning period. Due to the model that has been described by the equation (3.30), a pattern is observable in the outer fingerprint image $I_{outer}(x, y)$ that resembles stripes of changing brightness added to the image (Fig. 3.14 (c) and (g)).

In order to minimize the influences of the outliers, the cleared image, $I_{outer}^{cleared}$, is defined as follows:

$$I_{outer}^{clared}(\mathbf{x}) = \begin{cases} I_{outer}(\mathbf{x}) & \text{if } |I_{outer}(\mathbf{x})| \leq \frac{1}{2} F d_{max} \\ M_{3\times 3}(I_{outer}(\mathbf{x})) & \text{if } |I_{outer}(\mathbf{x})| > \frac{1}{2} F d_{max} \end{cases} \tag{3.34}$$

where $M_{3\times 3}$ is a median filter of size 3×3.

Using the statistical properties of an image regarding the model (3.30), we describe the quality score qs_2 by means of ratios between means and standard deviations of y-lines in the derivation image $I_{dy}(x, y) \approx \frac{\partial I_{outer}^{cleared}(x,y)}{\partial y}$, defined as follows:

$$I_{dx}(x, y) = I_{outer}^{cleared}(x, y) - I_{outer}^{cleared}(x, y + 1) \tag{3.35}$$

The quality score qs_2 is the sum of energies of ratios between means and standard deviations of y-lines in the derivation image $I_{dx}(x, y)$, as follows:

$$qs_2 = 100 - \min(100, 10(\sum_{y=1}^{height-1} |\frac{\mathrm{mean}(I_{dx}(x, y), x \in (1, w))}{\mathrm{std}(I_{dx}(x, y), x \in (1, w))}|^3)^{\frac{1}{3}}) \tag{3.36}$$

This metric makes use of the rather constant changes of the pixel values in the cleared fingerprint image, providing for low standard deviations compared to the mean in the y-lines in $I_{dx}(x, y)$, as long as the shaking occurred during the acquisition procedure. In case of high-quality scans, no-stripes are present in the $I_{dx}(x, y)$ and the changes are rather random, generating high standard deviations in comparison to the changes of the mean.

3.5 Results

In order to test the relevance of the proposed quality metrics, the following protocol was applied.

3.5.1 Ground truth for OCT quality estimation

400 samples of OCT scans of genuine fingerprints were randomly chosen from the database, and manually classified by an expert into two groups, $G_{acceptable}$ and G_{bad}, adhering to strict criteria as follows: (i) If some of the points on the outer fingerprint surface in the scan were closer than 30 voxels along the z-axis to the bottom of the volume, the scan was assigned to the group G_{bad}, as the scanner is unreliable in the part of the volume where $z \in (0, 30)$, and the

situation results from the scenario when the finger was pressed too close to the surface of the sensor. (ii) If the surface of the outer fingerprint, as represented by the OCT scan, is suddenly discontinued after a specific value of the y-coordinate, the scan is assigned to the G_{bad} group (Fig. 3.12). Such a discontinuity pattern in the scan corresponds to lifting of the finger during the capture process. (iii) In order to describe the situation, where the strong shaking of the fingers occurred during scanning process, the scans are assigned to the G_{bad} group according to the following criteria; 1. The fingerprint surface is obviously disturbed by a function determined by a y-coordinate only. 2. The amplitude of the disturbances is clearly larger than than the amplitude of the ridge/valley pattern

All of the scans that do not satisfy any criteria required for the G_{bad} group, are considered to be of acceptable quality and assigned to the group $G_{acceptable}$.

3.5.2 Synthetically controlled OCT quality degradation

In order to perform synthetic degradation of the OCT scan quality, the pipeline of the layer estimation method is altered as follows. The outer fingerprint candidate-point set, S_{outer}, is extracted, representing the original high-resolution details of the surface of the outer fingerprint (Fig. 3.9b). A controlled quality degradation method is applied to the set, defined by the following equation ($Fd_{max} = 30$):

$$z = z + a(Fd_{max}SUR(\lfloor y/10 \rfloor) + 0.25Fd_{max}SUR(\lfloor y \rfloor)) \tag{3.37}$$

The function $SUR(x)$, generates random numbers from a uniform distribution, $SUR(x) \in (-0.5, 0.5)$, and cubically interpolates between $SUR(\lfloor x \rfloor)$ and $SUR(\lfloor x + 1 \rfloor)$, if a non-integer value, $x \neq \lfloor x \rfloor$ is requested. The term, $Fd_{max}SUR(\lfloor y/10 \rfloor)$, models the strong shaking pattern, while the second term, $Fd_{max}SUR(\lfloor y \rfloor)$, models the weak shaking pattern, whose variations are lower than the variations caused by the fingerprint pattern. The coefficient a represents amount of the degradation applied, where $a = 0$ represents no degradation and the original pattern is kept. After the degradation of S_{outer} is performed, the method normally proceeds with estimating the smooth surface f_{outer}.

3.5.3 OCT scan quality estimation

In order to assess relevance of the qs_1 quality score, one evaluation on synthetically degraded scans was carried out, along with one evaluation on the real low-quality scans. For the first scenario, the degradation model from the equation (3.37) was adopted.

If measured as the average distance between the estimated layer positions and the candidate point positions, $d_{outer} = \text{mean}(|z - f^{outer}(x, y)|) \wedge (x, y, z) \in S_{outer}$, the layer estimation method, run on the scans in $G_{acceptable}$, has achieved average d_{outer} of 3.06 with the standard deviation of 1.20.

The Fig. 3.15 illustrates the correlation, $c = -0.96$. between the level of the quality degradation, a, and the value of the quality score qs_1.

The real data evaluation was performed by assessing the ability of the quality score qs_1 to distinguish between the scans in the group $G_{acceptable}$ and the scans in the group G_{bad}, reported as false detection rates, as shown by Fig. 3.16.

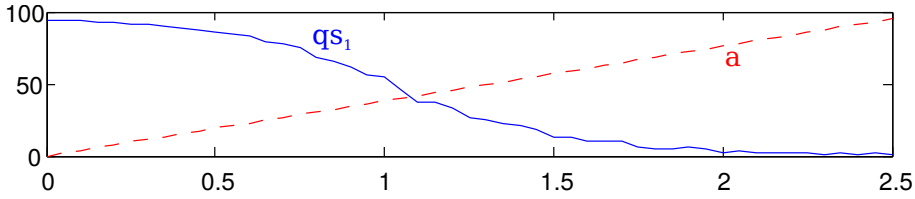

Figure 3.15: Quality score results on synthetically degraded data, a - quality degradation level, qs_1 - severe quality issues score

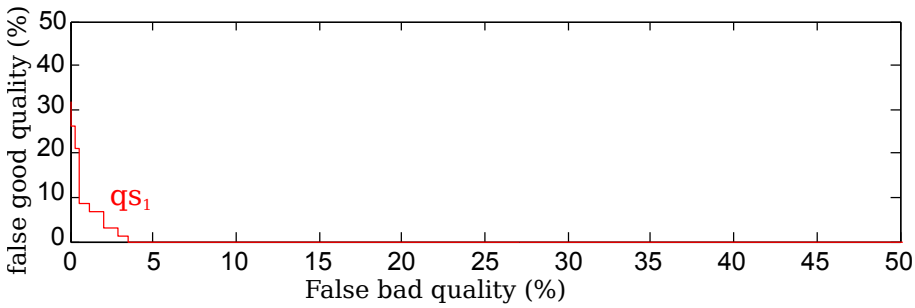

Figure 3.16: Detection results for the expert labeled ground truth data in terms of distinguishing between $G_{acceptable}$ and G_{bad} using the metric qs_1

A rigorous assessment of the relevance of the quality score qs_2 is challenging, as this score describes the fine variations caused by the slight shaking of the finger during the scanning, which variations are smaller than the variations caused by the presence of the fingerprint ridges and valleys. Nevertheless, the scans in the group $G_{acceptable}$ were further manually classified, which classification was based on whether they contain a pattern caused by addition of a function depending solely on the y-coordinate. Such a pattern is observable by a closer examination of the scan, as the fingerprint pattern still appears disturbed by the weak shaking pattern in the y-coordinate only (Fig. 3.14). The classification results for the metric qs_2 are illustrated by Fig. 3.17.

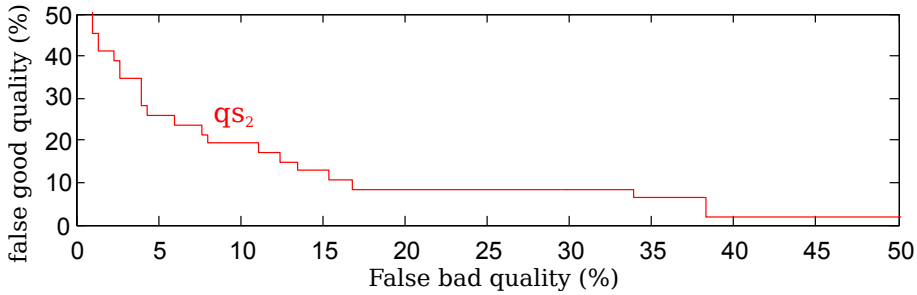

Figure 3.17: Results of detection of slight shaking of the scanned finger using the metric qs_2

3.6 Conclusions and future work

A reliable method for statistical approximation of the layer surfaces in an OCT fingerprint scan has been developed, allowing for extraction of the outer and inner fingerprint patterns. The method functions with a mean estimation error of 3.06 voxels and a standard deviation of the estimation of 1.2 voxels, which provides for a solid basis for extraction of the fingerprints into 2D representations. Two OCT-specific quality scores have been developed that enables discarding the low-quality scans that have resulted from a non-compliant capture subject behavior. For the more severe cases, the qs_1 allowed for detection of 98% of low-quality scans with a false detection rate of 3%.

The future work should focus on the application of the layer surface approximation method as a basis for the sweat gland identification and the subsequent verification of their genuine structure, providing for a reliable PAD method. The combination of the OCT-scan quality method proposed by this paper and a reliable PAD method would provide for a solid foundation for secure and reliable OCT-based fingerprint identification. A large-scale data collection performed by means of a high-quality OCT device of a larger scanning area is planned in the framework the project *OCT-Finger-II*. The full-area fingerprints that can be extracted from the resulting database will enable validation of the proposed quality scores in terms of the correlation with fingerprint recognition accuracy as defined in [51].

Chapter 4

Full Fingerprint OCT sensor

4.1 Summary

This chapter, based on the papers by Breithaupt et al. [12] and Sousedik & Breithaupt [99], describes an OCT sensor prototype designed specifically for fingerprint sensing. The original proof of concept was developed in terms of the project OCT-Finger-II [12]. Afterwards, the design underwent major improvements in terms of the OCT-Finger-II project and the following OCT-DATA project [99] organized by the German Federal Office for Information Security (BSI). The contribution in terms of OCT-Finger-II consists of developing the original proof of concept, and a follow-up full re-design of the scanning head. The contribution in terms of OCT-DATA involved full re-write of the scanner-control & visualization software, such that the level of long term stability required for successful data collection could be achieved. It also involved a major improvement of the sensor in terms of hardware components. With the significantly improved and stable design, a high-resolution dataset of OCT scans has been collected from a 2x2 cm area along with 2D fingerprints from identical capture subjects, in order to allow for further developments in terms of extraction of full fingerprints that could be handled by the existing commercial 2D fingerprint matchers.

4.2 Related work

With a few exceptions, the existing research regarding OCT fingerprinting focuses on using existing OCT setups and addressing the signal processing challenges (see Chapter 2, Section 2.5.2, OCT), rather than development of a specific-purpose OCT fingerprint sensor. Regarding an effort to develop a specific-purpose fingerprint OCT sensor with a scanning area sufficient for reliable fingerprint identification, Auksorius & Boccara [5, 6] have taken an approach using Full-Field (FF) OCT in the framework of the INGRESS project [1]. Unlike the FD-OCT OCT setups, which separately capture in-depth scanlines at high speed, the FF-OCT captures a 2D image at once, from a single specific depth using a 2D camera. This approach requires pressing the fingerprint against a glass surface, so that the curvature of the outer and inner fingerprint is flattened. According to earlier studies [74, 76], this comes with disadvantages regarding fingerprint scanning under difficult conditions (dry,

wet, greasy fingers etc.) similar to those faced by the existing 2D sensors. In addition, the readily 2D information extracted from the finger does not contain as many PAD-related cues as a full 3D volumetric scan, even though it leads to smaller data amounts and as such carries the potential for faster operation.

4.3 OCT Fingerprint Scanner Setup

Our fingerprint scanner setup is based on the Fourier-Domain OCT (FD-OCT) imaging technique as illustrated by Fig. 4.1.

4.3.1 FD-OCT scanning

As designed in original proof of concept [12], the illumination is generated by a super-luminescent diode (SLD), operating in an infra-red spectral band of 800-900 nm, coupled into a fiber optic arm of a fiber-optic coupler with a splitting ratio of 50:50. The light travels via the fiber-optic coupler into the scanning head, where it is collimated into a light beam with diameter of 3.9mm (2.6mm in the original design from [12]). The light travels from the fiber-optic collimator into a 50:50 beam splitter, such that 50% of the light travels through with unchanged trajectory as the sample beam and 50% of the light is deflected at a $90°$ angle into the reference arm as the reference beam.

The sample beam is deflected by a setup of 2 mirror galvanometers, which enable deflection of the beam in two orthogonal axes. The deflected sample beam is then focused by an objective lens system, so that for any deflection setting of the mirror galvanometers in a certain range, the beam leaves the lens in a vertical direction and is point-focused at a distance from the objective, which equals to its focal length.

In a limited distance range from the point of focus, the sample beam is sufficiently narrow to allow for the high-resolution imaging purposes. The narrowed sample beam travels into the scanned finger and is scattered both on its surface and in the skin underneath the fingerprint surface. A certain portion of the scattered light is reflected back as rays taking exactly the same range of trajectories that have been taken by the rays of the sample beam itself, which re-couples the light back into the optical setup, deflecting the light rays, reflected back from the finger, into the same optical elements in reverse order.

In the reference arm, the reference beam leaves the beam splitter and is reflected back into the system, after having its intensity significantly reduced by an adjustable setup. This intensity reduction setup allows matching the strongly reduced intensity range of the sample light that has been scattered in the finger, and as such only partially reflected back into the optical setup.

The sample beam, back-reflected from the finger, and the reference beam - after their re-coupling in the beam splitter - optically interfere. The interfered re-combined light travels back into the fiber-optic coupler and is measured by a spectrometer operating in the proper range of 800-900 nm.

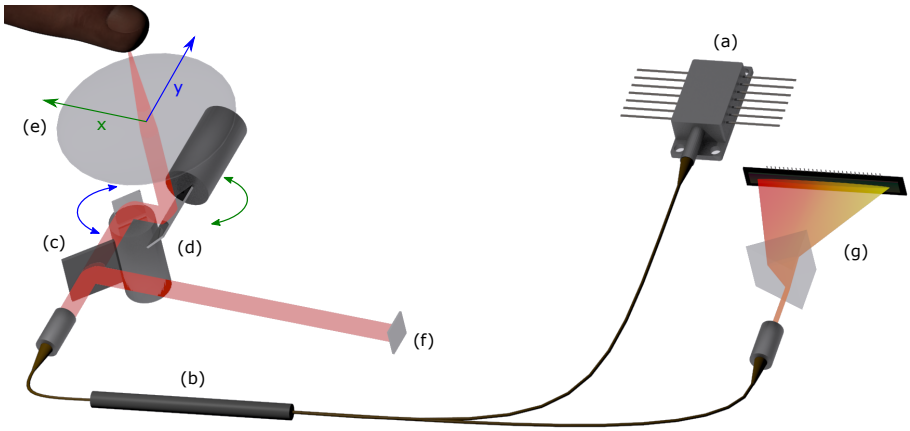

Figure 4.1: Schematic depiction of our FD-OCT fingerprint scanner: (a) SLD 800-900 nm light source, (b) fiber coupler, (c) beam splitter, (d) mirror galvanometers, (e) objective lens, (f) reference arm back-reflector, (g) 800-900 nm spectrometer

A single measurement taken by the spectrometer allows obtaining a 1D depth profile, $d(z)$, of the scattering properties of the scanned finger, at the current position of the sample beam, in the following manner. The spectrometer records a spectral profile $p(\lambda)$, where λ is the wavelength in the range of 800-900 nm. If no finger is present, no sample light is back-reflected into the system, and the profile $p(\lambda)$ equals the spectral profile of the back-reflected reference light $p_r(\lambda)$. If a scanned finger is present, the specific measured intensities in the interference profile, $p(\lambda)$, are equal to the reference spectral profile altered by the interference pattern, $p_i(\lambda)$, due to interference of the reference light with the back-reflected sample light:

$$p(\lambda) = p_r(\lambda) + p_i(\lambda) \tag{4.1}$$

By subtraction of the reference spectral profile, $p_r(\lambda)$, from the measured spectral profile $p(\lambda)$, it is possible to obtain the interference pattern $p_i(\lambda)$ - which depends primarily on the scattering properties of the scanned finger in the currently measured depth profile, $d(z)$.

In order to obtain the depth profile, $d(z)$, the wavelength-dependent intensities, $p(\lambda)$, must be transformed into frequency-dependent intensities, $p_i(f)$. The depth profile, $d(z)$, equals the modulus of Fourier transform of the interference pattern, $p_i(f)$.

$$d(z) = |\mathscr{F}(p_i(f))| \tag{4.2}$$

Intuitively, for all sample illumination waves of wavelength λ, the reflected wave is a superposition of the waves as reflected from the entire depth pro-

file of the scanned sample - the reflected wave represents a complex number determined by the integral of the illumination wave and the entire depth profile of the finger. During the interference with the reference beam, the measured intensity, $p(\lambda)$, is increased or decreased by interference with the reflected wave by $p_i(\lambda)$ - the real part of the complex integral. As such, a set of measured intensity changes for different wavelengths λ represents the real numbers resulting from a Fourier Transform of the scanned depth profile.

The measured interference profile, $p_i(f)$, represents only the real valued part of the Fourier Transform, $\mathscr{F}(d)$, of the depth profile, $d(z)$. This does not allow for unambiguous reconstruction of the depth profile, $d(z)$. In practice, the scanned sample is positioned above the focal plane only, which is equivalent to a depth profile with the first half equal to 0. Such a depth profile can be reconstructed unambiguously at $1/2$ of the spectrometer's resolution (using the modulus of the Fourier Transform in Eq. 4.2).

4.3.2 3D volumetric data acquisition

In order to obtain a 3D volumetric representation of the entire fingerprint, a depth profile $d(z)$ has to be acquired for each x and y coordinate of the scanning area.

An analog waveform, $V_x(t)$ resp. $V_y(t)$, is generated by an analog signal generator for each of the axes xy. For each axis xy, the momentary voltages in the waveform represent a specific rotation of the mirror galvanometer at a specific point in time t - which allows for sequential adjusting of the specific xy coordinates of the scanning beam.

A shared synchronization clock is used to activate the camera shutter of the spectrometer as well as the generation of the next sample, $(V_x(t), V_y(t))$, which adjusts the position of the mirror galvanometers into the new xy coordinate by means of a controller circuit.

The programmable analog waveform generator allows for the xy coordinates of the sample beam to be chosen in software, which fact enables software-controlled adjustments of both the lateral resolution and the scanning area of our setup.

4.3.3 Scanning head

In our setup, the fingerprint is scanned in free air, in contrast to pressing the finger against a surface, such as glass [5]. This design feature results from the findings of earlier studies, which have shown that scanning the finger pressed against a glass surface mitigates the ability of the OCT scanner to capture the surface fingerprint under difficult conditions (wet, greasy, etc. fingers) in a very similar fashion to existing 2D sensing technologies [74, 76].

Our scanning head allows resting the finger, while simultaneously leaving the fingerprint area in free-air. This design allows the OCT scanner to capture a 3D volumetric representation of the finger, without having to deal with loss

of the fine fingerprint structure due to the pressing the finger against a flat surface.

In the oiginal proof of concept of our FD-OCT fingerprint scanner [12], illustrated by Fig. 4.2, the scanning head contained the optical elements arranged in a highly flexible and easily adjustable setup. However, the OCT requires highly precise positioning of the optical elements, and as such the flexible setup limited the portability and long-term stability of the scanner, which was required for reliable data collection.

(a) measurement head - size: $250 \times 150 \times 304mm$

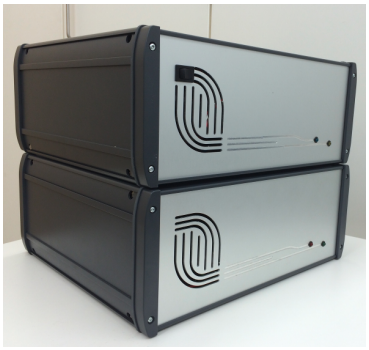

(b) OCT base device and a processing PC unit (replaceable by a PC) - unit size: $356 \times 150 \times 304mm$

Figure 4.2: First version of our OCT fingerprint scanner prototype [12]

In the current design [99] of the scanning head, illustrated by Fig. 4.3, the module contains the beam collimator, beam splitter, the reference arm, the galvanometers and the lens objective. The optical elements are fixed in precise positions in an aluminum block, which has been CNC-machined/drilled[1] in order to contain the correct cavities necessary for the optics path as well as the precise fixed positioning of the optical elements. This allows for a much more robust solution that greatly reduces the risk of the loss of calibration during transport as well as greatly supports the long term stability of the setup.

In terms of the OCT-DATA project, we exchanged the mirror galvanometers, the galvanometer controllers as well as the associated electrical coupling in order to greatly simplify the process of calibration of the scanning area and improve the long-term stability of the design. We also replaced the original beam collimator by a different model with a wider 3.9mm beam radius.

[1]Computer numerical control (CNC) is a computer controlled approach to material machining and drilling

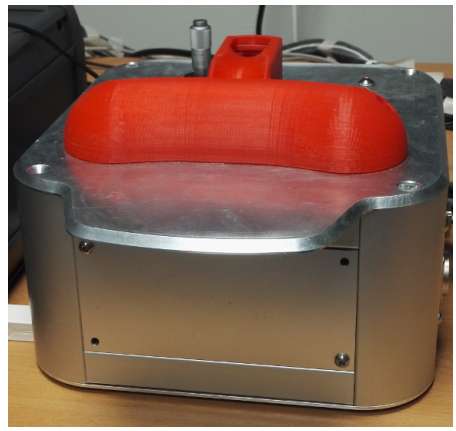

Figure 4.3: Second version scanning head of the FD-OCT fingerprint scanner [99]

4.3.4 Main & processing module

Currently [99], the main module contains the SLD light source, the spectrometer and the FPGA-based control circuitry necessary for real-time synchronization of the movement of the mirror galvanometers and the shutter of the spectrometer. The main module is connected to a PC unit with a GPU for processing & visualization purposes.

During the scanning, the spectrometer transfers 2048 pixels measurements at a 12-bit precision with a line-rate of 100 kHz over a CameraLink interface to the RAM of the processing PC - this gives a throughput of about 293 MB/s. This allows, together with the waveform generators operating at 100 kS/s[2], capturing a volumetric scan of the fingerprint at a lateral resolution of 512 DPI in our 2x2 cm scanning area in 1.63 s.

In terms of the OCT-DATA project, we updated the electrical coupling inside the main module and added additional EM-shielding features. We also replaced the fiber-optics coupling between the spectrometer, the SLD light source and the beam collimator in the scanning head.

4.4 Testing & Results

A significant challenge associated with 3D volumetric scanning of the fingerprint lies in the generated data amounts. During the operation, the spectrometer of 100 kHz line-rate and 2048 pixels per lines rate generates - 100K x 2048 x 12bit - about 293 MB/s of data, where each scan-line needs to be processed

[2]kilo-Samples/s (kS/s) - the amount of distinct outputs generated by the waveform generator per second

by Fourier Transform in order to obtain the depth profile $d(z)$. In our current setup, a single core i7 processor in the PC module processes the data in a multi-threaded pipeline during the scanning process itself, and is able to perform the FFT inversion slightly faster than the spectrometer generates the raw data. As such, the pipelined FFT inversion provides a readily processed spatial volumetric representation of the fingerprint practically immediately after the end of the scanning process.

In comparison with related attempts for OCT-based subsurface fingerprint scanning using FF-OCT [5], our FD-OCT setup allows for software adjustments of the scanning resolution. This enables performing a lower-resolution scan of the entire fingerprint (1.63 s at 512 DPI, current standard fingerprint resolution), extracting the outer fingerprint and inner fingerprint, allowing for superior reliability under difficult conditions (dry, wet, greasy fingers etc.). Immediately afterwards, a higher-resolution scan of a partial area can be acquired, for the purposes of reliable detection of fake fingerprints - PAD.

4.4.1 Scanner software

In the original proof of concept [12], the scanner software was equipped with a 2D preview mode, that was able to scan and visualize a single 2D slice of the scanned finger several times per second. This feature posed significant limitations regarding the data collection, since it did not allow to conveniently control the correct positioning of the scanned finger. In addition, visualization of the actual high-resolution scans required extra steps of running the FFT inversion of the spectral data into the spatial data and viewing using an external tool, which was not was not suitable regarding the time constraints in our data collection. The level of long-term stability of the original software was also insufficient for our data collection.

In terms of the OCT-DATA project, the software has been fully re-developed. The software has been equipped with a 3D preview mode, in which the the scanner repeatedly scans a low-resolution volume of 128 x 128 x 1024 voxels with an area of 2x2 cm and the volume is readily FFT-processed in a pipeline and visualized using a GPU at semi-realtime speed of 5 scans per second. The software also visualizes the high-resolution 3D fingerprint scan directly upon the end of the scanning process - using a FFT-inversion pipeline operating in parallel with the scanning process and GPU-based volume rendering. Both the preview mode and the high-resolution visualizations allow to view the 3D volume freely from any angle, which allows controlling the positioning of the finger as well as examining the scanned result. In addition, it is possible to visualize the spectral data and the 2D spatial slices of the scanned volume both in the preview and the high-resolution scanning mode.

4.4.2 Collected dataset

To evaluate our fingerprint scanner setup and make future research of the behavior and properties of the OCT scans of human fingerprints possible, we have collected the following dataset:

- fingerprint volume of 1408 x 1408 x 1024 voxels
- 2 x 2 cm scanning area
- 14.2 μm lateral resolution
- 720 fingers
- 72 participants
- all 10 fingers per participant

A single volumetric scan of a finger in this dataset (so that the offline research of the FFT processing pipeline is possible as well) requires the storage of 2048 pixels x 1408 x 1408 x 12bit (stored as 16bit) - 7,6 GB of raw spectral data. In addition, the processed spatial data, readily available upon the end of the scanning, are stored - 1024 x 1408 x 1408 x 8bit - 1.9 GB. This results in a total dataset size of - 720 fingers x 9.5 GB - 6.6 TB.

From an identical set of participants, 2D fingerprints of 52 participants inclusive 10 fingers have been collected using a standard optical 2D sensor, in order to allow for studies of compatibility of the OCT fingerprints and the standard 2D fingerprints.

In addition, the following high-resolution dataset of partial fingerprints has been collected, to enable a study of human skin behavior under high-resolution OCT, primarily for the purpose of fake fingerprint detection (PAD):

- fingerprint volume of 512 x 512 x 1024 voxels
- 3.58 x 3.58 mm scanning area
- 7 μm lateral resolution
- 156 fingers
- 52 participants
- right-hand thumb, index and ring finger per participant

Despite the relatively large data sizes, our experiments indicate the speed of the computer RAM, the Cameralink interface and further processing on GPUs (320 GB/s raw data throughput for standard gaming GTX 1080) would allow for scanning & processing speeds necessary for acquisition and processing in a matter of seconds at medium resolutions.

4.4.3 Visualizations

The OCT scans as captured by our first version scanner design 1.0 [12] are visualized by Fig. 4.4. Fig. 4.4a-c illustrates the imaging quality at which the sweat glands and the inner fingerprint were possible to capture by the first version scanner design.

The imaging quality achieved by our improved second version setup 2.0 is illustrated by Fig. 4.5-4.10.

Fig. 4.5-4.6 and Fig. 4.7-4.8 represent a 3D transparent visualization of an index finger resp. thumb. The sweat glands are visible under the transparent-rendered outer fingerprint. Visualization of the outer fingerprint, sweat glands along with the inner fingerprint layer are shown by Fig. 4.9-4.10. A vertical cut through a fingerprint scanned from a 2x2cm area is illustrated by Fig. 4.9, while Fig. 4.10a represents an identical fingerprint, visualized from the side as a highly-transparent 3D volume. Fig. 4.10b represents a vertical cut through a partial fingerprint from a 3.58x3.58mm area.

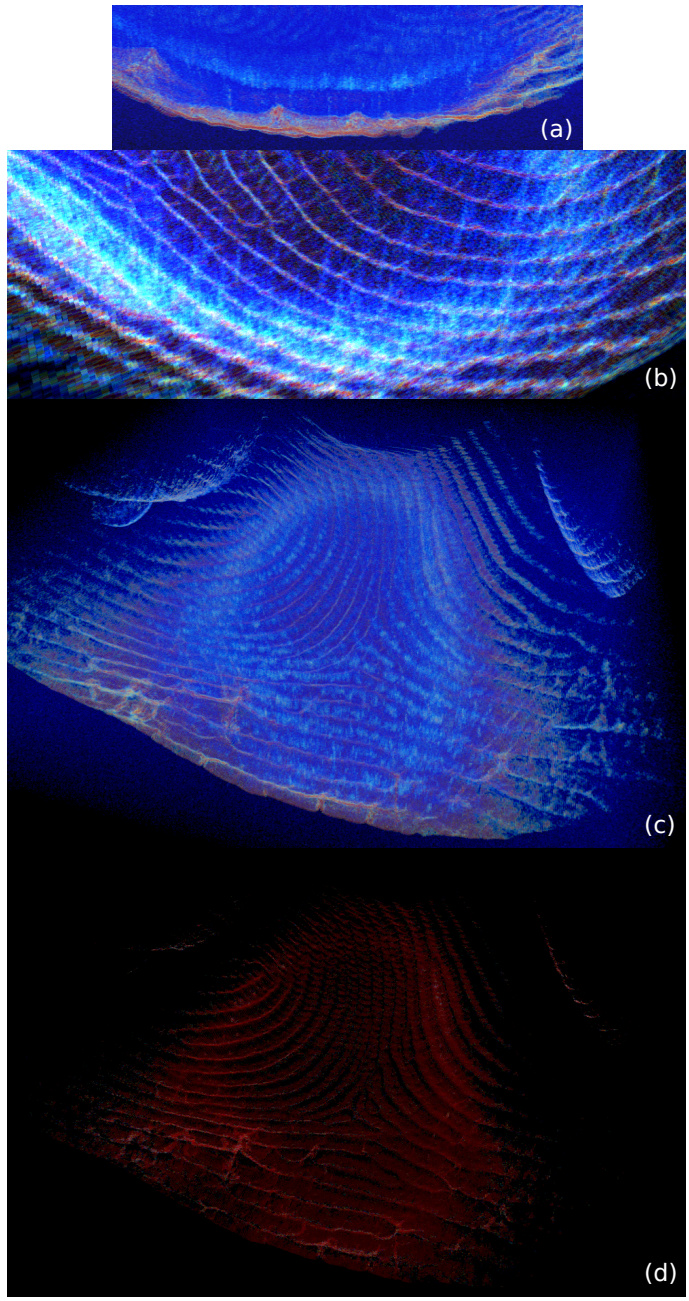

Figure 4.4: For comparison; OCT scan visualizations from the original proof of concept - OCT fingerprint scanner 1.0 [12]; (a)-(b) sweat glands, (c) inner fingerprint, (d) outer fingerprint

Figure 4.5: OCT scanner 2.0; index finger scan: 2x2cm area, 1408x1408x1024, 14.2μm - sweat glands overview - transparent 3D visualization

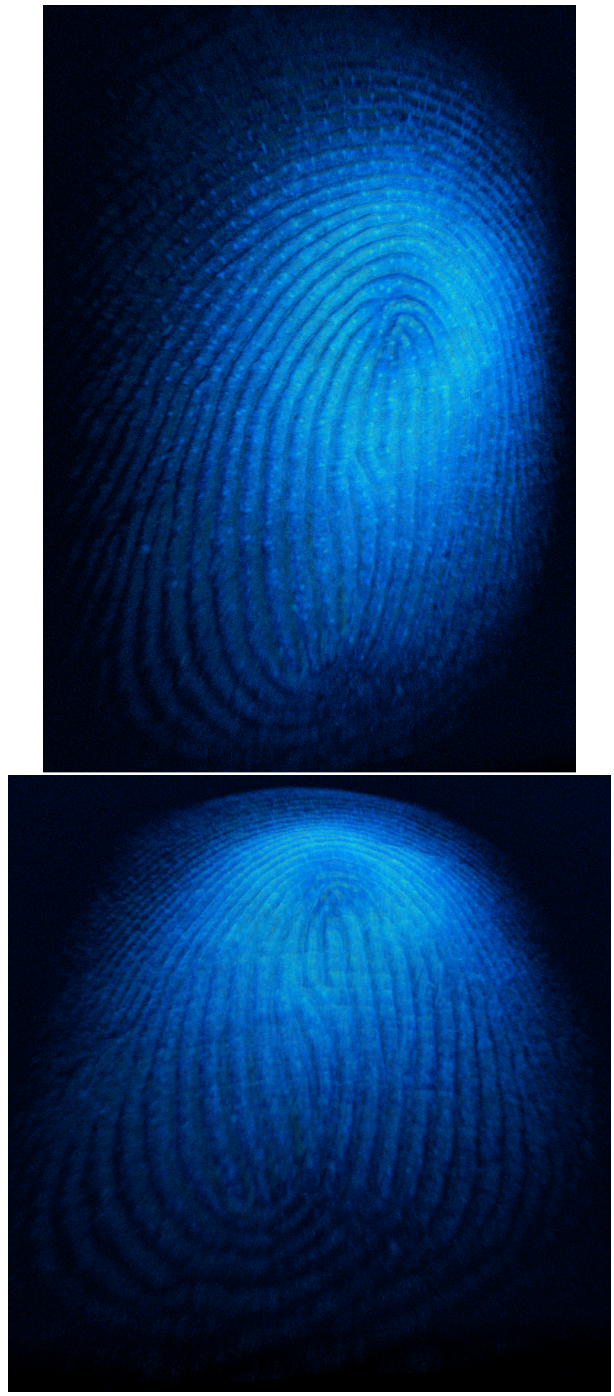

Figure 4.6: OCT scanner 2.0; index finger scan: 2x2cm area, 1408x1408x1024, 14.2μm - outer fingerprint - transparent 3D visualization

Figure 4.7: OCT scanner 2.0; thumb scan: 2x2cm area, 1408x1408x1024, 14.2μm - sweat glands overview - transparent 3D visualization

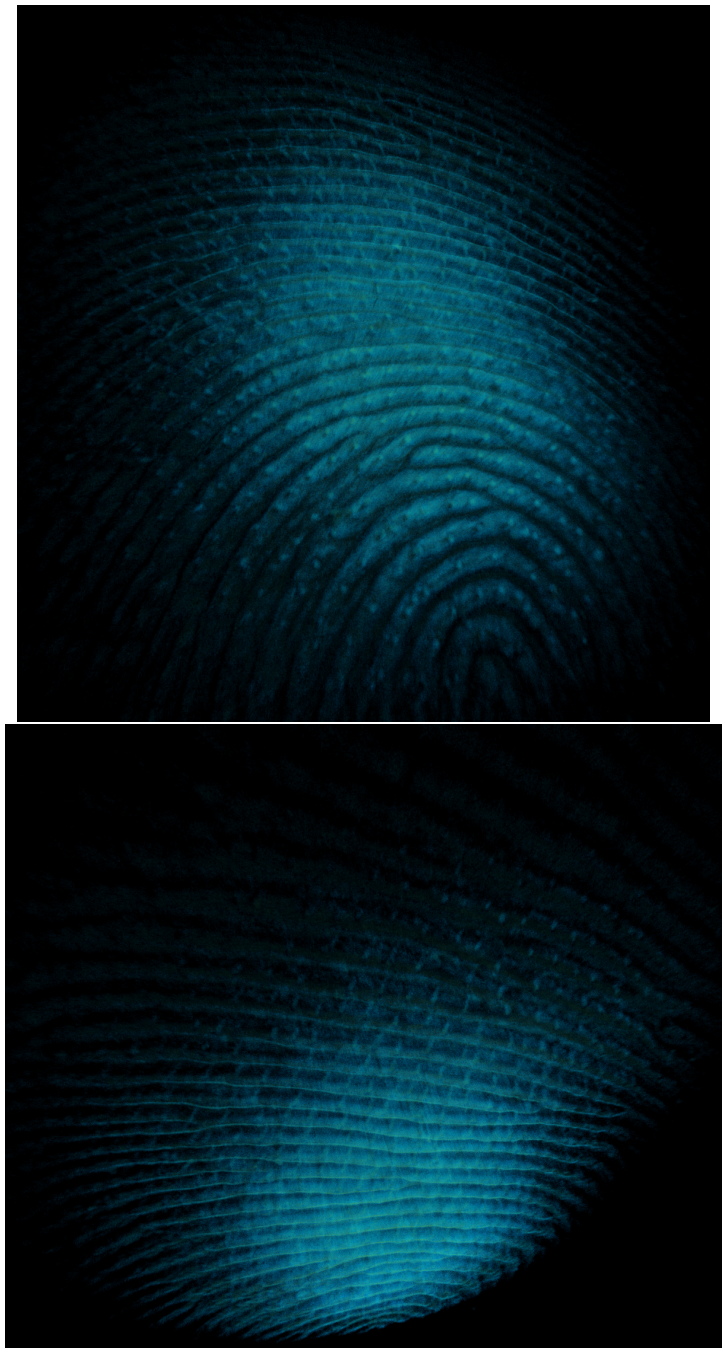

Figure 4.8: OCT scanner 2.0; thumb scan: 2x2cm area, 1408x1408x1024, 14.2μm - outer fingerprint - transparent 3D visualization

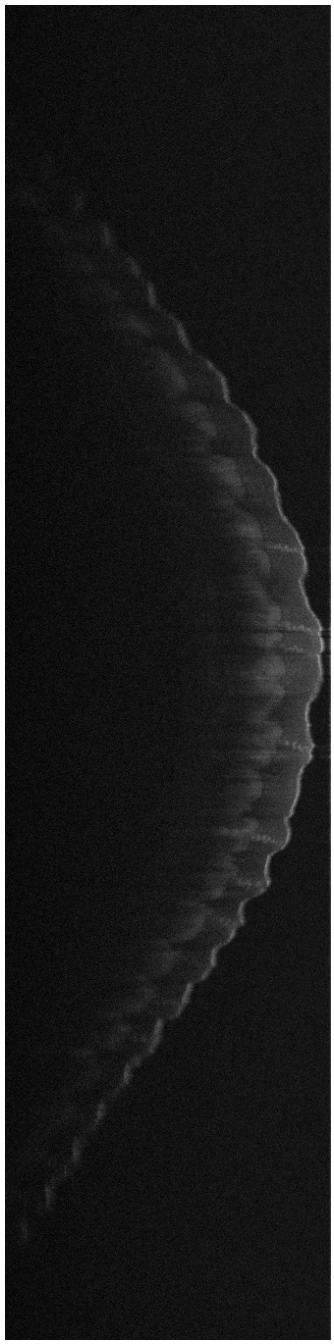

Figure 4.9: OCT scanner 2.0; thumb scan: (a) 2x2cm area, 1408x1408, 14.2μm, 5 averaged slices orthogonal to the finger axis

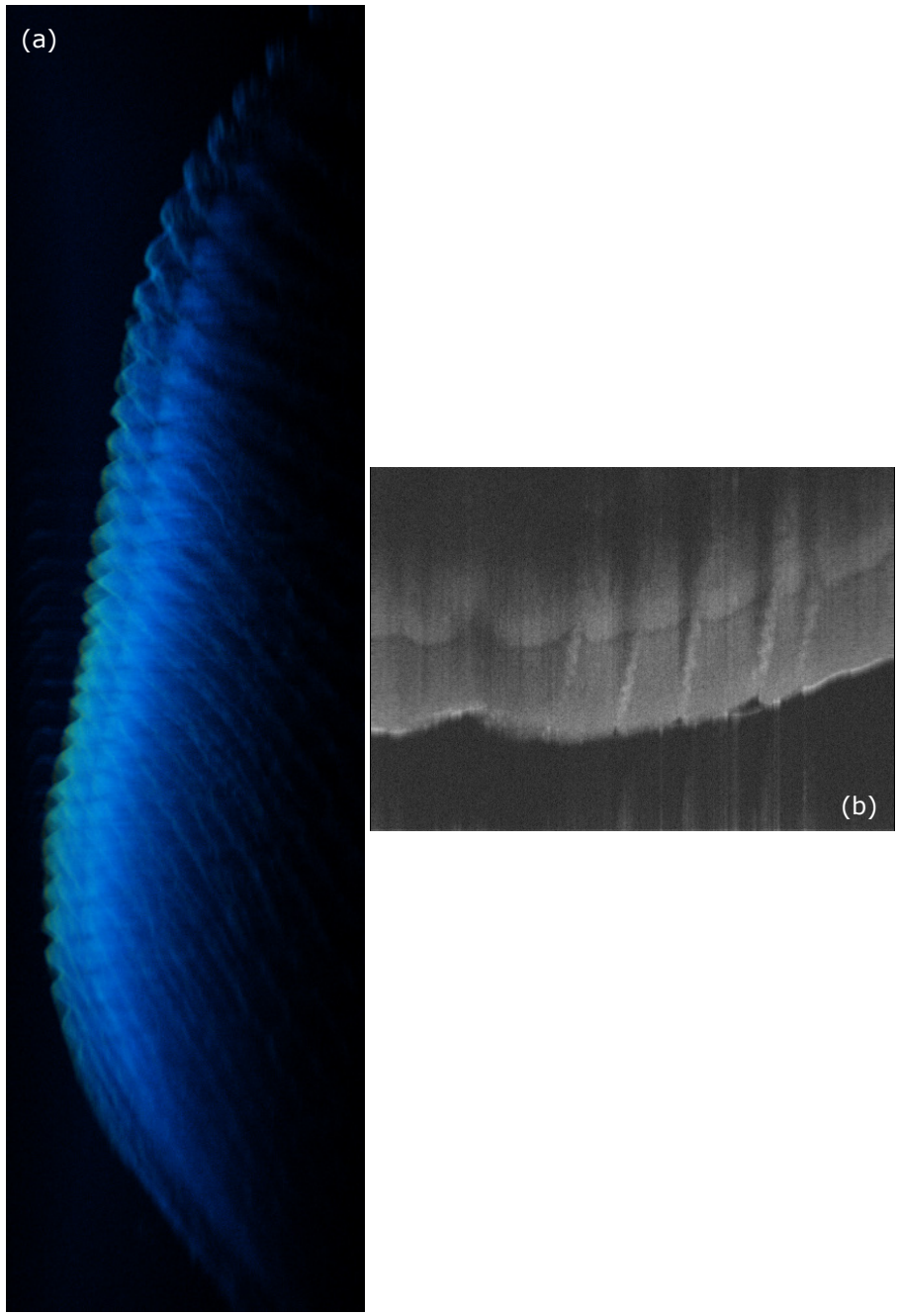

Figure 4.10: OCT scanner 2.0; thumb scan: (a) 2x2cm area, 1408x1408, 14.2μm transparent 3D visualization, finger visualized from the side; (b) 3.58x3.58 area, 512x512, 7μm, 10 averaged slices

4.5 Conclusion and Future Work

We have developed a novel specific-purpose FD-OCT fingerprint sensor setup. Unlike the existing designs, our setup is capable of imaging a full fingerprint from a 2x2 cm area, as a complete volumetric representation at speeds that demonstrate the usability of 3D OCT in real-world applications.

Our setup allows for software adjustments of the scanning area & resolution, which makes a 2-stage scanning pipeline possible - first stage being fingerprint extraction at lower resolutions and the second the high-resolution limited-area scanning for PAD purposes.

The future work would involve optimizations of the setup regarding the scanning range & resolution through the air as well as imaging depth into the fingertip skin, by an improved light management by means of non-evenly-splitting beam splitters and fiber couplers and related possible changes of the beam diameter.

The scanning head of the setup should be further improved to better address the issues associated with involuntary muscle shakes, that pose a challenge for high-quality imaging.

The future efforts will also focus on miniaturization, replacing the relatively large general-purpose electronics controlling the galvanometer and camera synchronization by a much smaller specialized solution. The scanning head could be significantly miniaturized using a MEMS mirror system replacing the large mirror galvanometer pair.

Chapter 5

Fast Edge & Blob Detection

5.1 Summary

This chapter describes two innovative techniques for performing low level filtering operations necessary for edges & blob detection in the OCT fingerprint data. The first proposed technique allows performing very efficient filtering by a smooth Gaussian and it's derivatives, with the intention to address the detection of blobs and soft edges in the noisy OCT data. The second approach allows for design of a range of high-performance filters suited somewhat better for detection of sharp edges. In terms of the second approach, a specific filter is proposed for efficient detection of the fingerprint layers along the in-depth scan-lines of the OCT scans. The work is planned for submission to EURASIP Journal on Advances in Signal Processing.

5.2 Motivation

Scanning using 3D high-resolution full-fingerprint OCT scanning generates very large amounts of volumetric data ($\simeq$ 1.9 GB of spatial data at 8-bit per voxel for a single finger in our dataset). A robust solution for processing such amounts of data in a matter of seconds, as required by the applications of fingerprint biometrics, poses a significant challenge. Many standard computer vision techniques and approaches are designed for processing of 2D images, while in our case, the processing requires fast handling of data containing an entire extra dimension.

Naive convolution-based filtering approaches are completely computationally prohibitive for high-resolution 3D data, since unlike 2D images where the computational complexity depends on $\mathcal{O}(width \times height \times filter\_size^2)$, the 3D data lead to a computational complexity depending on $\mathcal{O}(width \times height \times depth \times filter\_size^3)$. The extra factor of $depth \times filtersize$ can easily lead to increase in computational complexity by 3-5 orders of magnitude, especially for larger filter sizes and resolutions.

Consequently, robust processing of the OCT fingerprint data requires very efficient filtering techniques, ideally with a computational complexity independent of the filter size, such that not only the smallest and insufficient filter sizes are computationally feasible.

In addition, the 3D volumetric data ask for significant memory capacity, as they grow cubically with resolution, unlike the 2D images, where the growth is quadratic. The problem is not so much about storing the 3D OCT data (e.g as 8-bit voxels) in the memory, but rather about their processing where many standard 2D-image-suited approaches would generate a completely prohibitive amount of memory overhead during the processing.

A 3D OCT fingerprint processing approach that is robust, reliable and flexible enough for future improvements and adjustments calls for non-standard filtering techniques that exhibit excellent properties both in terms of computational and spatial complexity, such that the 3D data can be handled fast with reasonable amounts of memory.

5.3 Filter-size independent Gaussian filtering

Current industrial applications of computer vision for real-time video processing and real-time medical image analysis face similarly significant demands on computational performance, and several techniques and approaches have been invented that do satisfy the requirement that the performance of the filtering must be independent of the size of the filtering kernel, either in a more general setting or for specific, widely used filters.

One of the most widely used filters, well-known for its interesting properties in terms of noise reduction and the ability to process the image at a specific scale of interest is the Gaussian filter. The scale-specific suppression of the noise and of certain rather small and uninteresting features is strongly related to scale-specific edge & blob detection and serves in different forms as the groundwork for a large number of computer vision algorithms.

Automated analysis of the 3D OCT fingerprint data, in contrast to problems faced by generic 3D volumetric medical data segmentation, poses a problem of detecting the structure of outer and inner fingerprint layers along with sweat glands in between, which is somewhat simpler than problems such as generic organ segmentation or 3D volumetric vein segmentation. However, the amounts of data are potentially even larger than for a full-body CT (due to the necessary microscopic resolutions) and the requirements on reliability, speed and fully automatic operation pose a significant additional challenge.

As such, filtering techniques are needed that can perform rather generic but robust and noise-resilient edge & blob detection for a 3D volume with excellent computational as well as spatial complexities.

The Gaussian filter is a core component of a number of such generic edge & blob detection approaches, such as Laplacian of Gaussian (LoG) and its commonly used approximation, Difference of Gaussians (DoG).

A significant advantage of the Gaussian-filtering-based edge & blob detection techniques for processing 3D OCT fingerprint data is the separability of the Gaussian core. It is possible to calculate a convolution of n-dimensional data and n-dimensional Gaussian core by n separate computing passes along

each of the n dimensions, reducing the computational complexity vastly from $\mathcal{O}(d^n)$ to $\mathcal{O}(dn)$ (introducing, however, spatial complexity issues).

A number of approaches exist to compute a Gaussian filtered version of a signal in 1D, apart from the computationally expensive basic convolution [42]. A widely-known approach is the filtering in the frequency domain, for which the signal is transformed by Fast Fourier Transform (FFT) or Fast Cosine Transform (FCT) ($\mathcal{O}(n \log n)$), the filter is applied by multiplication of two signals ($\mathcal{O}(n)$), and the result is transformed back into the spatial domain by inverse FFT/FCT ($\mathcal{O}(n \log n)$). The computational expense of computing FFT/FCT twice has motivated a number of other approaches that aim to further minimize the computational cost. A Gaussian filtered signal can be efficiently approximated by K repeated filtering passes by box filters [45, 110] thanks to the possibility of performing 1D box filtering in $\mathcal{O}(n)$ by sequential subtraction/addition (running sums) or by employing integral images [8, 35, 47, 49].

Another group of techniques for the Gaussian filtering is based on an application of recursive filtering techniques [31], requiring causal and anti-causal filter pairs. The approach by Deriche [32] requires parallel computation of the response of the causal and anti-causal filters and combination of the results, while the approaches by Young and Vliet [114] and Vliet et al. [109] require the causal and anti-causal filters to be applied in a cascade.

As the 1D LoG filter is the result of a second-order Gaussian filter derivative of the corresponding size, it is possible to perform the LoG filtering by Gaussian filtering followed by the computation of the second-order signal derivative by using neighboring sample differences [109]. An approximation of a LoG filtered image can also be obtained by Gaussian filtering with a core of variance σ, followed by a LoG filtering by a smaller and potentially less expensive core ($\sigma_2 < \sigma$) [17] (DoG).

However, all of these standard approaches require an additional memory buffer of signal length or in-situ overwriting of the original signal before the results can be obtained:

- frequency domain 1D LoG or Gaussian filtering - due to the necessity to calculate the frequency domain representation
- recursive 1D LoG and Gaussian filtering - due to application of the causal and anti-causal filter pairs
- Application of the integral signal - the integral signal has to be precomputed and stored
- The multi-pass running-sum based approach - the pass $k + 1$ requires results from pass k

5.4 Read-only filter-size-independent Gaussian filtering

The requirement for additional signal-length buffers of the above mentioned filter-size-independent methods for Gaussian filtering strongly limits their usability when processing 3D volumetric data under strong memory constraints.

Especially in a massively parallel computing environment, such as GPUs, the need for additional buffer of the size of the processed signal adds a significant extra memory requirement. The problem is even more severe when using the above mentioned fast Gaussian filtering methods to accomplish 3-D Gaussian filtering by 3 separate parallel Gaussian filtering passes.

The following proposed Gaussian filtering approximation technique has no need for additional intermediary memory buffers, and can deliver the Gaussian filtered results readily on-the-fly, allowing for nearly the same flexibility in filtering design as the basic convolution.

5.4.1 Laplacian of Gaussian approximation

We approximate the Laplacian of Gaussian by adding two overlapping sinusoidal waves (Fig. 5.1a):

$$aLoG_1(x) = \begin{cases} -sin(x) & \text{if } x \in (0, 2\pi) \\ 0 & \text{else} \end{cases} \tag{5.1}$$

$$aLoG_2(x) = \begin{cases} -sin(x) & \text{if } x \in (\pi, 3\pi) \\ 0 & \text{else} \end{cases} \tag{5.2}$$

$$aLoG(x) = aLoG_1(x) + aLoG_2(x) \tag{5.3}$$

5.4.2 Filtering in discrete domain

In the discrete domain ($x \in \mathbb{Z}$), the filtering cores, $aLoG_1$ and $aLoG_2$, can be defined as follows:

$$aLoG_1(x) = \begin{cases} -sin(\frac{3\pi}{s_f}x) & \text{if } x \in (0, \frac{2}{3}s_f - 1) \\ 0 & \text{else} \end{cases} \tag{5.4}$$

$$aLoG_2(x) = \begin{cases} -sin(\frac{3\pi}{s_f}x) & \text{if } x \in (\frac{1}{3}s_f, s_f) \\ 0 & \text{else} \end{cases} \tag{5.5}$$

The convolution $*$ of the signal, $s(x)$, and the filtering cores, $aLoG_1$ and $aLoG_2$, can be expressed using the imaginary component of complex exponential functions as follows:

$$(s * aLoG_1)(x) = \Im(\sum_{n=0}^{2/3s_f-1} -e^{i\frac{3\pi}{s_f}n} s(x+n)) \tag{5.6}$$

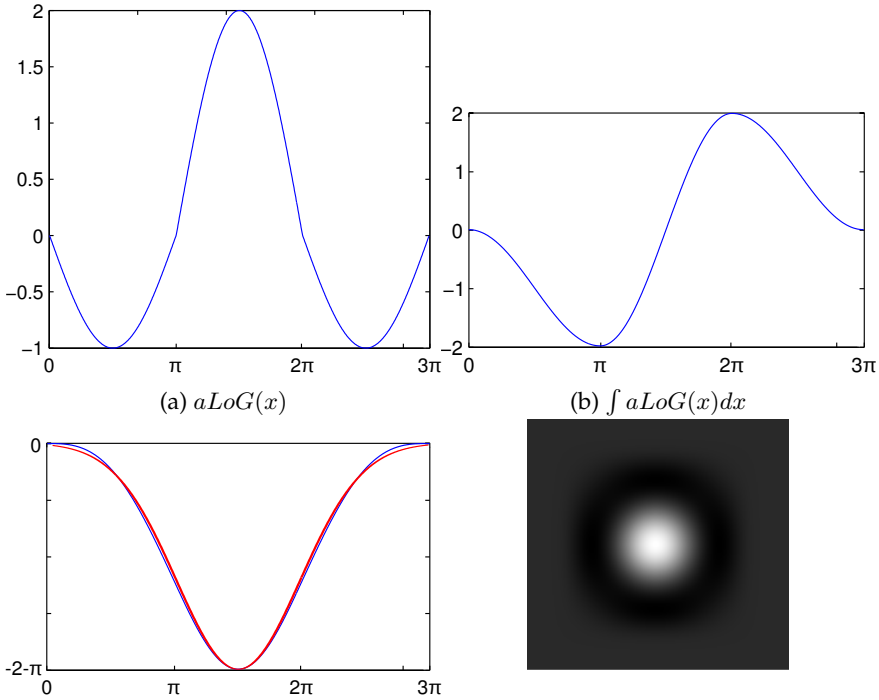

(a) $aLoG(x)$

(b) $\int aLoG(x)dx$

(c) blue: $\int\int aLoG(x)dx$, red: real Gaussian

(d) 2D DoG impulse response generated using our approximate Gaussian

Figure 5.1: Approximated Gaussian and its derivatives

$$(s * aLoG_2)(x) = \Im(\sum_{n=0}^{2/3s_f-1} e^{i\frac{3\pi}{s_f}n} s(x + \frac{1}{3}s_f + n)) \tag{5.7}$$

Let $z_1(b)$ be an intermediary result defined at $z_1(0)$ as equivalent to the complex version of the convolution $(s * aLoG_1)(0)$.

$$z_1(0) = \sum_{n=0}^{2/3s_f-1} -e^{i\frac{3\pi}{s_f}n} s(n) \tag{5.8}$$

$$\Im(z_1(0)) = (s * aLoG_1)(0) \tag{5.9}$$

$z_1(b)$ can be recursively defined as follows, requiring only two samples of signal, $s(x)$, upon every step:

$$\begin{aligned} z_1(b) = \sum_{n=b}^{2/3s_f-1+b} -e^{i(\frac{3\pi}{s_f}n)} s(n) = z_1(b-1) - \\ - (-e^{i(\frac{3\pi}{s_f}(b-1))}) s(b-1) + (-e^{i(2\pi+\frac{3\pi}{s_f}(b-1))}) s(\frac{2}{3}s_f - 1 + b) \end{aligned} \tag{5.10}$$

By performing a simple phase shift of the intermediary result, $z_1(b)$, it is possible to compute the complex version of the term $(s * aLoG_1)(b)$. This allows to calculate the convolution of the signal, $s(x)$, with the core, $aLoG_1(x)$, in a very efficient manner.

$$\begin{aligned} z_1(b)e^{i(-\frac{3\pi}{s_f}b)} = \sum_{n=b}^{2/3s_f-1+b} -e^{i(\frac{3\pi}{s_f}n)} e^{i(-\frac{3\pi}{s_f}b)} s(n) = \\ = \sum_{n=b}^{2/3s_f-1+b} -e^{i(\frac{3\pi}{s_f}(n-b))} s(n) = \sum_{n=0}^{2/3s_f-1} -e^{i(\frac{3\pi}{s_f}n)} s(b+n) \end{aligned} \tag{5.11}$$

$$\Im(z_1(b)e^{i(-\frac{3\pi}{s_f}b)}) = (s * aLoG_1)(b) \tag{5.12}$$

A similar definition is possible for the other core, $aLoG_2(x)$. Let $z_2(b)$ be an intermediary result defined at $z_2(0)$ as equivalent to the complex version of the convolution $(s * aLoG_2)(0)$.

$$z_2(0) = \sum_{n=0}^{2/3s_f-1} e^{i\frac{3\pi}{s_f}n} s(\frac{1}{3}s_f + n) \tag{5.13}$$

$$\Im(z_2(0)) = (s * aLoG_2)(0) \tag{5.14}$$

$z_2(b)$ can be recursively defined as follows, requiring only two samples of signal, $s(x)$, upon every step:

$$z_2(b) = \sum_{n=b}^{2/3s_f-1+b} e^{i(\frac{3\pi}{s_f}n)} s(\frac{1}{3}s_f + n) = z_2(b-1) -$$
$$- (e^{i(\frac{3\pi}{s_f}(b-1))}) s(\frac{1}{3}s_f + b - 1) + (e^{i(2\pi+\frac{3\pi}{s_f}(b-1))}) s(\frac{1}{3}s_f + \frac{2}{3}s_f - 1 + b) \quad (5.15)$$

By performing a simple phase shift of the intermediary result, $z_2(b)$, it is possible to compute the complex version of the term $(s * aLoG_2)(b)$. This allows to calculate the convolution of the signal, $s(x)$, with the core, $aLoG_2(x)$, in a very efficient manner.

$$z_2(b)e^{i(-\frac{3\pi}{s_f}b)} = \sum_{n=b}^{2/3s_f-1+b} e^{i(\frac{3\pi}{s_f}n)} e^{i(-\frac{3\pi}{s_f}b)} s(\frac{1}{3}s_f + n) =$$
$$= \sum_{n=b}^{2/3s_f-1+b} e^{i(\frac{3\pi}{s_f}(n-b))} s(\frac{1}{3}s_f + n) = \sum_{n=0}^{2/3s_f-1} e^{i(\frac{3\pi}{s_f}n)} s(b + \frac{1}{3}s_f + n) \quad (5.16)$$

$$\Im(z_2(b)e^{i(-\frac{3\pi}{s_f}b)}) = (s * aLoG_2)(b) \quad (5.17)$$

Considering the main convolution, $(s * aLoG)(x)$, with the core, $aLoG(x) = aLoG_1(x) + aLoG_2(x)$, it is possible to define a joint intermediary result:

$$z(b) = z_1(b) + z_2(b) \quad (5.18)$$

The joint intermediary result, z, can be recursively updated by a phase-shifted sum of signal reads as follows:

$$z(b) = z(b-1) - (-e^{i(\frac{3\pi}{s_f}(b-1))}) s(b-1) + (-e^{i(2\pi+\frac{3\pi}{s_f}(b-1))}) s(\frac{2}{3}s_f - 1 + b) -$$
$$- (e^{i(\frac{3\pi}{s_f}(b-1))}) s(\frac{1}{3}s_f + b - 1) + (e^{i(2\pi+\frac{3\pi}{s_f}(b-1))}) s(\frac{1}{3}s_f + \frac{2}{3}s_f - 1 + b) =$$
$$= z(b-1) -$$
$$- e^{i(\frac{3\pi}{s_f}(b-1))}(-s(b-1) + s(\frac{1}{3}s_f + b - 1) + s(\frac{2}{3}s_f + b - 1) - s(s_f + b - 1)) \quad (5.19)$$

The final result of the main convolution, $(s * aLoG)(b)$, with the core, $aLoG(x) = aLoG_1(x) + aLoG_2(x)$, can be obtained by a simple phase shifting of the joint intermediary result, z:

$$\begin{aligned}(s * aLoG)(b) &= (s * aLoG_1)(b) + (s * aLoG_2)(b) = \\ &= \Im(z_1(b)e^{i(-\frac{3\pi}{s_f}b)} + z_2(b)e^{i(-\frac{3\pi}{s_f}b)}) = \\ &= \Im(e^{i(-\frac{3\pi}{s_f}b)}z) \end{aligned} \tag{5.20}$$

Eq. 5.19 and 5.20 provide a framework for computing a result that is equivalent to 1D convolution with the proposed LoG approximation. The intermediary result, $z(x)$, can be re-used to calculate an intermediary result, $z(x+1)$, and the final filtering result can be obtained by a simple phase shift. Apart from an initialization step, the computational complexity is independent of the filter size, and does not require an intermediary memory buffer.

5.4.3 Gaussian-like filtering

A convolution with a Gaussian core $G(x) = \int\int g(x)dxdx$ can be seen as a convolution with its second derivative, Laplacian of Gaussian, $g(x)$, followed by integrating twice as follows:

$$\int_{-\infty}^{\infty} f(\tau) \int\int g(t-\tau)dtdtd\tau = \int\int\int_{-\infty}^{\infty} f(\tau)g(t-\tau)d\tau dtdt \tag{5.21}$$

This is equivalent to convolution with the Gaussian-like core illustrated by Fig. 5.1c.

For practical implementation of the above analyzed approach to computation of a LoG approximation, 2 independent accumulators are required, in order to hold the real and imaginary part of the intermediary result, z (Eq. 5.19).

The following functions, $fcos(n)$ and $fsin(n)$, can be pre-computed and used in a cyclical fashion ($n \in (0, s_f - 1)$):

$$fcos(n) = \Re(e^{i(\frac{3\pi}{s_f}n)}) = cos(\frac{3\pi}{s_f}n), \qquad fsin(n) = \Im(e^{i(\frac{3\pi}{s_f}n)}) = sin(\frac{3\pi}{s_f}n) \tag{5.22}$$

The accumulators $Acc_1, Acc_2(Int_0, Int_1)$ can be initialized simply using zeros, which is their proper value for a zero signal, following by a filtering as if the signal was padded by s_f zeros. Since some of the signal reads performed during this initial phase are zero by definition, the algorithm can be simplified accordingly for the initialization phase, yielding 2 actual signal reads per pixel.

For every step from $(s * aLoG)(x)$ to $(s * aLoG)(x+1)$, 4 signal reads are necessary to obtain the values necessary further on.

Algorithm 5.1: Signal reads

$s_0 \leftarrow s(x)$;
$s_1 \leftarrow s(x + \frac{1}{3}s_f)$;
$s_2 \leftarrow s(x + \frac{2}{3}s_f)$;
$s_3 \leftarrow s(x + s_f)$;

The accumulators are updated as follows:

Algorithm 5.2: Accumulator update

$v_c \leftarrow -fcos(x)$;
$v_s \leftarrow -fsin(x)$;
$s_a \leftarrow -s_0 + s_1 + s_2 - s_3$;
$Acc_1 \leftarrow Acc_1 + v_c s_a$;
$Acc_2 \leftarrow Acc_2 + v_s s_a$;

Since only the imaginary part of the result is needed, the phase shift from Eq. 5.20 can be implemented as follows, prividing the final filtering result with the proposed approximate 1D Laplacian of Gaussian $aLoG$:

Algorithm 5.3: Phase shift

$aLoG = Acc_1 v_s - Acc_2 v_c$;

Convolution with the Gaussian-like core illustrated by Fig. 5.1c can be achieved by two integration accumulators:

Algorithm 5.4: Gaussian-like filtering

$Int_0 = Int_0 + aLoG$;
$Int_1 = Int_1 + Int_0$;
$aGauss = Int_1$;

5.4.4 Performance

In order to provide for a fair performance benchmark of our approach, we adopted the following protocol. We processed 1GB of 1024x1024x1024 8-bit voxels with our method 10x along one dimension, averaging the computation time. The methods that have been benchmarked, apart from our proposed method, are recursive filtering [114], 4-pass averaging filtering [35] and symmetrically implemented convolution.

For the CPU demonstration, a single-thread non-parallel C++ implementation was used, executed on 64-bit Intel(R) Core(TM) i7-3820 CPU @ 3.60GHz, in order to illustrate the relative performance in sequential processing[1] - Fig.

[1]It is worth noting that acceleration by using vector instructions and multiple threads would

5.2a. The CPU calculations are performed in 64-bit floating point or 64-bit integer as necessary.

The GPU demonstration is done using CUDA implementation on NVidia GeForce GTX 660 Ti and GTX 980 SC - Fig. 5.2b. The GPU computation is performed in 32-bit floating point, native to the employed GPUs.

5.4.5 Discussion

Our approach allows for scan-line filtering by a smooth approximation of Laplacian of Gaussian with 2 accumulators, 4 reads, 4 multiplications and 6 additions. With 2 extra additions and 2 extra accumulators, smooth approximate Gaussian filtering is possible. Our method operates in a read-only fashion without any intermediate signal representations yielding the filtered results in a single pass.

In our experiments, both in the GPU and the CPU setting, our approach outperforms state-of-the-art alternative approaches for Gaussian-like filtering with computational complexity independent of the filter size. In the CPU setting, the approach was speed-wise equivalent to a 12-pixel symmetrically implemented convolution and in the GPU setting to a 5-6 pixel convolution. The commonly-employed running sums approach ranks second best on the CPU, while performing poorly on the GPU. This is probably due to the slow global memory access compared to the speed of computation and a small cache, which properties are characteristic for GPUs. We hypothesize that the slight variations in computational complexity with the filter size for some of the methods are caused by interference of the differences in memory access pattern for different filter sizes.

5.5 Fast scan-line edge detection

Detection of the outer and inner fingerprint surfaces from the 3D volumetric data can be seen as a problem of detecting major edges along the in-depth scan-lines in the OCT scan - Fig. 5.3.

Taking into account the size of the volumetric 3D OCT data and the significant amounts of noise typical for OCT scanning, usage of a fast edge detector, capable of considering a wide neighborhood of the edge candidates, is probably advisable so that reliable detection of the inner and outer fingerprint surfaces can be achieved.

5.5.1 Differential filter design

A closer examination of the previously mentioned eq. 5.21 offers interesting options for creating a custom-designed fast edge detection filter. Eq. 5.21 can be generalized as follows:

probably lead to a speed-up by an order of magnitude, however, we wanted to demonstrate the relative performance in a non-parallel setting

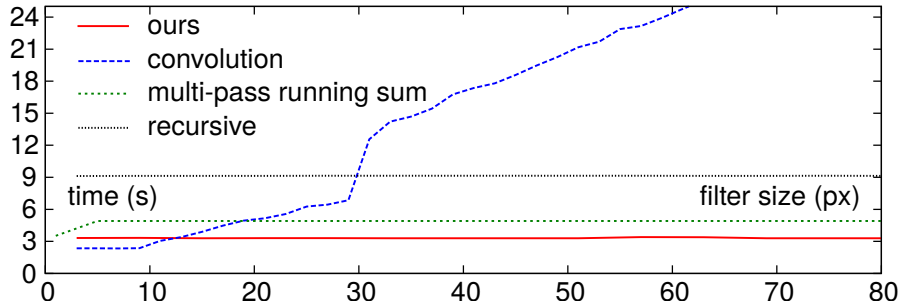

(a) processing 1GB (1024x1024x1024) 8-bit voxels along one dimension in a single-thread on Intel(R) Core(TM) i7-3820 CPU @ 3.60GHz

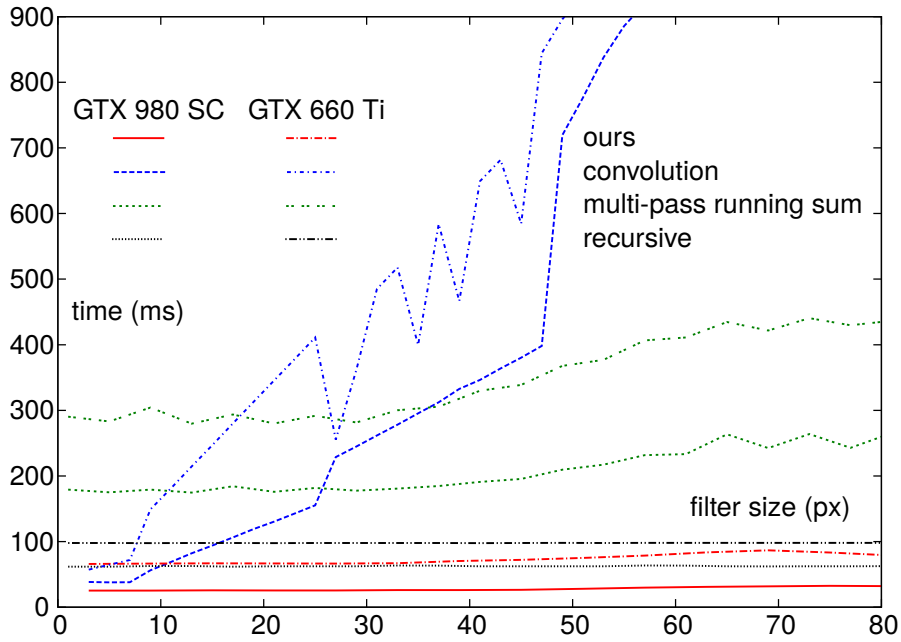

(b) processing 1GB (1024x1024x1024) 8-bit voxels along one dimension on GTX 980 and GTX 660 GPUs

Figure 5.2: Fast Gaussian filtering performance benchmark

$$\int_{-\infty}^{\infty} f(\tau) \int \cdots \int g(t-\tau)dt \cdots dtd\tau = \int \cdots \int \int_{-\infty}^{\infty} f(\tau)g(t-\tau)d\tau dt \cdots dt \tag{5.23}$$

Intuitively, it is possible to calculate n-th derivative, g, of the convolution

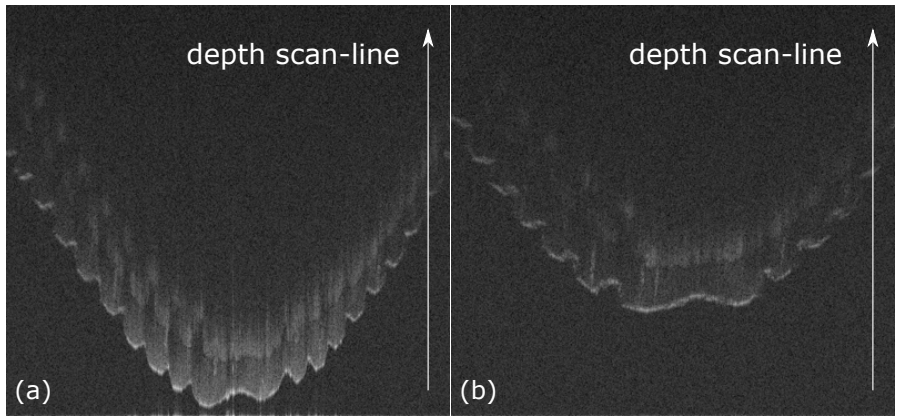

Figure 5.3: OCT finger 2D slices - inner and outer fingerprint edges visualization

core, $G = \int \cdots \int g$, perform the convolution with the source signal and integrate n-times, in order to obtain a result equivalent to convolution with the core, G.

The idea is that it could be possible to design a relatively complex and wide filter, which would normally lead to excessive computational demands, but with a sparse and simple representation of the n-th derivative, which allows for performing of the convolution much more efficiently.

5.5.2 OCT-specific scan-line edge detection filter

The design of a filter suitable for scan-line edge detection in the OCT fingerprint data, as depicted by Fig.5.3, should meet several criteria for maximum robustness and computational efficiency:

- zero response for a continuous signal with no slope - total integral of the filter equals zero - this ensures that the filter measures the strength of the edge only, ignoring other not-edge-related effects such as overall slope or strength of the signal
- The edges for both the outer and inner fingerprint are always positive (Fig. 5.3) - For the outer fingerprint, the signal changes from the dark reflection of the empty air to the strong reflection of the fingerprint tissue; For the inner fingerprint, the reflection changes from a weaker reflection of the middle layer to a stronger reflection of the inner layer - This suggests the filter shape should be suited for detecting positive edges only
- The filter should be capable of precise localization of strong thin edges (Fig. 5.3b), as well as wider edge boundaries (Fig. 5.3a). This suggests

a filter with a slope in the positive and the negative half, which design will ensure maximum response at the correct position when detecting strong thin edges

- The slopes of the filter should copy the diminishing reflections of the boundaries with the depth (Fig. 5.3a)
- 1st, 2nd or 3rd derivation should lead to a very sparse representation of the filter (further derivation quickly leads to precision issues), which would allow for efficient convolution with the scan-lines of the OCT data

Bearing in mind the above mentioned criteria, we propose the following approximate filter suited for detection of positive edges at the fingerprint layer boundaries in the OCT data (Fig. 5.4):

$$G(n) = \begin{cases} -height_2 + (n+1) \cdot slope & \text{if } n \in [-\frac{size}{2}, -1] \\ height_2 - n \cdot slope & \text{if } n \in [0, \frac{size}{2} - 1] \\ 0 & \text{otherwise} \end{cases} \tag{5.24}$$

The parameters $size$, $height_1$ and $height_2$ can be chosen freely and the $slope$ parameter is defined as:

$$slope = \frac{height_2 - height_1}{size/2 - 1} \tag{5.25}$$

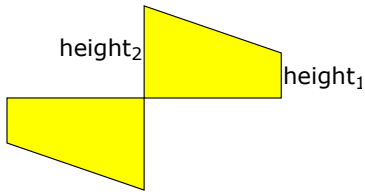

Figure 5.4: Shape of the proposed approximate positive edge detection filter

The first derivative of the filtering core, G', is defined as follows (Fig. 5.5b):

$$G'(n) = \begin{cases} -height_1 & \text{if } n = -\frac{size}{2} \\ -slope & \text{if } n \in [-\frac{size}{2} + 1, -1] \\ 2 \cdot height_2 & \text{if } n = 0 \\ -slope & \text{if } n \in [1, \frac{size}{2} - 1] \\ -height_1 & \text{if } n = \frac{size}{2} \\ 0 & \text{otherwise} \end{cases} \tag{5.26}$$

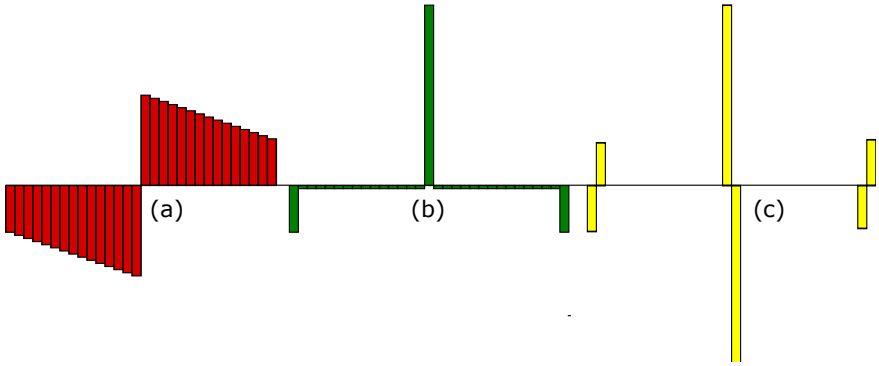

Figure 5.5: Fast approximate edge detection filter and its derivatives for $height_1 = 15$, $height_2 = 29$, $size = 30$: (a) filter core $G(x)$; (b) first derivative $G'(x)$; (c) second derivative $G''(x)$

Finally, the second derivative of G leads to a following sparse representation (Fig. 5.5c):

$$G''(n) = \begin{cases} -height_1 & \text{if } n = -\frac{size}{2} \\ height_1 - slope & \text{if } n = -\frac{size}{2} + 1 \\ 2 \cdot height_2 + slope & \text{if } n = 0 \\ -(2 \cdot height_2 + slope) & \text{if } n = 1 \\ -height_1 + slope & \text{if } n = \frac{size}{2} \\ height_1 & \text{if } n = \frac{size}{2} + 1 \\ 0 & \text{otherwise} \end{cases} \tag{5.27}$$

Independently of the filter size, $size$, and the shape parameters, $height_1$ and $height_2$, the second derivative G'' is always represented using 6 non-zero filter weights only. In addition, every two non-zero weights are adjacent at a position n and $n + 1$, which allows for a filter implementation where only 3 actual signal reads per pixel are necessary, and the other 3 signal reads are performed using 3 extra variables serving as delay lines, reusing the signal reads from the computation of a previous pixel.

If one considers a zero-padded version of the signal, the accumulators and delay lines can be initialized simply using zeros:

Algorithm 5.5: Edge detection filter - initialization

1 $s_0 = 0$;
2 $s_2 = 0$;
3 $s_4 = 0$;
4 $Acc_0 = 0$;
5 $Acc_1 = 0$;
6 $c_0 = height_1$;
7 $c_1 = height_1 - slope$;
8 $c_2 = 2 \cdot height_1 + slope$;

A step of the filtering is performed as:

Algorithm 5.6: Edge detection filter - a filtering step

1 $s_1 = s(x - size/2 + 1)$;
2 $s_3 = s(x + 1)$;
3 $s_5 = s(x + size/2 + 1)$;
4 $Acc_0 = Acc_0 - c_0 s_0 + c_1 s_1 + c_2 s_2 - c_2 s_3 - c_1 s_4 + c_0 s_5$;
5 $Acc_1 = Acc_1 + Acc_0$;
6 $s_0 = s_1$;
7 $s_2 = s_3$;
8 $s_4 = s_5$;
9 $result = Acc_1$

5.6 Conclusion

A framework has been presented that enables designing of fast, filter-size independent implementations of some of the essential filters necessary for edge & blob detection in the context of processing of OCT fingerprint scans. Solutions have been demonstrated for fast approximate filtering by a Gaussian core, its first derivative and the LoG core. The presented Gaussian filtering solution also supports separable filtering, which allows for usage of the algorithm as a building block in calculating Difference of Gaussians (DoG). In addition, an alternative approach has been suggested that allows implementations of fast custom filtering. In particular, a specific design of a parametrizable filter for detection of positive edges in the scan-lines of the OCT data has been described in detail.

Chapter 6

Fingerprint Extraction

6.1 Summary

This chapter is based on the paper by Sousedik & Breithaupt [100]. Utilizing the data collected using our sensor (see Chapter 4) and our fast edge detection filtering approach (see Chapter 5), we developed a technique for extraction of the outer and inner fingerprints from the OCT scan. Our GPU-accelerated technique can extract both fingerprints from a 2GB OCT scan in less than 1.25 seconds. The OCT-extracted fingerprints have been evaluated by comparisons to fingerprints captured by a standard 2D sensor. Our results show that the sub-surface inner fingerprints extracted from underneath the fingertip skin perform better than the fingerprints extracted from the surface, which shows great promise of the OCT for the fingerprint sensing scenario. At the same time, despite the potential of the OCT fingerprint sensor for improvements, the subsurface inner fingerprints do perform at near-practical error rates already.

6.2 Related Work

Despite the fact that a number of initial studies exists regarding the application of the OCT for fingerprint sensing and genuine/fake finger detection (see Chapter 2, Section 2.5.2, OCT), very few studies take the speed of the processing into account. OCT fingerprint scans represent volumetric data of very significant sizes if one aims for standard resolutions of 500dpi or 1000dpi in 2D, which easily exceeds 1 GB per finger (1024x1024x1024 at 8bit). This fact calls for an approach where the speed of the processing techniques is taken seriously into account as an actual research challenge, rather than disregarded as simply a matter of faster processing hardware.

In addition, majority of the studies assume a finger pressed against a flat surface (e.g. glass) during the scanning, which greatly simplifies the processing challenges (since the fingerprint surface is flattened) but introduces a number of disadvantages shared with standard 2D fingerprint sensors, such as difficulty to scan wet, greasy, dry or soft-skinned fingers, which could otherwise be easily overcome by the OCT [28, 74].

Last but not least, the free-air scanning approach taken in our work has the potential for touch-less fingerprint sensing applications, where the subjects

do not have to come into contact with any potentially unclean surface of the fingerprint sensor, increasing acceptability and convenience.

Regarding the work that satisfies the challenging constraints mentioned above, we are aware only of the promising works by Darlow et al. [26, 27, 28].

6.3 Fingerprint Surface Extraction in 3D

Our approach is to scan the fingerprint free-air, such that it is undistorted by pressing against a flat surface (such as glass). This comes with the challenge of precise 3D segmentation of the volumetric fingerprint OCT scan, so that further analysis is possible. A well segmented OCT fingerprint scan could be further used for extracting the fingerprints both from the surface and from underneath the skin and it could also serve well for further analysis of the skin regarding PAD (Fig. 6.3).

6.3.1 Database

We utilized the OCT fingerprint scan dataset collected with our OCT fingerprint sensor: [99] (see Chapter 4, Section 4.4.2):

- 1408x1408x1024 voxels
- 8bit per voxel
- 72 participants
- all 10 fingers
- 720 OCT fingerprint scans in total
- 2x2cm scanning area

Along with the OCT fingerprints, the dataset also contains standard 2D fingerprints collected from an identical set of participants, in order to enable testing of compatibility of the OCT fingerprints and the standard 2D fingerprints. This dataset contains 520 2D fingerprints, of all 10 fingers from 52 participants.

6.3.2 Efficient edge detection

In order to address the challenge of processing 2GB OCT fingerprint scans in a matter of a few seconds, as required by numerous applications including border control, we took a combined approach of cuda GPU acceleration and our specifically developed fast filter-size-independent filtering technique, discussed in detail in Chapter 5, Section 5.5.2. Our technique allows to perform the convolution with the core illustrated by Fig. 6.1a, by computing a convolution with the core's second derivative - Fig. 6.1c - and double integration on the fly.

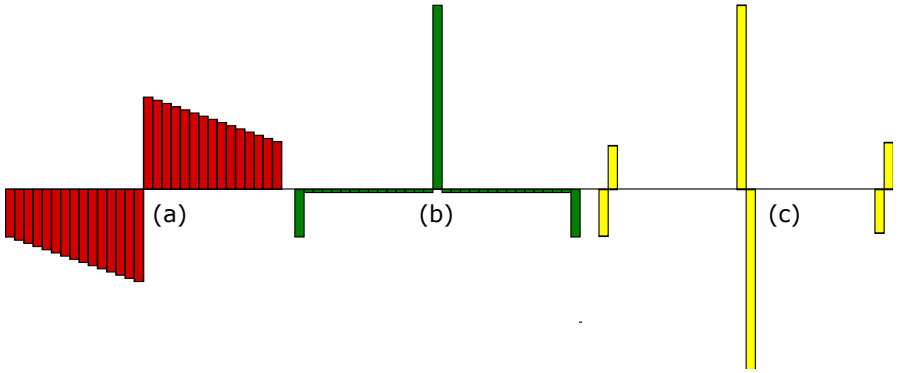

Figure 6.1: Our fast approximate edge detection filter and its derivatives (a) filter core $G(x)$; (b) first derivative $G'(x)$; (c) second derivative $G''(x)$

Notably, the core illustrated by Fig. 6.1c has always only 6 non-zero coefficients, which come in 3 pairs of 2 coefficients positioned immediately next to each other - Fig. 5.5. This allows for a very efficient implementation of the convolution on the GPU, since only 3 memory reads per voxel are necessary to perform the filtering along the scan-lines, as the other 3 reads can be implemented using 3 delay variables reusing the results from a previous voxel. Integrating the results twice along the way allows to obtain the convolution of the scan-lines with the core, $G(n)$, in very efficient manner in a single cuda GPU thread per scan-line. In addition, the technique can calculate the results for each of the scan-lines without using any extra intermediary memory buffer, which supports both the speed and the flexibility of the approach.

The actual edge detection is performed by identifying the position of a maximum during the process of convolution of the OCT scan-lines and the above discussed convolution core.

6.3.3 Outer Fingerprint Surface

However, it is highly sub-optimal to simply perform the above discussed edge detection for each of the (x, y) in-depth scan lines and treat the result as the detected surface. The OCT scan inherently contains large amounts of noise, and such an approach would result in a highly noisy surface (point-cloud), full of holes, where the detection failed due to the presence of the noise - Fig. 6.2a.

In addition, the strength of the finger's response diminishes with depth, which poses further challenges - Fig. 6.3.

In order to address the challenges, we took inspiration from the approach by Darlow et al. [27], where the fingerprint surface detection is performed using a pyramid of down-sampled versions of the original 3D OCT fingerprint data. Unlike Darlow et al. [27], who suggest building the pyramid by down-

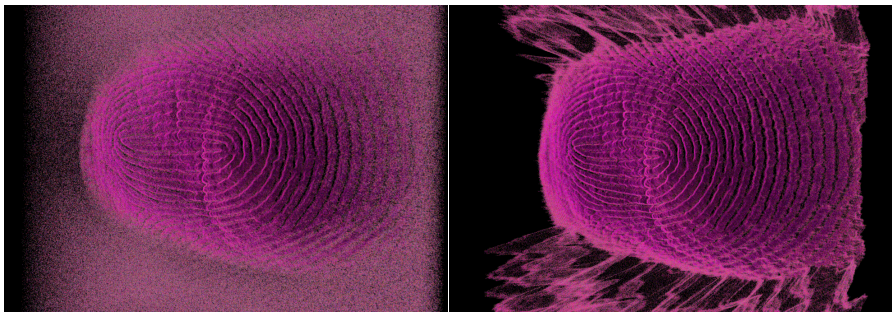

Figure 6.2: Index finger; (a) noisy 3D point-cloud obtained by direct edge-detection filtering along the scan-lines at full resolution only; (b) continuous 3D fingerprint surface (for comparison)

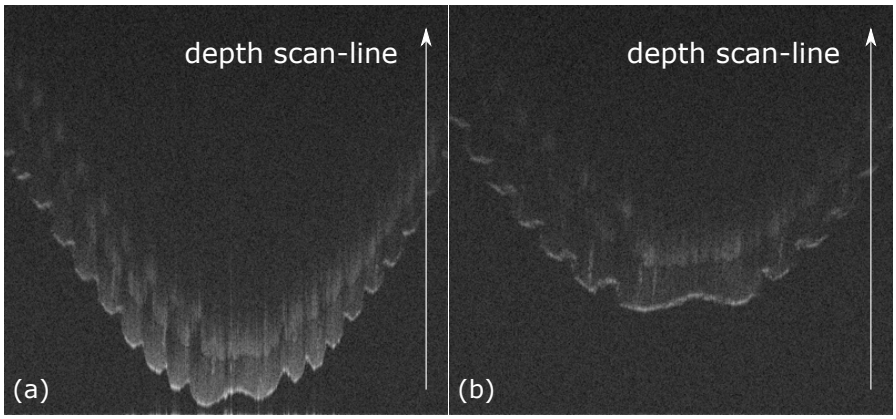

Figure 6.3: OCT finger 2D slices - inner and outer fingerprint edges visualization

sampling the OCT scan in all three dimensions, we have taken an approach where the pyramid is built by downsampling the scan always to $1/2$ in width and height, leaving the depth dimension unaltered as illustrated by Fig. 6.4. The detection of the full-resolution outer fingerprint surface, $outer_0(x, y)$, is then performed iteratively using the Alg. 6.1.

The rationale is that it is far more likely to correctly detect the position of the fingerprint surface in a more downsampled scan, since the down-sampling heavily reduces the noise levels. If the higher-resolution surface that is being extracted in iteration n, $outer_n(x, y)$, is then searched for only in the proximity of the lower-resolution surface, $outer_{n+1}(x, y)$, detected in a more downsampled version of the scan, the likelihood of a correct detection is greatly increased. This creates an iterative chain where the lower-resolution surfaces

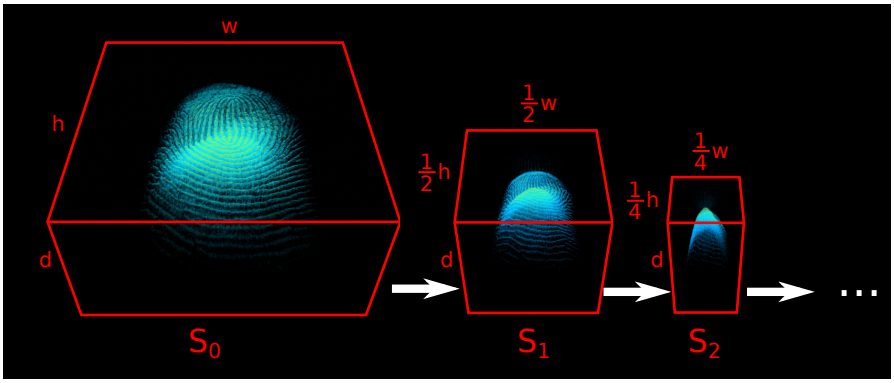

Figure 6.4: Downsampling of the OCT scan along the width and height dimensions

obtained from the more-downsampled lower-resolution and as such less-noisy versions of the scan serve as a prediction of where the surface should be in the next higher-resolution iteration.

In addition, detecting the surface, $outer_n(x, y)$, only in a distance, d_n, from a lower resolution surface $outer_{n+1}(x, y)$, allows for a significant speed-up since the entire scan does not need to be processed on any but the most downsampled level.

Algorithm 6.1: Outer fingerprint detection

1 Copy data from RAM to the GPU;
2 From the original OCT fingerprint scan, $V_0(x, y, z)$, generate N additional versions of the OCT scan, $V_1(x, y, z)...V_N(x, y, z)$, each downsampled to $1/2$ of the previous one along width and height dimensions;
3 While filtering the scan-lines using the edge detection filter, detect the maximum position in each $V_N(x, y)$ scan-line and store it to $outer_N(x, y)$;
4 **for** *each n in* $N - 1$ *to 0* **do**
5 Up-sample $outer_{n+1}(x, y)$ by a factor of two into $region_n(x, y)$
6 While filtering the scan-lines using the edge detection filter, detect the maximum position in each $V_n(x, y)$ scan-line and store it to $outer_n(x, y)$ IF at a distance d_n from $region_n(x, y)$;

6.3.4 Fingerprint Flattening

After the outer fingerprint surface, $outer_0(x, y)$, has been identified at full resolution, the detection of the inner fingerprint surface constitutes the natural

next step. The inner fingerprint is more difficult to detect, compared to the outer fingerprint, since the contrast between the inner fingerprint and and surrounding tissue is much lower than the contrast between the outer fingerprint and the empty air - Fig. 6.3.

In addition, the depth at which the inner fingerprint appears in various people varies widely. (The maximum inner fingerprint depths in the dataset are commonly 5x greater than the minimum depths.) If one attempts to detect the inner fingerprint simply as a second surface around the outer surface, $outer_n(x, y)$, the outer fingerprint easily interferes with the inner fingerprint on the more downsampled versions of the scan and the detection is highly unreliable, especially for fingers where the distance between the inner and outer layer is rather small.

In order to address this issue, we perform full flattening of the original OCT scan according to the identified outer fingerprint surface. By flattening we mean re-arranging of the data along the z-axis using the following equation (Fig. 6.5):

$$V_0(x, y, z) \leftarrow V_0(x, y, z - outer_0(x, y)) \tag{6.1}$$

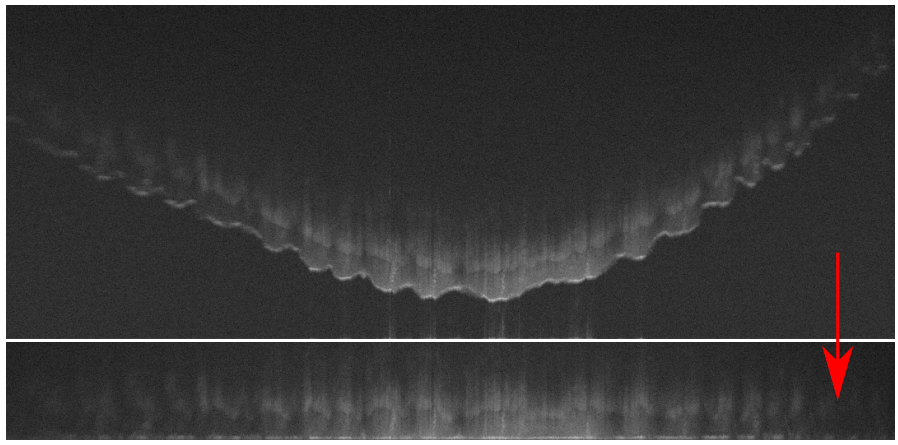

Figure 6.5: fingerprint flattening - a cut through the fingerprint scan before and after the flattening procedure (5 averaged slices)

6.3.5 Inner Fingerprint Surface

The re-arranged data naturally put any remnants of the outer fingerprint close to the bottom of the scan. This prevents interference of the outer fingerprint during the inner fingerprint detection.

Even though the algorithm, used for extracting the inner fingerprint surface, is similar to the algorithm for extracting the outer fingerprint surface, there are two important differences.

The inner fingerprint surface is not searched using a constant filter size, but rather an adaptive filter size. This is necessary to handle the cases of very thin inner layers, where the inner fingerprint is very close to the outer one. It also improves performance for the fingerprint where the the distance between the outer and inner fingerprint surface is large, and as such a larger filter size can perform much more reliably.

The inner fingerprint surfaces, detected even in the most down-sampled versions of the flattened OCT scan, can still contain significant number of errors. This appears to be caused by interference of the inner fingerprint with itself, if a significant amount of down-sampling is considered. The problem is mitigated by a guessing procedure, where any detected points that deviate too much from the average depth range are replaced by a position that gained maximum response in a histogram of the detected positions - by the most likely depth encountered. Although this could seem to damage the inner fingerprint surface, in practice, it provides a precise-enough estimate for the higher-resolution detection steps, and the technique can recover even from severe failures encountered at the most down-sampled level.

The concept is described by Alg. 6.2.

6.3.6 Surface Conversion to 2D Fingerprint

We extract the fingerprint into 2D representation by utilizing the identified 3D surface, masking out the random noise that appears where the finger was not present - Fig. 6.8, 6.11. The concept is described by Alg. 6.3.

Algorithm 6.2: Inner fingerprint detection

1 Flatten the fingerprint according to Eq. 6.1;
2 From the flattened OCT fingerprint scan, $V_0(x, y, z)$, generate N additional versions of the OCT scan, $V_1(x, y, z)...V_N(x, y, z)$, each downsampled to $1/2$ of the previous one along width and height dimensions (re-calculate the pyramid for the flattened scan);
3 $optimal\_filter\_size = DetermineOptimalFilterSize()$ (Alg. 6.4);
4 set $optimal\_filter\_size$ as the edge detection filtering size for all further operations;
5 While filtering the scan-lines using the edge detection filter, detect the maximum position in each $V_N(x, y)$ scan-line and store the maxima positions to $inner_N(x, y)$ and the value of the maxima (the response of the filter at the maxima positions) to $confidence_N(x, y)$;
6 **for** *each n in* $N - 1$ *to 0* **do**
7 **if** $n > ec\_depth\_limit$ **then**
8 Calculate a weighted histogram $h(d)$ of $inner_{n+1}(x, y)$ using $confidence_n(x, y)$ as weights;
9 Gaussian blur the $h(d)$ as a 1D function;
10 Detect the maxima, m, and its position, p, in $h(d)$;
11 From the position, p, search to the right and to the left in $h(d)$ until a number smaller than $m \cdot ratio$ is encountered (intuitively, measure the width of the peak in the histogram);
12 Utilize the identified positions to calculate the acceptable level of deviation, $inner\_layer\_deviation$;
13 Process $inner_{n+1}(x, y)$ such that any value further than $inner\_layer\_deviation/2 \cdot d\_ratio$ from m is replaced by m (Replace values too far from the average by the average value)
14 Up-sample $inner_{n+1}(x, y)$ by a factor of two into $region_n(x, y)$;
15 While filtering the scan-lines using the edge detection filter, detect the maximum position in each $V_n(x, y)$ scan-line and store the maxima positions to $inner_n(x, y)$ and the value of the maxima (the response of the filter at the maxima positions) to $confidence_n(x, y)$ IF at a distance d_n from $region_n(x, y)$;

Algorithm 6.3: 2D fingerprint extraction

1 Process the 3D fingerprint surface, inner or outer, $s(x, y)$, by a 2D Gaussian core and store to $s_{blurred}(x, y)$;
2 $s_{subtracted} \leftarrow (s - s_{blurred}) \cdot fingerprint\_height\_ratio$;
3 $s_{fingerprint}(x, y) \leftarrow s(x, y)$ IF $s(x, y) \in [0, 1]$;
4 $s_{fingerprint}(x, y) \leftarrow 1$ IF $s(x, y) > 1$;
5 $s_{fingerprint}(x, y) \leftarrow 0$ IF $s(x, y) < 0$;
6 Threshold the confidence map $confidence(x, y)$ into fingerprint and empty area, median filter to remove holes, and utilize to mask out the noisy areas;

Algorithm 6.4: Determining optimal filter size

1 **Function** *DetermineOptimalFilterSize ()*
2 $current\_maxima = -INF$;
3 **for** *each* $tested\_filter\_size$ *in* l *to* h *with step* s **do**
4 While filtering the scan-lines using the edge detection filter, detect the maximum position in each $V_N(x, y)$ scan-line and store the maxima positions to $inner_N(x, y)$ and the values of the maxima (the response of the filter at the maxima positions) to $confidence_N(x, y)$;
5 Calculate a weighted histogram $h(d)$ of $inner_N(x, y)$ using $confidence_N(x, y)$ as weights;
6 Gaussian blur the $h(d)$ as a 1D function;
7 Detect maxima m in $h(d)$;
8 **if** $m > current\_maxima$ **then**
9 set $current\_maxima \leftarrow m$;
10 set $optimal\_filter\_size \leftarrow tested\_filter\_size$;
11 **return** $optimal\_filter\_size$;

6.4 Results

As discussed above, the fingerprint surfaces are first extracted by our method as depth maps that describe the 3D structure of the particular fingerprint surface (Alg. 6.1, 6.2). The extracted fingerprint surfaces are then used to extract 2D fingerprint images (Alg. 6.3).

Fig. 6.6 visualizes an index finger OCT scan. The corresponding extracted surfaces, both for the outer fingerprint and the inner fingerprint, are illustrated by Fig. 6.7. The associated 2D fingerprints are illustrated by Fig. 6.8. Fig. 6.9 visualizes an OCT fingerprint scan of a thumb. The fingerprint surfaces extracted from the scan are illustrated by Fig. 6.10 and the corresponding 2D fingerprints by Fig. 6.11.

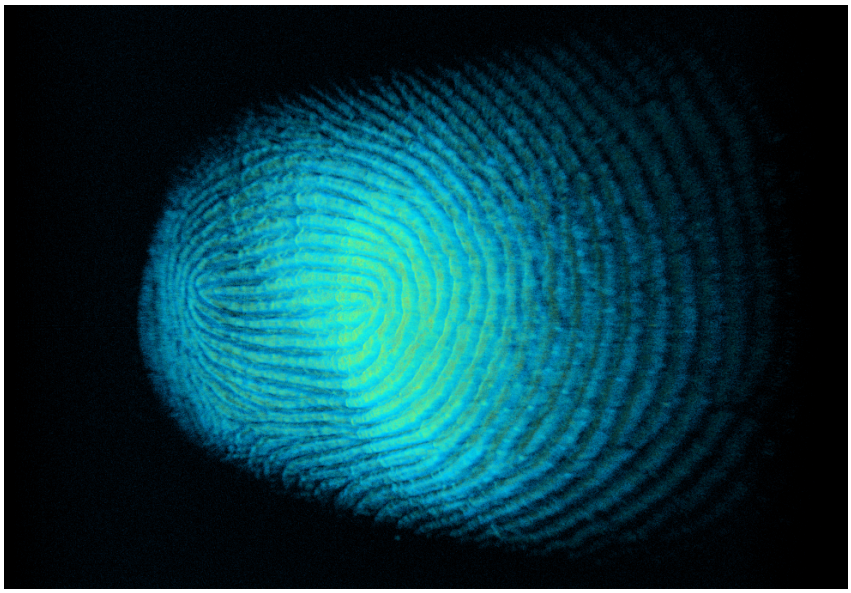

Figure 6.6: Index finger; 3D scan visualization

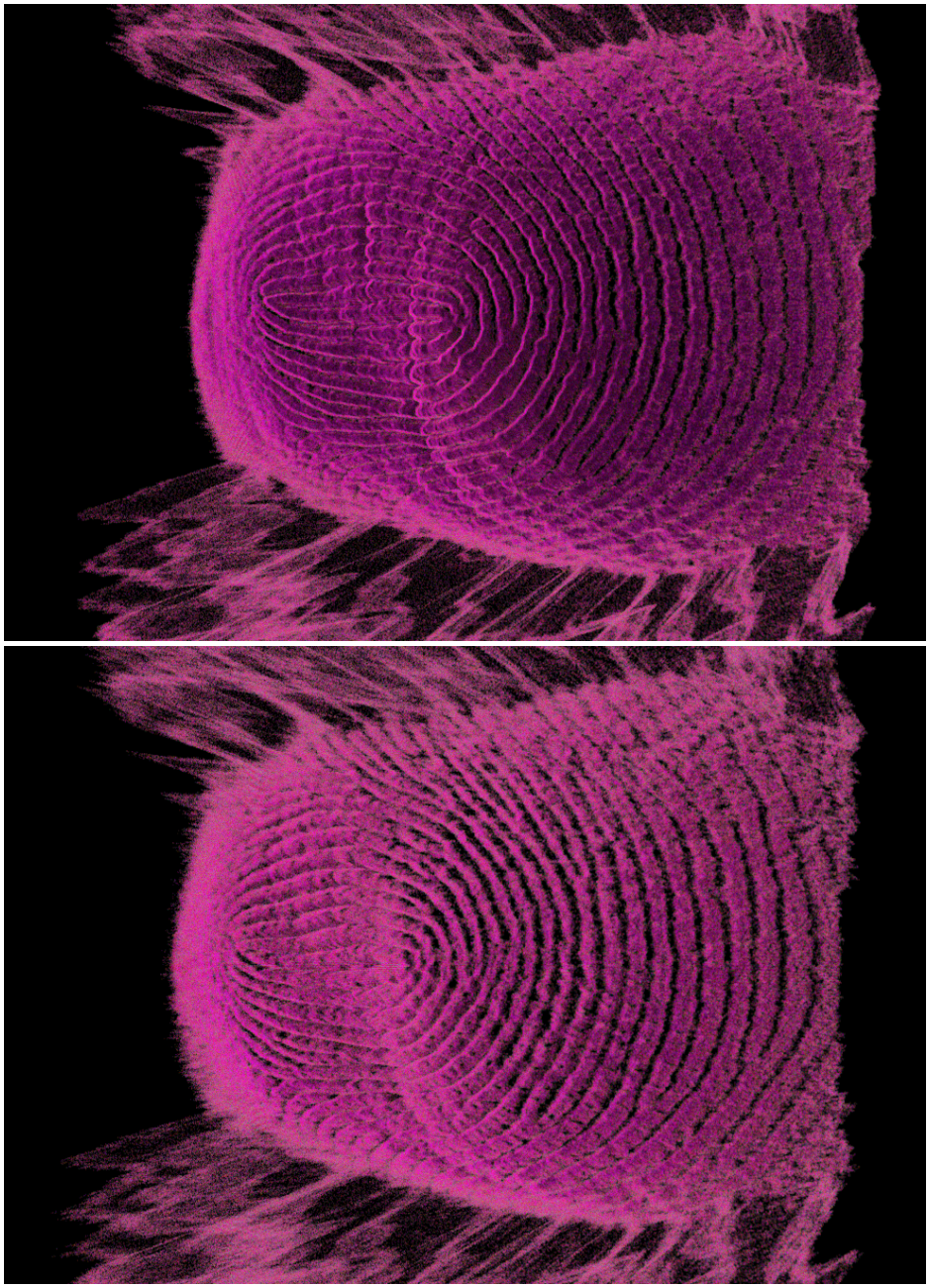

Figure 6.7: Index finger; Top: outer fingerprint surface; Bottom: inner fingerprint surface

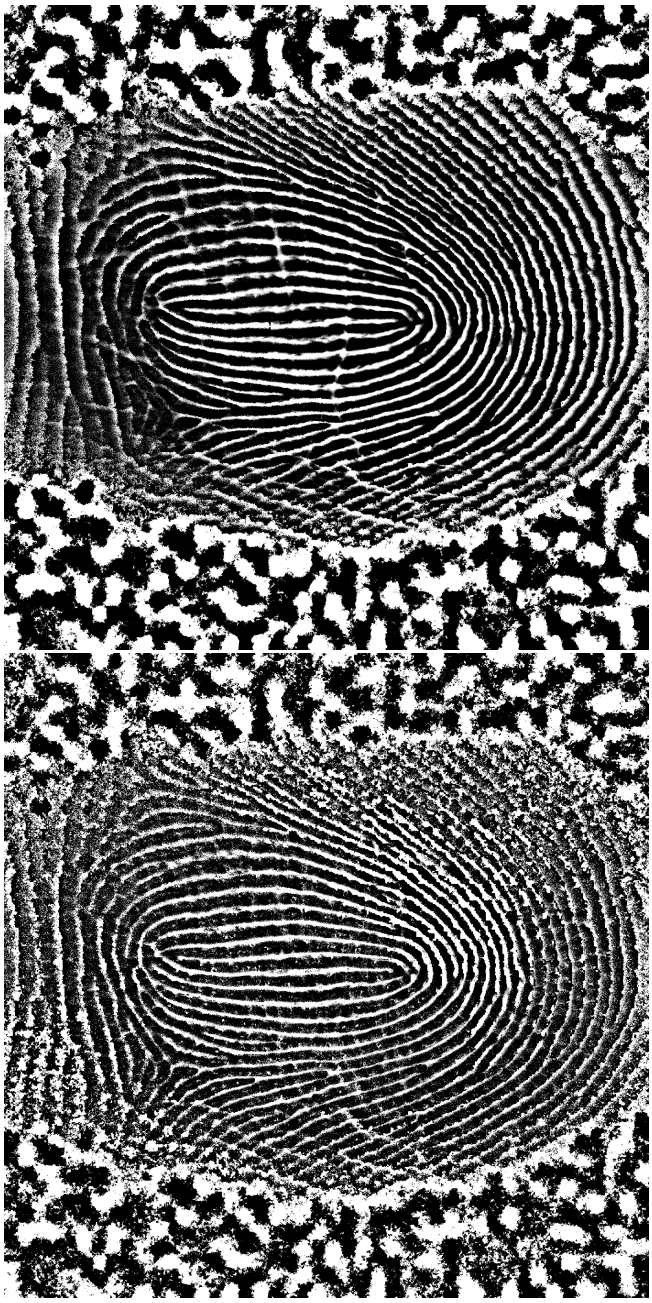

Figure 6.8: Index finger; Top: 2D outer fingerprint; Bottom: 2D inner fingerprint

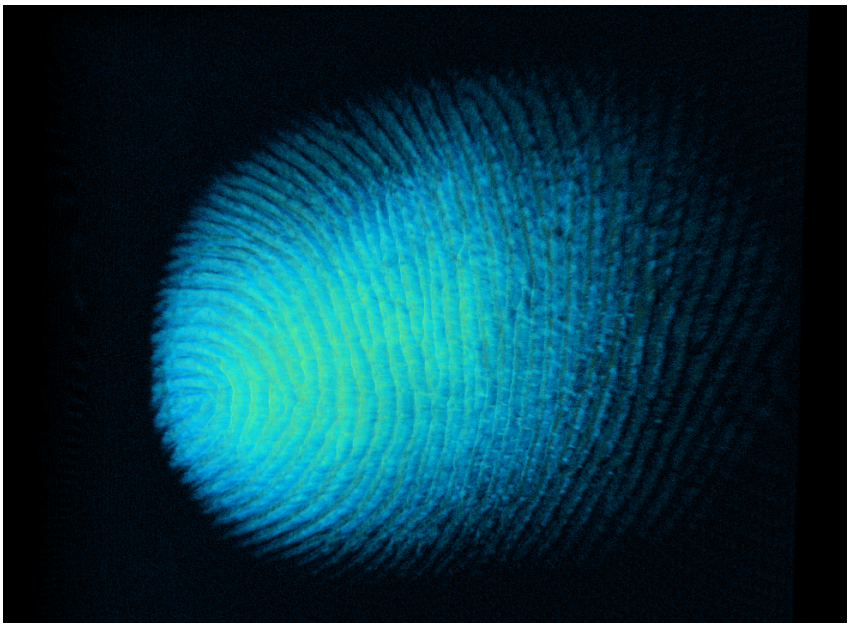

Figure 6.9: Thumb; 3D scan visualization

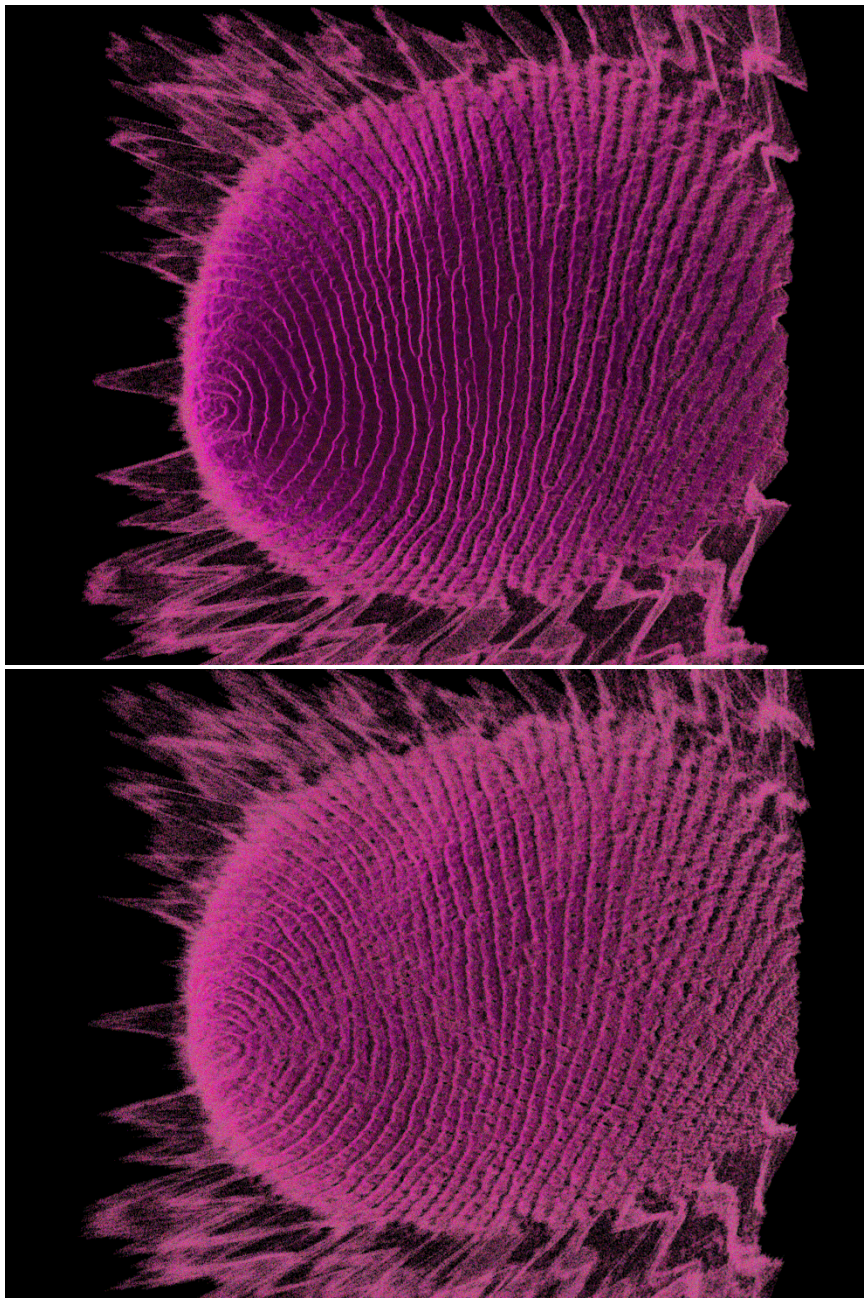

Figure 6.10: Thumb; Top: outer fingerprint surface; Bottom: inner fingerprint surface

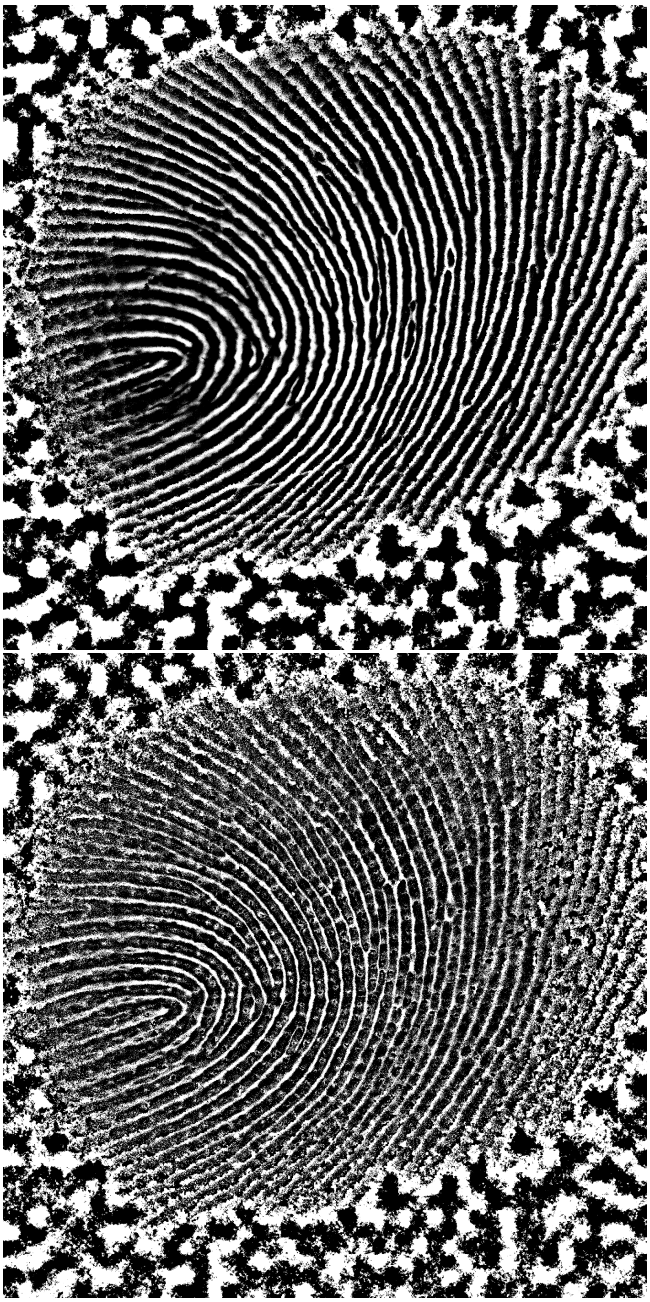

Figure 6.11: Thumb; Top: 2D outer fingerprint; Bottom: 2D inner fingerprint

Direct comparison with the method of Darlow et al. [28] is difficult, since we were not able to obtain the codes/executables from the authors and we do not have any opportunity to share the data either due to their sensitive nature. However, we believe our method clearly outperforms the method of Darlow et al. [28] for the following reasons:

- Our approach using adaptive filter size allows processing of the cases where the inner fingerprint is at very small depth - something that is not possible using a simple 3-point edge detector on a scan down-sampled in all 3 dimensions as in [28]
- Our approach uses a filter with a wide support, which allows obtaining a much higher quality surface than in [28]
- Darlow et al. [28] did not follow the path of extracting the 2D fingerprints directly from the 3D surface, and instead utilized the surface simply as an estimate of the fingerprint positions. The fingerprint is read off from the original scan by averaging the data above and below the estimated surface. Our method does not require this, in fact, we were able to obtain complete fingerprints using the layer information alone.

Nevertheless, we utilized the fingerprint surfaces as detected by our method to replicate the fingerprint extraction technique proposed in [28] - by averaging around the surface in the original scan. The results are illustrated by Fig. 6.12.

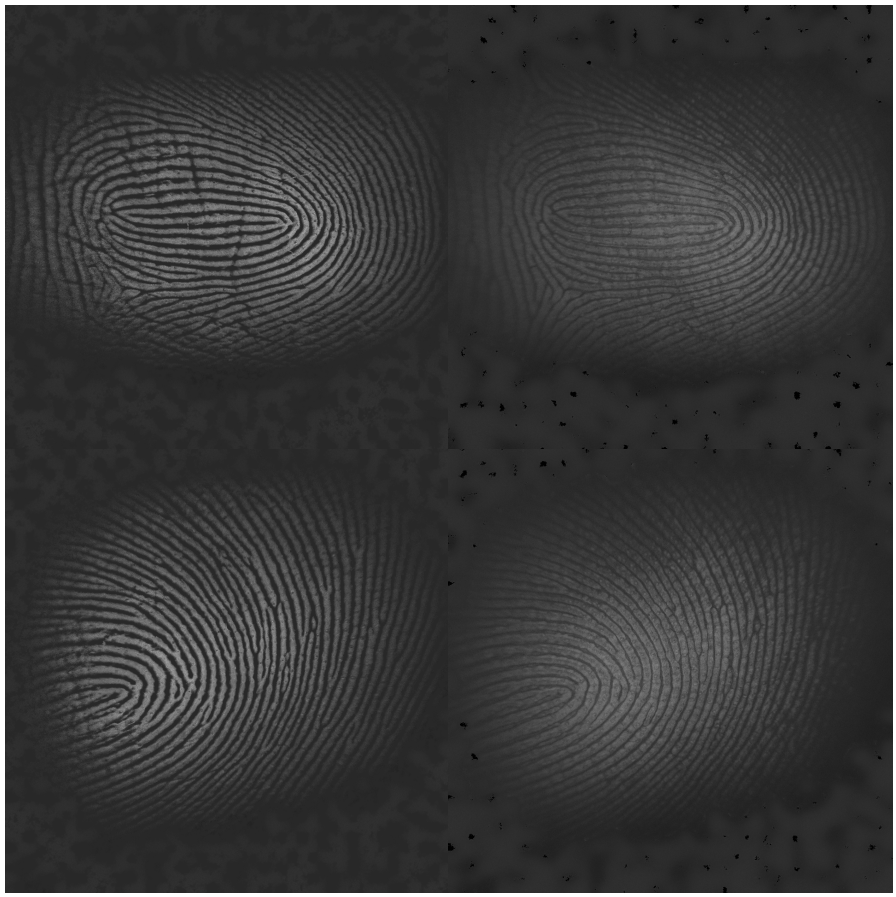

Figure 6.12: 2D fingerprints extracted by averaging around the detected surface similarly to Darlow et al. [28]; Top: index finger - outer (left) and inner (right) fingerprint; Bottom: thumb - outer (left) and inner (right) fingerprint;

6.4.1 Compatibility with 2D Fingerprints

To further prove the robustness of our approach as well as test the compatibility of 3D-OCT-based and standard 2D fingerprinting, we performed a cross-comparison of the fingerprints extracted from the OCT fingerprint scans using our method and the 2D fingerprints acquired using a standard 2D fingerprint sensor from the above mentioned dataset.

Fig. 6.13 illustrates the results of comparing each OCT-extracted outer fingerprint to each 2D standard-sensor fingerprint. Fig. 6.14 illustrates the results of comparing each OCT-extracted inner fingerprint to each standard-sensor 2D fingerprint.

The metrics considered are the propotion of miss-classified comparisons

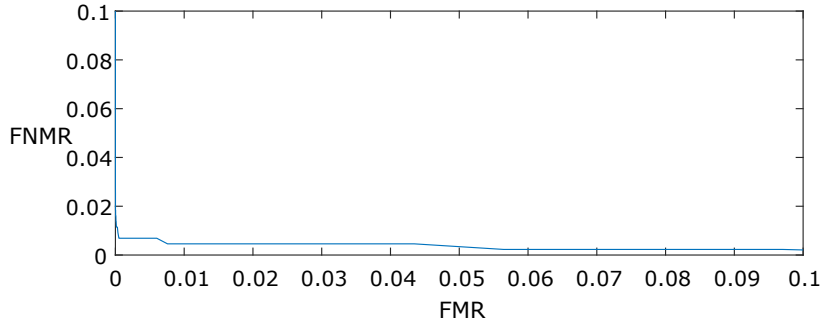

Figure 6.13: DET curve for the outer fingerprints and the 2D fingerprints comparisons

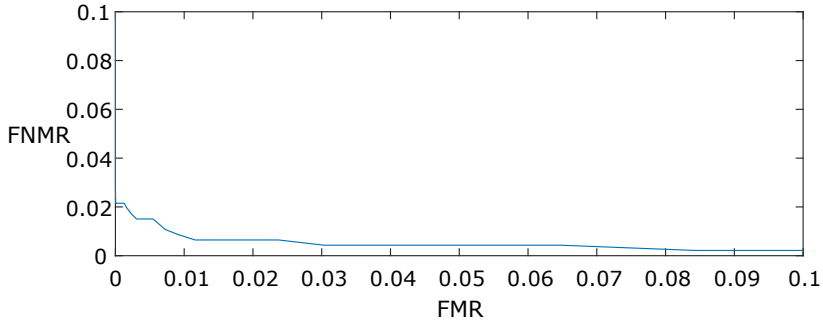

Figure 6.14: DET curve for the inner fingerprints and the 2D fingerprints comparisons

of identical fingerprints, false non-match rate (FNMR), and the proportion of miss-classified comparisons of non-identical fingerprints, false match rate (FMR). The failure to extract (FTX) metric expresses the proportion of fingerprints the comparison software failed to extract fingerprint features from [52]. The outer fingerprints compared to the 2D fingerprints with an equal-error-rate (EER) of 0.7% and a FTX rate of 11%. The inner fingerprints compared to the 2D fingerprints with EER of 1% and a FTX rate of 3.5%. For comparison, the 2D fingerprints from a commercial sensor resulted in FTX of 3.4%. The fingerprints were compared using the commercial fingerprint identification software Verifinger 9.0.

6.4.2 Speed & Memory

The durations of the different stages of the fingerprint extraction pipeline, averaged over all scans in the dataset, are listed in Tab. 6.1. The measurements were taken either using the cuda GPU time measurement API or using the

standard C CPU time measurement API. For the CPU measurements, synchronization with the GPU was always performed prior to the measurement, such that all previously issued GPU computations are guaranteed to be finished.

The pipeline requires 3GB of GPU RAM, where 2GB are taken by the scan data and less than 1GB is used for storing the generated image pyramid, the results of the fingerprint surface detection and other intermediary variables.

6.5 Conclusion and Future Work

Based on the fact that the inner fingerprint seems to perform better than the outer fingerprint, considering the FTX, we believe it is indeed very promising to expect significant improvements from the OCT regarding enrollment of individuals with outer fingerprints of insufficient quality that cannot be handled by current 2D sensors. At the same time, the fingerprints already do perform close to practical error rates - in spite of the significant potential of our custom-built OCT scanner for improvements. Our technique can process a 2GB scan in less than 1.25 s on an older GTX 660 Ti GPU with 3GB RAM, which shows promise both regarding the speed and memory associated challenges.

The future work would involve further improvements of the underlying scanner design. In addition, the method for the detection of the outer fingerprint could probably benefit from further improvements.

Table 6.1: Duration of different stages of the processing pipeline on different NVIDIA GeForce GPU models (average over all scans in the dataset); (CPU - measurement on CPU, GPU - measurement on GPU)

	GTX 980 4GB (ms)	GTX 780 3GB (ms)	GTX 660 Ti 3GB (ms)
CPU-GPU scan copy (CPU)	438.42	643.20	428.70
image pyramid allocation (GPU)	3.48	4.46	4.34
V_0 to V_1 downsampling (GPU)	15.44	16.12	23.64
V_1 to V_2 downsampling (GPU)	3.97	3.49	6.57
V_2 to V_3 downsampling (GPU)	1.14	0.97	1.79
V_3 to V_4 downsampling (GPU)	0.28	0.28	0.46
V_4 to V_5 downsampling (GPU)	0.10	0.20	0.17
V_5 outer layer detection (GPU)	0.49	0.94	0.86
V_4 outer layer detection (GPU)	0.62	1.15	1.13
V_3 outer layer detection (GPU)	1.61	2.54	3.50
V_2 outer layer detection (GPU)	3.76	6.95	10.88
V_1 outer layer detection (GPU)	10.10	21.77	34.12
V_0 outer layer detection (GPU)	18.25	24.10	39.50
2D outer fingerprint from 3D surface (CPU)	41.42	41.14	41.68
total outer print (including extra glue code, after data copy to GPU) (CPU)	133.98	162.12	207.40
fingerprint flattening (GPU)	146.63	64.63	281.17
V_0 to V_1 downsampling of the flattened scan (GPU)	24.20	22.13	29.41
V_1 to V_2 downsampling (GPU)	3.97	3.48	6.59
V_2 to V_3 downsampling (GPU)	1.13	0.96	1.79
V_3 to V_4 downsampling (GPU)	0.27	0.27	0.46
V_4 to V_5 downsampling (GPU)	0.10	0.19	0.16
determining filter size (CPU)	89.69	104.84	101.17
V_5 inner layer detection (GPU)	0.47	0.92	0.81
V_4 inner layer detection (GPU)	0.28	0.46	0.41
V_3 inner layer detection (GPU)	0.68	0.86	1.09
V_2 inner layer detection (GPU)	2.16	2.84	4.20
V_1 inner layer detection (GPU)	7.77	12.78	17.97
V_0 inner layer detection (GPU)	28.64	46.88	65.85
2D inner fingerprint from 3D surface (CPU)	48.29	47.73	48.46
total inner print (including extra glue code) (CPU)	375.58	330.23	582.12

Chapter 7

Sweat Glands Detection

7.1 Summary

This chapter proposes a novel fast memory-efficient filter-size-independent scheme for calculating 3D Difference of Gaussians (DoG) both on CPUs and GPUs. The DoG-filtering scheme is used to emphasize the sweat glands in volumetric OCT fingerprint scans and a multiple-source multiple-target graph-based shortest path searching algorithm is proposed for detection of the paths taken by the sweat glands inside the fingerprint scans. The work is planned for submission to the IET Biometrics journal.

7.2 Introduction

Regarding the problem of robust detection whether a genuine human finger was scanned - the problem of Presentation Attack Detection (PAD) - the OCT fingerprint scans contain multiple useful features.

One of the most apparent features, apart from the inner fingerprint scanned from underneath the skin surface, are the sweat glands. The sweat glands are spiral structures, which can be observed between the fingerprint surface and the inner fingerprint layer in the OCT scan. A sweat gland ends on the surface of the fingerprint ridge as a sweat pore, which releases the sweat fluid generated by the sweat gland in the process of perspiration.

Due to their microscopic size and irregular biological spiral shape, the sweat glands can be expected to be extremely hard to replicate in artifact fingerprints. A method for their reliable detection (and the subsequent analysis of their shape) could therefore provide for a very strong fingerprint PAD solution.

7.3 Challenges

The sweat glands are captured by the OCT as spiral structures starting at the pores on the fingerprint ridges and ending at the boundary of the sub-surface inner fingerprint - Fig. 7.1.

In the previous chapter, a method has been developed that can provide for the 3D surfaces, $outer_0$ and $inner_0$, that describe the positions of the outer

and inner fingerprints in the OCT scan (see Algorithms 6.1, 6.2). Additionally, an OCT scan flattening procedure according to the outer fingerprint surface $outer_0$ has been implemented as follows (Fig. 7.1):

$$V_f(x, y, z) \leftarrow V_0(x, y, z - outer_0(x, y)) \tag{7.1}$$

If the OCT scan has been flattened according to Eq. 7.1, the problem of searching for the sweat glands is simplified to detecting them as spiraling structures starting at the bottom of the flattened scan and ending close to the inner fingerprint boundary.

However, the directions of the sweat glands can deviate significantly from the strictly vertical direction in both of the lateral coordinates.In some cases, their direction also cannot be well approximated by a strictly linear path, but rather by a slightly curved shape. These properties suggest a need for a rather generic approach that could handle the search for each sweat gland as a search for a rather generic path from the bottom to the top of the flattened fingerprint volume (Fig. 7.1).

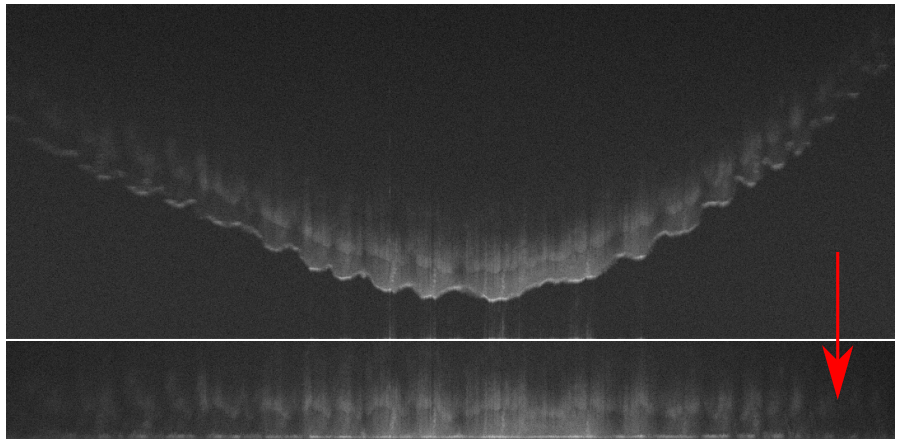

Figure 7.1: fingerprint flattening - a cut through the fingerprint scan before and after the flattening procedure (5 averaged slices)

In addition, the volume between outer fingerprint surface, $outer_0$, and the inner fingerprint surface, $inner_0$, represents a significant amount of volumetric data to analyse. This poses a challenge regarding the speed of the processing considering the total processing times of a few seconds necessary for typical applications of fingerprint biometrics such as border control. Since we ultimately aim for a version of our OCT fingerprint scanner as an embedded system with a limited size and cost, the memory requirements of the processing algorithm are also of significant interest. The combination of the strong requirements on the low memory usage and the high processing speed suggests the need for a novel domain-specific approach rather than the usage of

existing medical imaging methods - many of which are well suited only for systems offering only a limited level of parallelism, such as the CPU, and not for massively-parallel systems as as the GPUs.

7.4 Memory Efficient 3-D Difference of Gaussians

Difference of Gaussians (DoG) operator is a well-known and commonly used initial step in various edge and blob detection approaches, and as such, represents an important building-block of many modern computer vision algorithms.

The DoG-based blob detection algorithms are typically based on the ability of the DoG operator to smoothen the image (handling the image noise in robust fashion) and, at the same time, point out the centers of the blobs in the original image as maxima in the DoG-filtered image. As such, by searching the DoG-filtered image for local maxima, it is possible to identify blobs in the original image.

Since the sweat glands can be seen as prolonged 3D blobs taking a rather linear path from the bottom of the flattened OCT fingerprint scan to the inner fingerprint layer, filtering with a 3D DoG operator appears to be a natural processing step in the detection of the paths the sweat glands are taking. The 3D DoG simultaneously operates in all 3 dimensions, offering much better potential for noise resilience than any approach that would attempt to divide the volumetric data into 2D slices that would be processed separately. Even though division into (and separate processing of) 2D slices is a common approach for analyzing 3D volumetric data, it involves some level of disregarding the full 3D neighborhood of every voxel during the analysis. Given the noise levels typical for the OCT data, this would be a suboptimal approach.

7.4.1 2-D Difference of Gaussians

For 2D-images, the DoG-filtered result can be computed by filtering the image by two 2D Gaussian cores of different, σ_1 and σ_2, parameters. The resulting filtered images are subtracted from one another, emphasizing the edges and blobs as local extrema. Intuitively, the two resulting images, Gaussian-blurred to a different extent, will differ exactly at the edge boundaries. In addition, assuming that the two Gaussian cores are larger in size than the blobs in the original image, local extrema will be generated at the centers of weight of the blobs.

The computational efficiency of filtering with the DoG-operator depends directly on the ability to efficiently compute the convolution of the original image with the Gaussian core. Fortunately, the Gaussian core is separable, which allows, in the case of the 2D images, for filtering in two separate filtering passes in the horizontal and vertical direction.

7.4.2 3-D Difference of Gaussians

This property of separability extends to filtering of the volumetric data with a 3D Gaussian core - 3 separate filtering passes in the vertical, horizontal and depth directions are necessary. In case of the volumetric data, the separability of the Gaussian core is a crucial property for computation of the 3D Gaussian-blurred version of the original volumetric data, since the direct convolution of 3D data with a 3D convolution core would generate extremely large and very likely impractical computational demands.

In order to perform a separable 3D Gaussian filtering of volumetric data, 3 separate 1D filtering passes are necessary - all the data have to be processed along the x, y and z axes. However, the existing fast methods for performing the elementary step of 1D Gaussian filtering, which is necessary for computation of a full 3D Gaussian blurred version of 3D volumetric data, do require additional memory buffers as discussed in detail in Chapter 5. This need for additional memory buffers for the 1D filtering passes results in the requirement for an extra memory buffer of the full size of the 3D Gaussian-filtered 3D volumetric data.

The amount of extra memory needed becomes even more severe for the 3D DoG computation. Computation of the 3D DoG requires two extra memory buffers of the size of the original volumetric data, very likely at higher precision than the original data in order to achieve high sensitivity of the DoG operator. For example, a 1GB of 8-bit volumetric data could easily require extra $4 + 4 = 8$ GB of memory buffers at the 32-bit floating point precision in order to compute the 3D DoG.

Naturally, it is possible to try to divide the volume into sub-volumes and process those separately, but this will lead to issues with overlaps between the 3D sub-volumes (due to boundary issues) and will become inefficient for larger filter sizes.

Based on the novel single-pass filter-size-independent 1D Gaussian filtering technique introduced in Chapter 5, we propose a following novel scheme for fast filter-size independent and memory-efficient computation of the DoG operator. Our scheme is possible due to the fact that our proposed 1D Gaussian filtering approach, which serves as the essential building-block in the separable 3D DoG filtering, operates in a single pass without the need for additional memory buffers.

Our fast memory-efficient 3D DoG filtering scheme is shown in Fig. 7.2 and described by Algorithm 7.1.

The proposed scheme offers a very low intermediary memory footprint, requiring only a limited number of 2D slices as intermediary buffers - completely independently of the DoG filter size. 4 2D slices are needed in order to store the content of the 4 accumulators (necessary for our single-pass 1D Gaussian filtering technique (see Chapter 5)) for each each of the two σ_1 and σ_2 filterings. In addition, a 2D slice for storage the partial filtered data is needed for each of the σ_1 and σ_2 filterings, before the final slice of 3D DoG

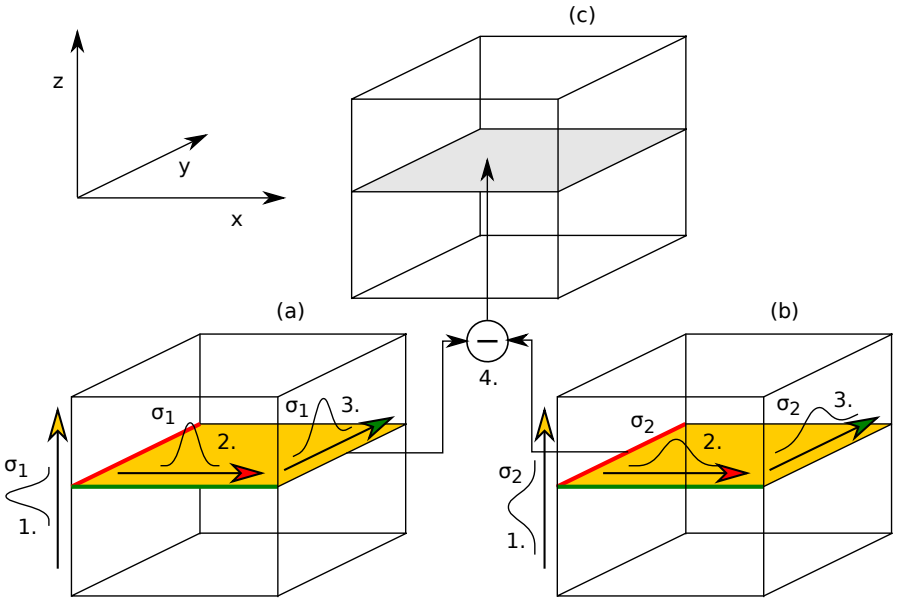

Figure 7.2: The proposed memory-efficient 3D DoG filtering scheme; (a) a step of filtering of the 3D volume by a Gaussian core of σ_1; (b) a step of filtering of the 3D volume by a Gaussian core of σ_2; (c) a step of 3D DoG filtered results; 1. filtering of the volume producing a 2D slice filtered by a 1D Gaussian core along the z axis; 2. filtering of the 2D slice from step 1. along the x axis by a 1D Gaussian core; 3. filtering of the 2D slice from step 2. along the y axis by a 1D Gaussian core; 4. subtraction of the two 2D slices filtered (σ_1 and σ_2) in order to compute the resulting 3D DoG filtered slice

filtered results can be computed.

7.4.3 GPU Implementation

The GPUs are massively-parallel systems and require a significant amount of tasks possible to perform in parallel in order to have their computational potential fully utilized. Even though the proposed 3D DoG filtering scheme as described by Algorithm 7.1 does readily allow for a certain level of parallel computation of the 1D filtering passes, the amount of parallelism is rather insufficient for modern GPUs. The bottleneck of the scheme described by Alg. 7.1 comes in the steps of the filtering of the 2D slices. 1D filtering of a 2D slice along a particular axis, all scan-lines in parallel, does not typically offer enough parallel tasks for a modern GPU.

Another challenge is associated with the typical speed-critical requirement for memory-coalesced access to the data on single instruction multiple data (SIMD) systems such as GPUs. For a coalesced data access, a single SIMD

Algorithm 7.1: The proposed memory-efficient 3D DoG filtering scheme

foreach *2D slice,* $S(x, y)$*, in the 3D volume* $V_f(x, y, z)$ **do**
- using the single-pass filter-size-independent Gaussian filtering technique described in Chapter 5, calculate two 2D slices, $G_1^z(x, y)$ and $G_2^z(x, y)$, of the original volume Gaussian filtered along the z axis with parameter σ_1 and σ_2;
- Gaussian filter the 2D slices, $G_1^z(x, y)$ and $G_2^z(x, y)$, along the x axis with parameters σ_1 and σ_2, producing slices $G_1^{zx}(x, y)$ and $G_2^{zx}(x, y)$;
- Gaussian filter the 2D slices, $G_1^{zx}(x, y)$ and $G_2^{zx}(x, y)$, along the y axis with parameters σ_1 and σ_2, producing 3D Gaussian filtered slices $G_1^{zxy}(x, y)$ and $G_2^{zxy}(x, y)$;
- Subtract the 2D slice, $G_2^{zxy}(x, y)$, from the 2D slice, $G_1^{zxy}(x, y)$, obtaining the resulting $DoG(x, y)$, which is a 2D slice of a fully 3D DoG filtered version of the original volume;

instruction accessing the data, representing a step of the computation of multiple parallel tasks at once, needs to request a continuous block of memory, rather than pieces of data scattered randomly across the address space.

When processing 2D images, all scan-lines in parallel along both the x and y axes, it is not possible to directly access the data in coalesced fashion when filtering along both axes. Depending on organization of the data in the memory (row-major vs. column major), one of the axes will not allow for direct coalesced access.

When processing a 3D volume in parallel along the scan-lines along all the x, y and z axes, it is not possible to find a combination of data storage and SIMD processing scheme that would lead to coalesced access for all the three axes. Depending on the organization of the 3D data in memory, one of the 3 axes will not allow for coalesced access.

An extra technical challenge regarding our GPU implementation is associated with the design choice of storing the volumetric OCT data as a 3D texture rather than raw data in the GPU memory. The 3D texture allows to utilize the hardware texture caches, and somewhat relaxes the hard requirements for the coalesced memory access for scenarios where data with narrow spatial locality are accessed. This design choice was made primarily to support more specific analysis of individual sweat glands in the future work, but could serve well also in order to support the speed of other processing approaches in the future, which do not fully meet the hard requirements for memory coalescing. For our 3D DoG implementation the usage of the texture memory means that, unlike for the raw data storage, the high speed access to the volumetric data is not possible along 2 out of 3 axes, but only along one of the axes. The other axis that would provide for high speed access in case of raw data storage,

does provide for a reduced access speed. This effect is caused by the special organization of the textures in memory of the GPU - supporting the speed of spatially localized access at the cost of the speed of the usual coalesced data access.

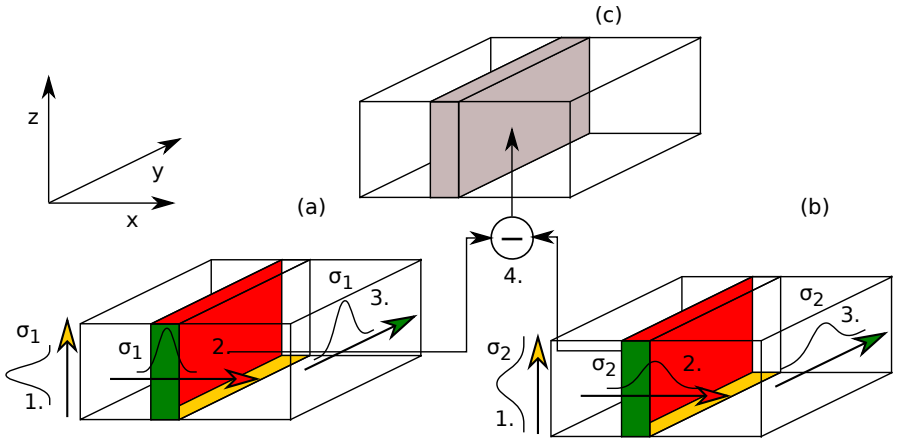

Figure 7.3: The proposed 3D DoG filtering scheme in our GPU implementation; (a) a step of filtering of the 3D volume by a Gaussian core of σ_1; (b) a step of filtering of the 3D volume by a Gaussian core of σ_2; (c) a step of 3D DoG filtered results; 1. filtering of the volume producing a small 3D sub-volume filtered by a 1D Gaussian core along the z axis; 2. filtering of the 3D sub-volume from step 1. along the x axis by a 1D Gaussian core; 3. filtering of the 3D sub-volume from step 2. along the y axis by a 1D Gaussian core; 4. subtraction of the two filtered 3D sub-volumes (σ_1 and σ_2) in order to compute the resulting 3D DoG filtered sub-volume

A GPU implementation that addresses the above mentioned GPU-specific challenges is described by Algorithm 7.2 and Fig. 7.3.

In order to provide for a sufficient level of parallelism while filtering along all 3 axes, as necessary for a high-speed GPU implementation, we iteratively filter 3D sub-volumes (Alg. 7.2, Fig. 7.3), $S(x, y, z)$, of the original volume V rather than 2D slices only as in the original version of proposed scheme (Alg. 7.1, Fig. 7.2). Even though this leads to increased memory requirements, it allows to fully utilize the parallel processing capabilities of the GPUs necessary for optimal performance regarding the speed of the DoG computation.

The single-pass nature of our Gaussian filtering scheme allows to seamlessly continue with filtering of the next sub-volume, without any additional computation due to boundary overlaps dependent on the filter size - the state of the filtering along the x-axis can be stored at the end of each iteration and re-loaded at the beginning of the next. As a consequence, the computational complexity of our GPU-specific DoG filtering scheme remains completely independent of the chosen filter size.

Algorithm 7.2: The proposed memory-efficient 3D DoG filtering scheme, GPU-specific implementation

1 **foreach** *3D sub-volume (non-overlapping),* $S(x, y, z)$*, in the 3D volume* V_f *(*x*-length of the sub-volume* $S(x, y, z)$ *is a multiple of* $thread\_count$ *(32))* **do**

2 using the single-pass filter-size-independent Gaussian filtering technique described in Chapter 5, calculate two 3D sub-volumes, $G_1^z(x, y, z)$ and $G_2^z(x, y, z)$, representing the sub-volume $S(x, y, z)$ as Gaussian filtered along the z axis with parameter σ_1 and σ_2;

3 Gaussian filter the 3D sub-volumes, $G_1^z(x, y, z)$ and $G_2^z(x, y, z)$, along the x axis with parameters σ_1 and σ_2, producing sub-volumes $G_1^{zx}(x, y, z)$ and $G_2^{zx}(x, y, z)$, reusing the filtering state information from previous iteration. During the filtering, transpose each $thread\_count$ x $thread\_count$ (32 x 32) patch along the dimensions (x, y), before storing to the buffer;

4 Gaussian filter the 3D sub-volumes, $G_1^{zx}(x, y, z)$ and $G_2^{zx}(x, y, z)$, along the y axis with parameters σ_1 and σ_2, producing 3D Gaussian filtered sub-volumes $G_1^{zxy}(x, y, z)$ and $G_2^{zxy}(x, y, z)$. The transposed data can be read full-speed in coalesced fashion;

5 Subtract the 3D sub-volume, $G_2^{zxy}(x, y, z)$, from the 3D sub-volume, $G_1^{zxy}(x, y, z)$, obtaining the resulting $DoG(x, y, z)$, which is a 3D sub-volume of a fully 3D DoG filtered version of the original volume V_f;

In order to provide for optimal performance of the fingerprint layers detection described in Chapter 6, the volumetric OCT fingerprint data are stored in the GPU memory in such way that the fastest coalesced access to the data is provided while filtering along the z-axis, where z-axis represents the in-depth direction into the scanned finger. Naturally, the depth range between the outer and inner fingerprint layers in a flattened OCT fingerprint scan is much smaller than the size of the fingerprint. As such, storing the yz 2D slices that represent the filtering state along the x-axis lead to least amount of extra memory requirements (Fig. 7.3). In order to keep the state when filtering along the x-axis and simultaneously allow for the data to be read in the first filtering pass along the fast coalesced z-axis, we maintain the filtering state in the second pass instead of the first pass as in the original scheme. This leads to increase of the intermediary memory buffer that must hold also the filtering results from the previous iteration regarding the overlap of the filtering core. However, this introduces dependence on the filter size only regarding the memory complexity - the computational complexity of the scheme remains filter size independent.

Regarding the above mentioned challenge of maintaining high-speed coalesced access to the volumetric data along all three axes, we perform trans-

position of every xy patch of size $thread\_count$ x $thread\_count$ (32 x 32 in the current GPUs) upon finishing the second x-axis filtering pass using the approach described in [14]. The transposed organization of the patches allows also the third y-axis filtering pass to read the data in full-speed coalesced fashion rather than in the significantly slower un-coalesced fashion.

7.5 Graph-based Sweat Glands Detection

Filtering by the 3D DoG operator allows to emphasize centroids of the sweat glands as maxima in the DoG-filtered version of the flattened OCT fingerprint scan. However, it is still necessary to detect clusters of these centroids in order to detect the position and path of an actual sweat gland.

We took an approach based on searching for multiple-source multiple-destination shortest paths in a graph. The DoG filtered flattened OCT fingerprint volume can be seen as a graph, where each voxel is connected to the voxels in its vicinity and the graph-distance is based on a function of the DoG amplitude at the two connected points, their mutual position (e.g. distance) and possibly other factors. We consider all the points at the bottom of the flattened volume - on the external fingerprint layer - the source points and try to find n shortest paths leading to the destination points on the inner fingerprint layer, since these paths are very likely to follow the paths of the sweat gland centroids.

7.5.1 Sparse Representation of the DoG Filtered Volume

Performing such a calculation on the full DoG filtered flattened fingerprint volume would very likely be prohibitive both spatially and computationally, since we need a careful approach even to store the OCT volumetric data and as such it is prohibitive, both spatially and computationally, to treat each voxel as a node in a graph. However, since the DoG operator emphasizes the centroids of the sweat gland paths as maxima in the DoG-filtered volume, it is possible to proceed with a sparse representation of the DoG filtered flattened fingerprint scan.

During the process of the GPU-based DoG filtering, our algorithm analyses tiny sub-volumes (8x8x4 voxels, adjustable setting) and identifies a voxel with maximum response of the DoG operator. Only the response of the identified voxel along with its original precise position is stored for further analysis - the identified maximum response voxel provides for a node for the graph analysis. The above described step allows to obtain a sparse representation with acceptable spatial and computational complexity of the shortest path detection.

7.5.2 Graph-processing for Sweat Glands Path Detection

The paths of the sweat glands in the sparse representation of the DoG-filtered flattened volumetric OCT fingerprint are searched as multiple-source multiple-target shortest paths from the bottom to the top of the sparse volume in a fashion similar to Dijkstra's shortest path algorithm [33].

The algorithm requires one upward pass and one downward pass through the sparse volume before the path of the sweat glands can be read off. The upward pass creates a map of shortest paths from the nodes at the bottom of the scan to each node inside the scan - Algorithm 7.3, Fig. 7.4. The distance function between two nodes, N_1 and N_2, has been experimentally determined as:

$$D(N_1, N_2) = (1.25 - \frac{a_2}{256})((x_1 - x_2)^2 + (y_1 - y_2)^2 + (z_1 - z_2)^2)^{0.75}, \quad (7.2)$$

where x_1, y_1, z_1 are the spatial coordinates of N_1; x_2, y_2, z_2 are the spatial coordinates of N_2; and a_2 is the amplitude (response of the DoG operator) of N_2.

Considering the data from the upward pass only, it is not easy to identify the most prominent paths yet, since many of the detected paths share sub-paths. In order identify a set of unique prominent paths from the bottom to the top of the sparse volume - the sweat glands paths - another downward pass through the data that resulted from the upward pass is performed - Algorithm 7.4, Fig. 7.5. The downward pass through the data ensures that no sub-paths of the identified prominent paths are being shared.

Intuitively, the method identifies the most prominent paths from the bottom to the top of the sparse flattened OCT fingerprint scan after processing with the blob-emphasizing DoG operator. The upward pass, Alg. 7.3, identifies the optimal paths from each node at the bottom of the scan to each node inside the scan, especially at the top of the scan. However, many of these paths share a sub-path, which fact would lead to multiple overlapping sub-optimal detections of the glands. The situation can be mitigated by another downward pass - Alg. 7.4. Alg. 7.4 ensures that only the optimal path from each group of paths that share a sub-path is selected. The weight of the optimal path is propagated as weight of the node, $M(N)$, to the bottom of the sparse DoG-processed flattened fingerprint volume. If a node, N, is not part of the optimal path in any of the sub-path-sharing groups, it's $M(N)$ is set to infinity and the node, N, is effectively discarded. Consequently, by simple analysis of the sparse volume at the bottom, it is possible to pick n nodes with smallest $M(N)$ and readily read-off the calculated sweat glands paths.

7.6 Results

Fig. 7.6 and 7.7 illustrates the flattened volume between the outer and inner fingerprint of a thumb and an index finger. Fig. 7.6a and 7.7a represents a

Algorithm 7.3: Upward pass of the multiple-source multiple-target shortest path graph algorithm for glands detection on the GPU

foreach *slice,* $S(x, y)$*, of the sparse representation of the DoG-filtered flattened OCT fingerprint volume,* $DoG(V_f)(x, y, z)$*, from the bottom to the top* **do**
  if *slice at the bottom* **then**
    Initialize the weight $W(N)$ of all nodes in the slice S to 0;
  else
    Initialize the weight $W(N)$ of all nodes in the slice S to infinity;
  Divide the slice, $S(x, y)$, into a grid, G, of rectangular GPU blocks, B (32x32);
  foreach *rectangular GPU block,* B*, in the grid,* G **do**
    Underneath the GPU block, B, define a sub-volume, $V_B(x, y, z)$, of size ($size(B)$ + $2span_L$) x ($size(B)$ + $2span_L$) x $span_D$, centered at the center of the block, B (Fig. 7.4);
    foreach *sub-slice,* $S_B(x, y)$*, of the defined sub-volume* $V_B(x, y, z)$ **do**
      pre-load the sub-slice $S_B(x, y)$ into the fast on-chip GPU shared memory;
      foreach *node,* N_B*, in the processed GPU block,* B **do**
        Define a sub-volume, V_N, of size ($2span_L$) x ($2span_L$) x $span_D$, centered underneath the node, N_B;
        Search the nodes in the sub-slice, S_B, inside the volume V_N, and a find a node, N_U, with minimum graph-distance, $W(N_U) + D(N_U, N_B)$;
        if $W(N_U) + D(N_U, N_B) < W(N_B)$ **then**
          Set $W(N_B)$ to $W(N_U) + D(N_U, N_B)$;
          Store the position of the minimum distance node, N_U, along with the GPU-block-node, N_B;

visualization the flattened OCT scanned data, V_f. Fig. 7.6b and Fig. 7.7b represents the sparse DoG processed data, $DoG(V_f)$, (see Alg. 7.2) that serve as an input to the graph-based glands detector (see Alg. 7.3, 7.4).

Visualizations of the results of the sweat glands detection (see Alg. 7.3, 7.4) in the the thumb and index finger are illustrated by Fig. 7.8 and 7.9. Results of detecting the first 100, 200 and 300 sweat glands are visualized.

7.6.1 Contrast and Other Issues

Correct functioning of the glands detection method depends on the assumption that the sweat glands are the most prominent features in the volume between the outer and inner fingerprint with highest contrast to the surrounding tissue compared to other features. However, in our dataset collected by the

Algorithm 7.4: Downward pass of the multiple-source multiple-target shortest path graph algorithm for glands detection on the GPU

```
1  foreach slice, S(x,y), of the sparse representation of the DoG-filtered
     flattened OCT fingerprint volume, DoG(V_f)(x,y,z), from the top to the
     bottom do
2      if slice at the top then
3          Initialize the weight M(N) of all nodes in the slice S to W(N);
4      else
5          Initialize the weight M(N) of all nodes in the slice S to infinity;
6      Divide the slice, S(x,y), into a grid, G, of rectangular GPU blocks,
         B (32x32);
7      foreach rectangular GPU block, B, in the grid, G do
8          Over the GPU block, B, define a sub-volume, V_B(x,y,z), of size
             (size(B) + 2span_L) x (size(B) + 2span_L) x span_D, centered at
             the center of the block, B (Fig. 7.4);
9          foreach sub-slice S_B(x,y) of the defined sub-volume V_B(x,y,z) do
10             pre-load the sub-slice S_B(x,y) into the fast on-chip GPU
                 shared memory;
11             foreach node, N_B, in the processed GPU block, B do
12                 Define a sub-volume, V_N, of size (2span_L) x (2span_L) x
                     span_D, centered over the node, N_B;
13                 Search the nodes in the sub-slice, S_B, inside the volume
                     V_N, and a find a node, N_U, with minimum weight
                     M(N_U) among the nodes that share a path with N_B;
14                 if M(N_U) < M(N_B) then
15                     Set M(N_B) to M(N_U);
16                     Store the position of the minimum weight node, N_U,
                         along with the GPU-block-node, N_B;
```

current version of the proposed OCT scanner this assumption is not fully met. The current version of the OCT scanner lacks adaptive contrast management that would adapt to the differences of reflective properties in fingers from different capture subjects. In addition, the contrast in the OCT scan currently depends significantly on the distance of the skin from the surface of the sensor - Fig. 7.6a, 7.7a. This dependency is non-linear in nature, possibly related to widening/weakening of the sample light beam with distance from the focal plane (sensor surface) and cannot be corrected for in software in a simple manner. In a significant percentage of cases, this issue causes the fingerprint pattern to be of higher contrast compared to the sweat glands in the parts of the fingerprint scanned closest to the scanner surface. The significance of the issue increases with decreasing distance to the sensor surface, as illustrated by Fig. 7.6a, 7.7a (We are limited regarding showing the effect on multiple cases by the sensitive nature of the biometric fingerprint data).

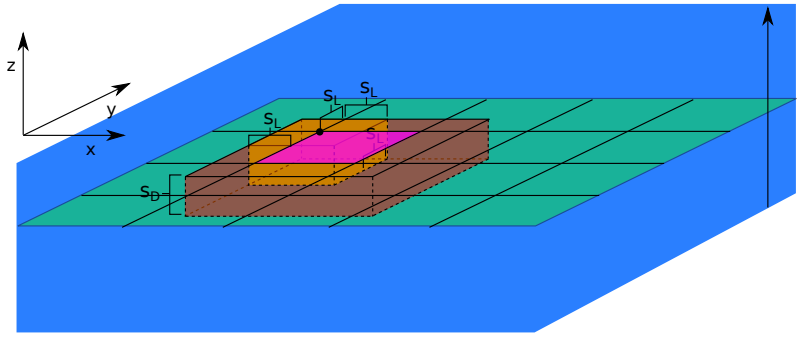

Figure 7.4: An iteration of the upward pass of the multiple-source multiple-target shortest path graph algorithm for glands detection on the GPU; Blue - the sparse representation of the DoG-filtered volume containing the flattened fingerprint - $DoG(V_f)(x, y, z)$; Green - a xy grid, G, (divided into GPU blocks 32x32) representing one iteration of the search for the nodes with minimum graph-distances from the nodes underneath; Orange - sub-volume, V_N, under a single node, N_B, that is being searched for the nodes, N_U, with minimum graph-distance from the node, $D(N_U, N_B)$; Red - a sub-volume, V_B, under a single GPU block, B, that is being buffered into the fast GPU shared memory for acceleration; Violet - a single GPU block, B

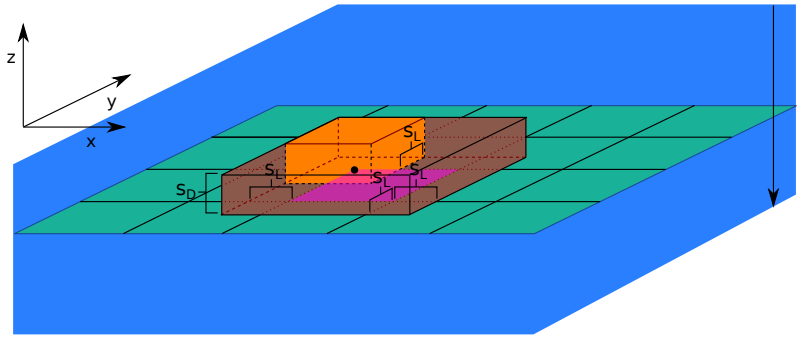

Figure 7.5: An iteration of the downward pass of the multiple-source multiple-target shortest path graph algorithm for glands detection; Blue - the sparse representation of the DoG-filtered volume containing the flattened fingerprint - $DoG(V_f)(x, y, z)$; Green - a xy grid, G, (divided into GPU blocks 32x32) representing one iteration of the search for the nodes that form an optimal path with the processed nodes on the plane; Orange - a sub-volume, V_N, over a single node, N_B, that is being searched for the nodes, N_U, that form an optimal path with the node, N_B; Red - a sub-volume, V_B, over a single GPU block, B, that is being buffered into the fast GPU shared memory for acceleration; Violet - a single GPU block, B

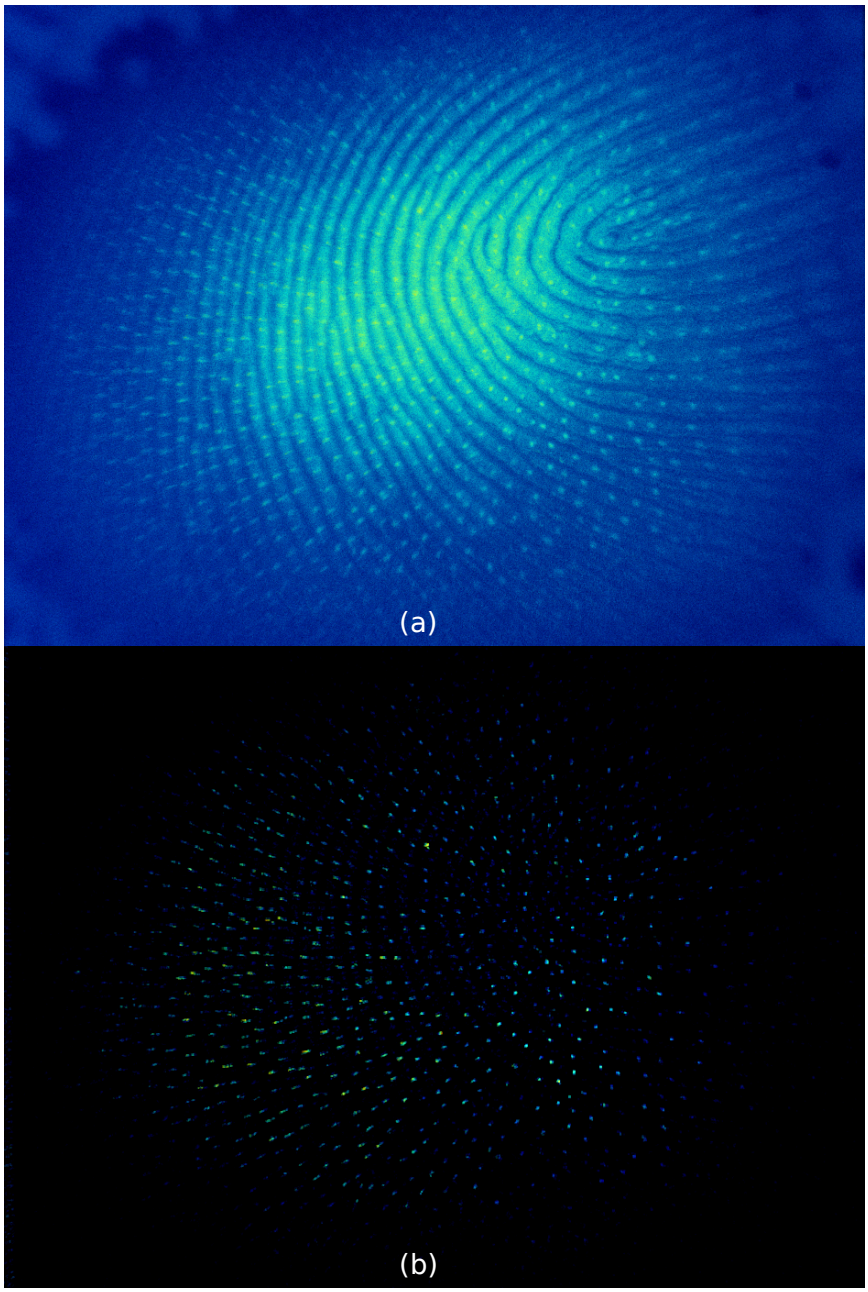

Figure 7.6: Top: Flattened middle layer of an OCT scanned thumb; Bottom: Processed by our sparse DoG approach (sweat glands emphasized)

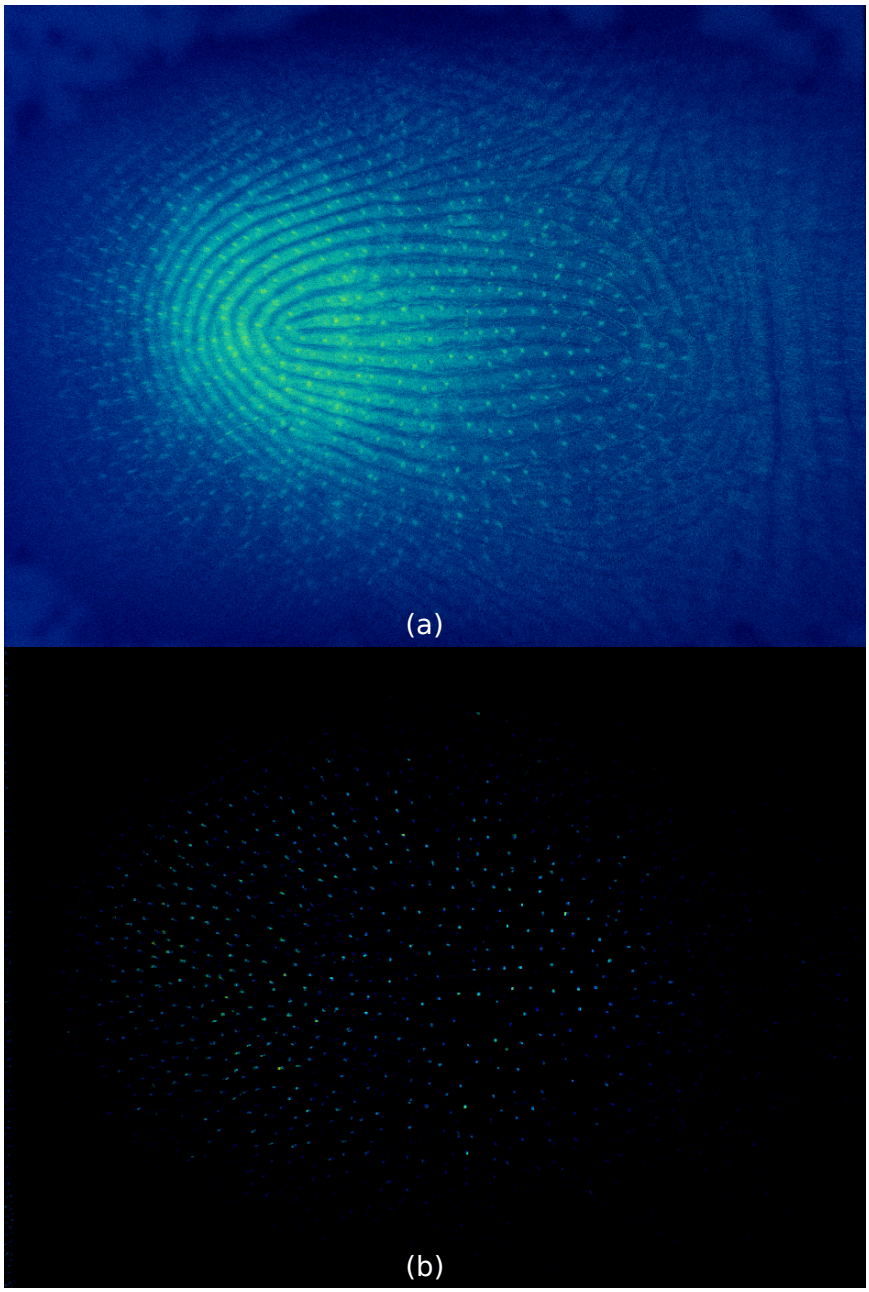

Figure 7.7: Top: Flattened middle layer of an OCT scanned index finger; Bottom: Processed by our sparse DoG approach (sweat glands emphasized)

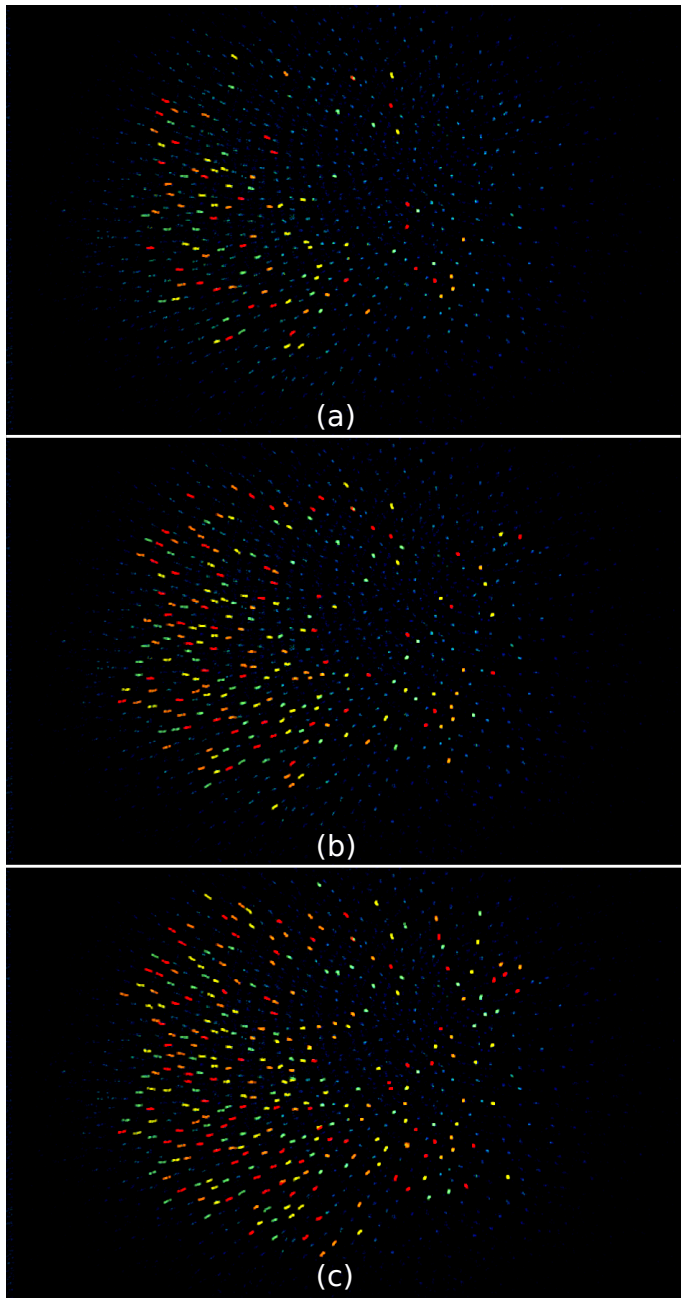

Figure 7.8: OCT scanned thumb; (a) First 100 sweat glands detections; (b) First 200 sweat glands detections; (c) First 300 sweat glands detections

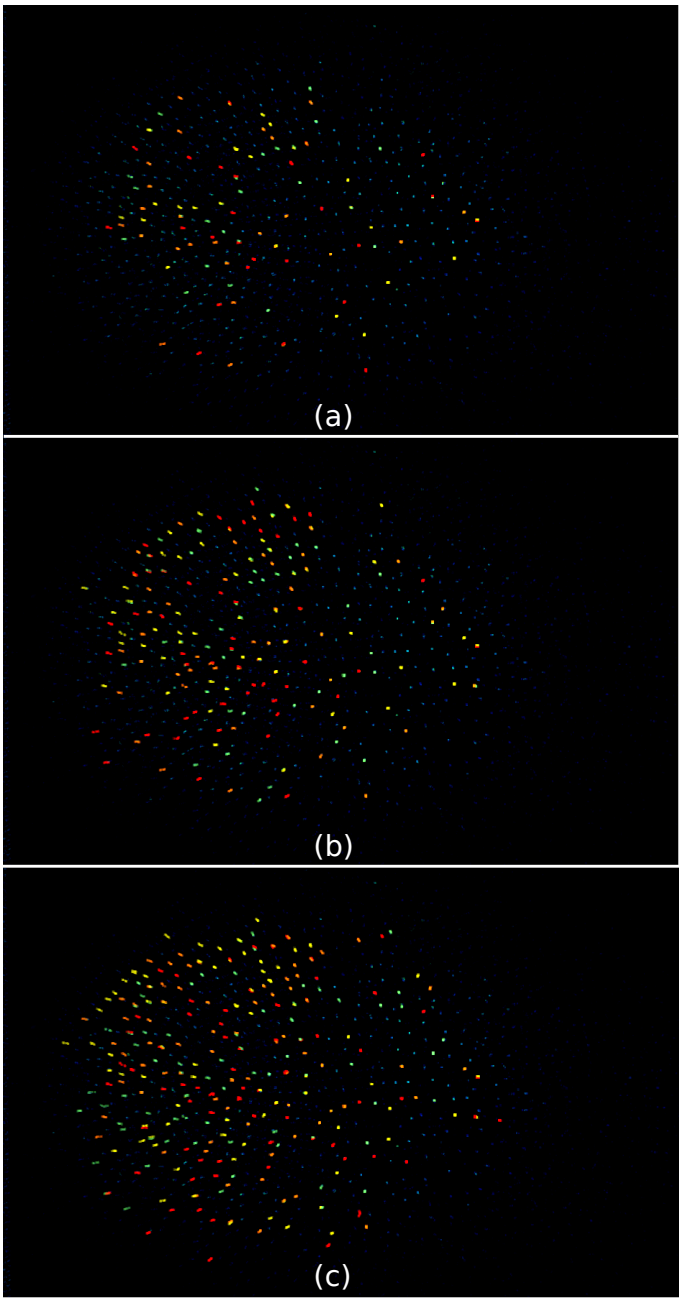

Figure 7.9: OCT scanned index finger; (a) First 100 sweat glands detections; (b) First 200 sweat glands detections; (c) First 300 sweat glands detections

A database-wide performance on the collected OCT fingerprint dataset described in previous chapters is shown by Tab. 7.1. The table shows the percentages of fingers where, among the first 100 sweat glands detections in a particular finger (correspondence of the automatic detections with real sweat glands has been checked manually):

- 80% or more sweat glands were correctly identified
- 50-80% of the sweat glands were correctly identified
- Sweat glands were the highest contrast, detectable, features in surrounding parts of the scan, but the method failed due to the above described contrast issue in the part closest to the sensor surface
- The sweat glands were not the highest contrast features anywhere in the scan or were not visible at all (dry, damaged tissue etc.)

The results are reported on a per finger as well as overall basis. The thumbs and index fingers clearly stand out as having the most clearly visible glands, while the little fingers were among the hardest to consistently find sweat glands in. Adaptive contrast management in the scanner, capable of mitigating the contrast issue, would clearly lead to significant improvement of the sweat glands detection performance.

Table 7.1: Sweat glands detection performance (by finger type and overall)

finger type	among 100 first gland detections 80%+ correct	among 100 first gland detections 50-80% correct	adaptive contrast issue	other issues
thumb	85 %	6 %	3 %	6 %
index	78 %	10 %	6 %	6 %
middle	69 %	10 %	12 %	9 %
ring	48 %	21 %	15 %	16 %
little	51 %	21 %	16 %	12 %
all fingers	66.4 %	13.8 %	10.1 %	9.7 %

7.6.2 Speed & Memory

The method runs on a GPU with 3GB of RAM, where 2GB are required for the OCT fingerprint scan and less than 700 MB for the processing buffers. The durations of the different stages of the sweat glands detection in a flattened OCT fingerprint scan are shown in Tab. 7.2.

Table 7.2: Duration of different stages of the glands detection pipeline on different NVIDIA GeForce GPU models (average over all scans in the dataset)

	GTX 980 4GB (ms)	GTX 780 3GB (ms)
3D DoG filtering	483.8	733.3
glands detection upward pass	40.7	54.5
glands detection downward pass	6.7	9.7

7.7 Conclusion and Future Work

Utilizing the single-pass approximate Gaussian filtering technique, proposed in Chapter 5, a novel, fast and memory efficient scheme for computation of 3D Difference of Gaussians (DoG) on CPUs as well as GPUs has been proposed that could find applications in medical imaging pipelines outside the narrow problem of detection of sweat glands in volumetric OCT fingerprint scans. The method allows for fast filter-size-independent calculation of 3D DoG with extra memory requirements representing only a small fraction of the size of the processed 3D volumetric data.

The 3D DoG technique has been used together with graph-based multiple-source multiple-target shortest path algorithm to identify sweat glands candidates as the most prominent paths between the outer fingerprint on the surface and the subsurface inner fingerprint. This can serve as a pre-processing step that greatly reduces the search space of possible positions and paths that the sweat glands can take in the significant amount of volumetric data representing the middle layer an OCT fingerprint scan. In the future work, the identified candidate sweat gland paths could be used for analysis of the structure along them in order to verify it as a genuine sweat gland or a false detection for the purposes of PAD.

The performance of the proposed sweat gland candidate detection pipeline currently suffers significantly from contrast issues caused by the lack of proper contrast management in the current version of the employed OCT fingerprint sensor prototype. The future work should focus on further examinations of the nature of the non-linear contrast issue and it's mitigation by the improvement of the OCT fingerprint sensor.

The sweat glands detection method itself could be probably improved by further adjustments of the distance function used as a measure in the graph-based sweat glands detector. In addition, the performance of the method could benefit from masking out the low quality areas and searching for the sweat glands only in selected areas of the OCT fingerprint scans, as opposed to the current entire-fingerprint operation.

Chapter 8

Conclusions and Future Work

In this research we focused on Optical Coherence Tomography (OCT) as a novel 3D scanning technology for fingerprint sensing. The OCT offers many advantages compared to standard 2D fingerprint sensing. The fingerprints can be scanned free-air, not pressed against a glass surface, which mitigates issues with dry, wet, greasy or too soft fingerprints. The OCT can also scan underneath the surface of the fingertip, offering great promise regarding robust detection of artefact fingerprints, due to its ability to spot the sub-surface inner fingerprint, sweat glands and other features.

Motivated by the many advantages of the OCT compared to standard 2D fingerprint sensors, we had to face significant challenges associated with processing of the large amounts of 3D volumetric data, as opposed to 2D scans, in a matter of seconds as required by many unsupervised scenarios such as border control.

The results in this thesis strongly suggest the following general conclusions regarding the main questions to be answered by this research:

- By utilizing massively-parallel GPU acceleration in combination with our novel fast filtering techniques, a reliable extraction of the outer fingerprints, as well as sub-surface inner fingerprints, from the volumetric OCT scans is possible in a matter of seconds, despite the very large data amounts.

- The sub-surface inner fingerprints are very consistently present in the population. The inner fingerprint is more likely to be of sufficient quality for fingerprint identification than the outer fingerprint, which fact offers a great promise of the OCT compared to standard 2D sensors that can acquire the surface outer fingerprint only.

- The sweat glands exhibit significant variations in the population regarding their amount, length, overall visibility in the scan and other properties, which fact poses extra challenges in their detection.

- Detection of the sweat glands in a matter of seconds is possible, by combination of our novel fast filtering techniques and GPU acceleration, but a reliable functionality of the pipeline, given the large variations of the sweat glands in the population, would require scans of higher quality.

- Novel fast approaches for filtering, edge and blob detection have been proposed, with a very limited memory footprint. The approaches are well-suited for GPUs and could find applications also outside the narrow scope of volumetric OCT fingerprinting.

8.1 Future work

The future work should focus both on improvements of the OCT fingerprint sensor prototype as well as the associated processing techniques.

The OCT sensor could be improved in terms of the scanning depth, allowing to scan more reliably even in the cases where the surface of the fingerprint has a strong curvature or the fingerprint is positioned sub-optimally. The contrast issues could be addressed by combination of improved adaptive management of the light beam and additional pre-processing. The scanning head should be further improved to better address the fingerprint shaking. The further efforts should also focus on miniaturization of the whole setup, by designing a specific-purpose electronics and replacing the large mirror galvanometer pair using a MEMS mirror solution.

Regarding the fingerprint extraction method, the detection of outer fingerprint could probably be somewhat improved using an approach based on multiple filter sizes.

Significant improvements of the sweat gland detection would probably require adaptive contrast adjustment to be implemented into the OCT fingerprint sensor, nevertheless, masking out the low quality areas or adjusting the distance function used in the sweat glands detection pipeline would probably lead to an improvement.

Chapter 9

References

[1] EU-project INGRESS. Available from: `http://www.ingress-project.eu/`. 25, 59

[2] ABHYANKAR, A., AND SCHUCKERS, S. Integrating a wavelet based perspiration liveness check with fingerprint recognition. *Pattern Recognition 42*, 3 (2009), 452–464. vii, 20

[3] ABHYANKAR, A., AND SCHUCKERS, S. Modular Decomposition of Fingerprint Time Series Captures for the Liveness Check. *International Journal of Computer and Electrical Engineering 2* (2010), 426–431. 21

[4] ANTONELLI, A., CAPPELLI, R., MAIO, D., AND MALTONI, D. Fake finger detection by skin distortion analysis. *IEEE Transactions on Information Forensics and Security 1*, 3 (2006), 360–373. 18, 31

[5] AUKSORIUS, E., AND BOCCARA, A. C. Fingerprint imaging from the inside of a finger with full-field optical coherence tomography. *Biomed. Opt. Express 6*, 11 (Nov 2015), 4465–4471. Available from: `http://www.osapublishing.org/boe/abstract.cfm?URI=boe-6-11-4465`. 25, 59, 62, 65

[6] AUKSORIUS, E., AND BOCCARA, A. C. Internal fingerprint imaging with visible light full-field optical coherence tomography. In *Biomedical Optics 2016* (2016), Optical Society of America. 25, 59

[7] BALDISSERRA, D., FRANCO, A., MAIO, D., AND MALTONI, D. Fake Fingerprint Detection by Odor Analysis. In *Advances in Biometrics*, vol. 3832 of *LNCS*. 2005, pp. 265–272. 22

[8] BHATIA, A., SNYDER, W., AND BILBRO, G. Stacked integral image. In *Robotics and Automation (ICRA), 2010 IEEE International Conference on* (May 2010), pp. 1530–1535. 79

[9] BIGGIO, B., AKHTAR, Z., FUMERA, G., MARCIALIS, G., AND ROLI, F. Security evaluation of biometric authentication systems under real spoofing attacks. *Biometrics, IET 1*, 1 (2012), 11–24. 11

[10] BIOMETRICS EVALUATION AND TESTING (BEAT). http://www.beat-eu.org/. 35

[11] BOSSEN, A., LEHMANN, R., AND MEIER, C. Internal Fingerprint Identification With Optical Coherence Tomography. *Photonics Technology Letters, IEEE 22*, 7 (2010), 507–509. 25

[12] BREITHAUPT, R., SOUSEDIK, C., AND MEISSNER, S. Full fingerprint scanner using optical coherence tomography. In *Biometrics and Forensics (IWBF), 2015 International Workshop on* (March 2015), pp. 1–6. viii, 3, 59, 60, 63, 65, 67, 68

[13] CANDES, E. J., AND DONOHO, D. L. Ridgelets: a key to higher-dimensional intermittency? *Philosophical Transactions of the London Royal Society 357* (1999), 2495–2509. 18

[14] CATANZARO, B., KELLER, A., AND GARLAND, M. A decomposition for in-place matrix transposition. In *Proceedings of the 19th ACM SIGPLAN Symposium on Principles and Practice of Parallel Programming* (New York, NY, USA, 2014), PPoPP '14, ACM, pp. 193–206. Available from: `http://doi.acm.org/10.1145/2555243.2555253`. 121

[15] CHANG, S., LARIN, K., MAO, Y., ALMUHTADI, W., AND FLUERARU, C. Fingerprint Spoof Detection By NIR Optical Analysis. In *State of the art in Biometrics*, J. Yang, Ed. 2011. 23, 24

[16] CHANG, S., SHERIF, S., AND FLUERARU, C. Large area full-field optical coherence tomography. In *Photonics North* (2006), vol. 6343. 37

[17] CHEN, J., HUERTAS, A., AND MEDIONI, G. Fast convolution with laplacian-of-gaussian masks. *Pattern Analysis and Machine Intelligence, IEEE Transactions on PAMI-9*, 4 (July 1987), 584–590. 79

[18] CHENG, Y., AND LARIN, K. In Vivo Two- and Three-Dimensional Imaging of Artificial and Real Fingerprints With Optical Coherence Tomography. *Photonics Technology Letters, IEEE 19*, 20 (2007), 1634–1636. 24

[19] CHENG, Y., AND LARIN, K. V. Artificial fingerprint recognition by using optical coherence tomography with autocorrelation analysis. *Appl. Opt. 45*, 36 (2006), 9238–9245. 24

[20] CHOI, H., KANG, R., CHOI, K., AND KIM, J. Aliveness Detection of Fingerprints using Multiple Static Features. In *World Academy of Science, Engineering and Technology* (July 2007), vol. 22. 16

[21] CHOI, S., KIM, T., AND YU, W. Performance evaluation of ransac family. In *Proc. BMVC* (2009), pp. 81.1–81.12. 48

[22] CIMALLA, P., WALTHER, J., MEHNER, M., CUEVAS, M., AND KOCH, E. Simultaneous dual-band optical coherence tomography in the spectral domain for high resolution in vivo imaging. *Opt. Express 17*, 22 (2009), 19486–19500. 24

[23] COLI, P., MARCIALIS, G., AND ROLI, F. Power spectrum-based fingerprint vitality detection. In *IEEE Workshop on Automatic Identification Advanced Technologies* (2007), pp. 169–173. 18, 30

[24] COLI, P., MARCIALIS, G. L., AND ROLI, F. Vitality Detection from Fingerprint Images: A Critical Survey. In *Proceedings of the international conference on Advances in Biometrics (ICB '07)* (Berlin, Heidelberg, 2007), pp. 722–731. 14, 15

[25] COLI, P., MARCIALIS, G. L., AND ROLI, F. Fingerprint silicon replicas: static and dynamic features for vitality detection using an optical capture device. *International Journal of Image and Graphics 8* (2008), 495–512. 30

[26] DARLOW, L. N., AND CONNAN, J. Efficient internal and surface fingerprint extraction and blending using optical coherence tomography. *Appl. Opt. 54*, 31 (Nov 2015), 9258–9268. Available from: `http://ao.osa.org/abstract.cfm?URI=ao-54-31-9258`. 25, 94

[27] DARLOW, L. N., CONNAN, J., AND AKHOURY, S. S. Internal fingerprint zone detection in optical coherence tomography fingertip scans. *Journal of Electronic Imaging 24*, 2 (2015), 023027. Available from: `http://dx.doi.org/10.1117/1.JEI.24.2.023027`. 25, 94, 95

[28] DARLOW, L. N., CONNAN, J., AND SINGH, A. Performance analysis of a hybrid fingerprint extracted from optical coherence tomography fingertip scans. In *2016 International Conference on Biometrics (ICB)* (June 2016), pp. 1–8. ix, 25, 93, 94, 108, 109

[29] DECANN, B., TAN, B., AND SCHUCKERS, S. A Novel Region Based Liveness Detection Approach for Fingerprint Scanners. In *Third International Conference on Advances in Biometrics (ICB '09)* (Berlin, Heidelberg, 2009), pp. 627–636. 20, 31

[30] DERAKHSHANI, R., SCHUCKERS, S., HORNAK, L. A., AND O'GORMAN, L. Determination of vitality from a non-invasive biomedical measurement for use in fingerprint scanners. *Pattern Recognition 36*, 2 (2003), 383–396. 19, 20

[31] DERICHE, R. Fast algorithms for low-level vision. In *Pattern Recognition, 1988., 9th International Conference on* (Nov 1988), pp. 434–438 vol.1. 79

[32] DERICHE, R. Recursively implementating the Gaussian and its derivatives. Research Report RR-1893, 1993. Available from: https://hal.inria.fr/inria-00074778. 79

[33] DIJKSTRA, E. W. A note on two problems in connexion with graphs. *Numer. Math. 1*, 1 (Dec. 1959), 269–271. Available from: http://dx.doi.org/10.1007/BF01386390. 122

[34] DRAHANSKY, M., NOTZEL, R., AND FUNK, W. Liveness Detection based on Fine Movements of the Fingertip Surface. In *IEEE Information Assurance Workshop* (2006), pp. 42–47. 23

[35] ELBOHER, E., AND WERMAN, M. Efficient and accurate gaussian image filtering using running sums. In *Intelligent Systems Design and Applications (ISDA), 2012 12th International Conference on* (Nov 2012), pp. 897–902. 79, 85

[36] ESPINOZA, M., AND CHAMPOD, C. Risk evaluation for spoofing against a sensor supplied with liveness detection. *Forensic Science International 204*, 1–3 (2011), 162–168. vii, 7, 11, 13

[37] ESPINOZA, M., AND CHAMPOD, C. Using the Number of Pores on Fingerprint Images to Detect Spoofing Attacks. In *International Conference on Hand-Based Biometrics (ICHB)* (2011), pp. 1–5. 11, 15, 31

[38] ESPINOZA, M., CHAMPOD, C., AND MARGOT, P. Vulnerabilities of fingerprint reader to fake fingerprints attacks. *Forensic Science International 204*, 1–3 (2011), 41–49. vii, 7, 11, 13

[39] FANN. Fast artificial neural network library. Available from: http://leenissen.dk/fann/wp/. 49

[40] GALBALLY, J., ALONSO-FERNANDEZ, F., FIERREZ, J., AND ORTEGA-GARCIA, J. A high performance fingerprint liveness detection method based on quality related features. *Future Generation Computer Systems 28*, 1 (2012), 311–321. 18, 27, 31

[41] GALBALLY, J., FIERREZ, J., ALONSO-FERNANDEZ, F., AND MARTINEZ-DIAZ, M. Evaluation of direct attacks to fingerprint verification systems. *Telecommunication Systems 47* (2011), 243–254. vii, 7, 11, 13

[42] GETREUER, P. A Survey of Gaussian Convolution Algorithms. *Image Processing On Line 3* (2013), 286–310. 79

[43] GHIANI, L., DENTI, P., AND MARCIALIS, G. Experimental Results on Fingerprint Liveness Detection. In *Articulated Motion and Deformable Objects*, vol. 7378 of *LNCS*. 2012, pp. 210–218. xi, 30, 31

[44] GHIANI, L., YAMBAY, D., MURA, V., TOCCO, S., MARCIALIS, G., ROLI, F., AND SCHUCKERS, S. LivDet 2013 Fingerprint Liveness Detection Competition 2013. In *6th IAPR International Conference on Biometrics (ICB)* (2013). 31, 34

[45] GWOSDEK, P., GREWENIG, S., BRUHN, A., AND WEICKERT, J. Theoretical foundations of gaussian convolution by extended box filtering. In *Scale Space and Variational Methods in Computer Vision*, A. Bruckstein, B. ter Haar Romeny, A. Bronstein, and M. Bronstein, Eds., vol. 6667 of *Lecture Notes in Computer Science*. Springer Berlin Heidelberg, 2012, pp. 447–458. Available from: http://dx.doi.org/10.1007/978-3-642-24785-9_38. 79

[46] HAN, Y., RYU, C., MOON, J., KIM, H., AND CHOI, H. A Study on Evaluating the Uniqueness of Fingerprints Using Statistical Analysis. In *Information Security and Cryptology – ICISC 2004*, vol. 3506 of *LNCS*. 2005, pp. 467–477. 7

[47] HECKBERT, P. S. Filtering by repeated integration. In *Proceedings of the 13th Annual Conference on Computer Graphics and Interactive Techniques* (New York, NY, USA, 1986), SIGGRAPH '86, ACM, pp. 315–321. Available from: http://doi.acm.org/10.1145/15922.15921. 79

[48] HENGFOSS, C., KULCKE, A., MULL, G., EDLER, C., PÜSCHEL, K., AND JOPP, E. Dynamic liveness and forgeries detection of the finger surface on the basis of spectroscopy in the 400-1650nm region. *Forensic Science International 212*, 1–3 (2011), 61–68. vii, 22, 23

[49] HUSSEIN, M., PORIKLI, F., AND DAVIS, L. Kernel integral images: A framework for fast non-uniform filtering. In *Computer Vision and Pattern Recognition, 2008. CVPR 2008. IEEE Conference on* (June 2008), pp. 1–8. 79

[50] INTERNATIONAL ORGANIZATION FOR STANDARDIZATION, ISO/IEC 5TH WD 30107. Information Technology - Biometrics - Presentation attack detection, 2013. 14, 25

[51] ISO-IEC-29794-1. Biometric sample quality, 2009. 53, 57

[52] ISO/IEC 2382-37. Information technology – Vocabulary – Part 37: Biometrics, 2012. 110

[53] JAIN, A. K., ARORA, S. S., CAO, K., BEST-ROWDEN, L., AND BHATNAGAR, A. Fingerprint recognition of young children. *IEEE Transactions on Information Forensics and Security 12*, 7 (July 2017), 1501–1514. 1

[54] JIA, J., AND CAI, L. Fake Finger Detection Based on Time-Series Fingerprint Image Analysis. In *Advanced Intelligent Computing Theories and Applications. With Aspects of Theoretical and Methodological Issues*, vol. 4681 of *LNCS*. 2007, pp. 1140–1150. 20, 31

[55] JIA, J., CAI, L., ZHANG, K., AND CHEN, D. A New Approach to Fake Finger Detection Based on Skin Elasticity Analysis. In *ICB* (2007), pp. 309–318. vii, 19, 31

[56] JIN, C., LI, S., KIM, H., AND PARK, E. Fingerprint Liveness Detection Based on Multiple Image Quality Features. In *Information Security Applications*, vol. 6513 of *LNCS*. 2011, pp. 281–291. 16, 17

[57] KANG, H., LEE, B., KIM, H., SHIN, D., AND KIM, J. A Study on Performance Evaluation of the Liveness Detection for Various Fingerprint Sensor Modules. In *Knowledge-Based Intelligent Information and Engineering Systems*, vol. 2774 of *LNCS*. 2003, pp. 1245–1253. vii, 7, 11, 13

[58] KHUTLANG, R., KHANYILE, N. P., MAKINANA, S., AND NELWAMONDO, F. V. High resolution feature extraction from optical coherence tomography acquired internal fingerprint. In *2016 17th IEEE/ACIS International Conference on Software Engineering, Artificial Intelligence, Networking and Parallel/Distributed Computing (SNPD)* (May 2016), pp. 637–641. 25

[59] KODA, Y., HIGUCHI, T., AND JAIN, A. K. Advances in capturing child fingerprints: A high resolution cmos image sensor with sldr method. In *2016 International Conference of the Biometrics Special Interest Group (BIOSIG)* (Sept 2016), pp. 1–4. 1

[60] LEE, C., LEE, S., AND KIM, J. A Study of Touchless Fingerprint Recognition System. In *Structural, Syntactic, and Statistical Pattern Recognition*, vol. 4109 of *LNCS*. Springer Berlin Heidelberg, 2006, pp. 358–365. Available from: `http://dx.doi.org/10.1007/11815921_39`. 8

[61] LIU, M., AND BUMA, T. Biometric Mapping of Fingertip Eccrine Glands With Optical Coherence Tomography. *Photonics Technology Letters, IEEE 22*, 22 (Nov 2010), 1677–1679. 25

[62] LUMIDIGM. http://www.lumidigm.com/technology/. 23

[63] MALTONI, D., MAIO, D., JAIN, A. K., AND PRABHAKAR, S. *Handbook of Fingerprint Recognition*, 2nd ed. Springer London, 2009, ch. 9.5, pp. 386–391. Available from: `http://dx.doi.org/10.1007/978-1-84882-254-2_9`. 9, 10, 15

[64] MALTONI, D., MAIO, D., JAIN, A. K., AND PRABHAKAR, S. *Handbook of Fingerprint Recognition*, 2nd ed. 2009. 53

[65] MANIVANAN, N., MEMON, S., AND BALACHANDRAN, W. Automatic detection of active sweat pores of fingerprint using highpass and correlation filtering. *Electronics Letters 46*, 18 (2010), 1268–1269. 16

[66] MARASCO, E., AND SANSONE, C. An anti-spoofing technique using multiple textural features in fingerprint scanners. In *IEEE Workshop on Biometric Measurements and Systems for Security and Medical Applications (BIOMS)* (2010), pp. 8–14. 16, 17, 31

[67] MARASCO, E., AND SANSONE, C. Combining perspiration- and morphology-based static features for fingerprint liveness detection. *Pattern Recognition Letters 33*, 9 (2012), 1148–1156. vii, 16, 17, 31

[68] MARCIALIS, G., GHIANI, L., VETTER, K., MORGENEIER, D., AND ROLI, F. Large Scale Experiments on Fingerprint Liveness Detection. In *Structural, Syntactic, and Statistical Pattern Recognition*, vol. 7626 of *LNCS*. 2012, pp. 501–509. 30

[69] MARCIALIS, G., LEWICKE, A., TAN, B., COLI, P., GRIMBERG, D., CONGIU, A., TIDU, A., ROLI, F., AND SCHUCKERS, S. First International Fingerprint Liveness Detection Competition—LivDet 2009. In *Image Analysis and Processing – ICIAP 2009*, vol. 5716 of *LNCS*. 2009, pp. 12–23. xi, 26, 27, 28, 31, 34

[70] MARCIALIS, G., ROLI, F., AND TIDU, A. Analysis of Fingerprint Pores for Vitality Detection. In *20th International Conference on Pattern Recognition (ICPR)* (2010), pp. 1289–1292. 21, 30

[71] MARQUARDT, D. W. An Algorithm for Least-Squares Estimation of Nonlinear Parameters. *SIAM Journal on Applied Mathematics 11*, 2 (1963), 431–441. 48

[72] MARTINSEN, O., CLAUSEN, S., NYSAETHER, J., AND GRIMNES, S. Utilizing Characteristic Electrical Properties of the Epidermal Skin Layers to Detect Fake Fingers in Biometric Fingerprint Systems - A Pilot Study. *IEEE Transactions on Biomedical Engineering 54*, 5 (2007), 891–894. 24

[73] MATSUMOTO, T., MATSUMOTO, H., YAMADA, K., AND HOSHINO, S. Impact of artificial "gummy" fingers on fingerprint systems. In *SPIE 4677, Optical Security and Counterfeit Deterrence Techniques IV* (2002), vol. 4677, pp. 275–289. vii, 7, 11, 13

[74] MEISSNER, S., BREITHAUPT, R., AND KOCH, E. Defense of fake fingerprint attacks using a swept source laser optical coherence tomography setup. In *Proc. SPIE, Frontiers in Ultrafast Optics: Biomedical, Scientific, and Industrial Applications* (2013), vol. 8611. 25, 59, 62, 93

[75] MEISSNER, S., BREITHAUPT, R., AND KOCH, E. Fingerprint fake detection by optical coherence tomography. In *SPIE 8571, Optical Coherence Tomography and Coherence Domain Optical Methods in Biomedicine XVII* (2013), vol. 8571. 34, 50

[76] MEISSNER, S., BREITHAUPT, R., AND KOCH, E. Fingerprint fake detection by optical coherence tomography, 2013. Available from: `http://dx.doi.org/10.1117/12.1000091`. 59, 62

[77] MEMON, S., MANIVANNAN, N., AND BALACHANDRAN, W. Active pore detection for liveness in fingerprint identification system. In *Telecommunications Forum (TELFOR), 2011 19th* (2011), pp. 619–622. 21

[78] MEMON, S., SEPASIAN, M., AND BALACHANDRAN, W. Review of finger print sensing technologies. In *IEEE International Multitopic Conference (INMIC)* (2008), pp. 226–231. vii, xi, 9, 10, 11, 12

[79] MENRATH, M. Fingerprint with OCT. Master's thesis, Fern-Universität Hagen in Cooperation with Bundesamt für Sicherheit in der Informationstechnik (BSI), 2011. 25, 38, 46

[80] MOON, Y., CHEN, J., CHAN, K., SO, K., AND WOO, K. Wavelet based fingerprint liveness detection. *Electronics Letters 41*, 20 (2005), 1112–1113. 17

[81] MURA, V., GHIANI, L., MARCIALIS, G. L., ROLI, F., YAMBAY, D. A., AND SCHUCKERS, S. A. Livdet 2015 fingerprint liveness detection competition 2015. In *Biometrics Theory, Applications and Systems (BTAS), 2015 IEEE 7th International Conference on* (Sept 2015), pp. 1–6. xi, 1, 31, 32, 33, 34

[82] NASIRI-AVANAKI, M.-R., MEADWAY, A., BRADU, A., KHOSHKI, R. M., HOJJATOLESLAMI, A., AND PODOLEANU, A. G. Anti-Spoof Reliable Biometry of Fingerprints Using En-Face Optical Coherence Tomography. *Optics and Photonics Journal 1*, 3 (2011), 91–96. 25

[83] NIKAM, S., AND AGARWAL, S. Fingerprint Liveness Detection Using Curvelet Energy and Co-Occurrence Signatures. In *Fifth International Conference on Computer Graphics, Imaging and Visualisation (CGIV '08)* (2008), pp. 217–222. 18, 30, 31

[84] NIKAM, S., AND AGARWAL, S. Gabor Filter-Based Fingerprint Antispoofing. In *Advanced Concepts for Intelligent Vision Systems*, vol. 5259 of *LNCS*. 2008, pp. 1103–1114. 18, 31

[85] NIKAM, S., AND AGARWAL, S. Texture and Wavelet-Based Spoof Fingerprint Detection for Fingerprint Biometric Systems. In *First International Conference on Emerging Trends in Engineering and Technology (ICETET '08)* (2008), pp. 675–680. 18, 30, 31

[86] NIKAM, S., AND AGARWAL, S. Wavelet energy signature and GLCM features-based fingerprint anti-spoofing. In *International Conference on Wavelet Analysis and Pattern Recognition (ICWAPR '08)* (2008), vol. 2, pp. 717–723. 18, 31

[87] NIKAM, S. B., AND AGARWAL, S. Ridgelet-based fake fingerprint detection. *Neurocomputing 72*, 10–12 (2009), 2491–2506. 18, 31

[88] NIKAM, S. B., AND AGARWAL, S. Wavelet-based multiresolution analysis of ridges for fingerprint liveness detection. *Int. J. Inf. Comput. Secur. 3*, 1 (June 2009), 1–46. 21, 31

[89] OCT-FINGER PROJECT. Bundesamt für Sicherheit in der Informationstechnik (BSI), Germany, 2010. 38, 39

[90] PARTHASARADHI, S., DERAKHSHANI, R., HORNAK, L., AND SCHUCKERS, S. Time-series detection of perspiration as a liveness test in fingerprint devices. *IEEE Transactions on Systems, Man, and Cybernetics, Part C: Applications and Reviews 35*, 3 (2005), 335–343. 20

[91] PEREIRA, L., PINHEIRO, H., CAVALCANTI, G., AND REN, T. I. Spatial surface coarseness analysis: technique for fingerprint spoof detection. *Electronics Letters 49*, 4 (2013), 260–261. 17

[92] PEREIRA, L., PINHEIRO, H., SILVA, J., SILVA, A., PINA, T., CAVALCANTI, G., REN, T. I., AND DE OLIVEIRA, J. A fingerprint spoof detection based on MLP and SVM. In *International Joint Conference on Neural Networks (IJCNN)* (2012), pp. 1–7. 18, 31

[93] PETERSON, L. E., AND LARIN, K. V. Image classification of artificial fingerprints using Gabor wavelet filters, self-organising maps and Hermite/Laguerre neural networks. *International Journal of Knowledge Engineering and Soft Data Paradigms 1*, 3 (Oct. 2009), 239–256. 24

[94] REDDY, P., KUMAR, A., RAHMAN, S., AND MUNDRA, T. A New Antispoofing Approach for Biometric Devices. *IEEE Transactions on Biomedical Circuits and Systems 2*, 4 (2008), 328–337. 22

[95] ROWE, R. K., NIXON, K. A., AND BUTLER, P. W. Multispectral Fingerprint Image Acquisition. In *Advances in Biometrics*, N. Ratha and V. Govindaraju, Eds. Springer London, 2008, pp. 3–23. Available from: `http://dx.doi.org/10.1007/978-1-84628-921-7_1`. vii, xi, 9, 10, 12, 22, 23

[96] SATO, N., MACHIDA, K., MORIMURA, H., SHIGEMATSU, S., KUDOU, K., YANO, M., AND KYURAGI, H. MEMS fingerprint sensor immune to various finger surface conditions. *IEEE Transactions on Electron Devices 50*, 4 (2003), 1109–1116. vii, xi, 9, 10, 12

[97] SEPASIAN, M., MARES, C., AND BALACHANDRAN, W. Vitality detection in fingerprint identification. *WSEAS Trans. Info. Sci. and App. 7*, 4 (Apr. 2010), 498–507. 32

[98] SHIMAMURA, T., MORIMURA, H., SHIMOYAMA, N., SAKATA, T., SHIGEMATSU, S., MACHIDA, K., AND NAKANISHI, M. Impedance-Sensing Circuit Techniques for Integration of a Fraud Detection Function Into a Capacitive Fingerprint Sensor. *Sensors Journal, IEEE 12*, 5 (2012), 1393–1401. 24

[99] SOUSEDIK, C., AND BREITHAUPT, R. Full-fingerprint volumetric subsurface imaging using fourier-domain optical coherence tomography. In *Biometrics and Forensics (IWBF), 2017 International Workshop on* (2017). viii, 59, 63, 64, 94

[100] SOUSEDIK, C., BREITHAUPT, R., AND BOURS, P. Classification of fingerprints captured using optical coherence tomography. In *Scandinavian Conference on Image Analysis (SCIA), 2017* (2017). 93

[101] SOUSEDIK, C., BREITHAUPT, R., AND BUSCH, C. Volumetric fingerprint data analysis using Optical Coherence Tomography. In *International Conference of the Biometrics Special Interest Group (BIOSIG)* (2013), p. 16. vii, 16, 37, 46

[102] SOUSEDIK, C., AND BUSCH, C. Presentation attack detection methods for fingerprint recognition systems: a survey. *IET Biometrics 3*, 4 (2014), 219–233. 1, 2, 7

[103] SOUSEDIK, C., AND BUSCH, C. Quality of fingerprint scans captured using optical coherence tomography. In *IEEE International Joint Conference on Biometrics* (Sept 2014), pp. 1–8. 37

[104] TAN, B., AND SCHUCKERS, S. Liveness Detection for Fingerprint Scanners Based on the Statistics of Wavelet Signal Processing. In *Computer Vision and Pattern Recognition Workshop (CVPRW '06)* (2006), p. 26. 17, 30

[105] TAN, B., AND SCHUCKERS, S. New approach for liveness detection in fingerprint scanners based on valley noise analysis. *Journal of Electronic Imaging 17*, 1 (2008), 011009–011009–9. 16, 30, 31

[106] TAN, B., AND SCHUCKERS, S. Spoofing protection for fingerprint scanner by fusing ridge signal and valley noise. *Pattern Recognition 43*, 8 (2010), 2845–2857. 17, 31

[107] TRUSTED BIOMETRICS UNDER SPOOFING ATTACKS (TABULA RASA). http://www.tabularasa-euproject.org/. 35

[108] VAN DER PUTTE, T., AND KEUNING, J. Biometrical fingerprint recognition: don't get your fingers burned. In *IFIP TC8/WG8.8, 4th Working Confeference on Smart Card Research and Advanced Applications* (Norwell, MA, USA, 2000), pp. 289–303. vii, 7, 11, 13

[109] VAN VLIET, L., YOUNG, I., AND VERBEEK, P. Recursive gaussian derivative filters. In *Pattern Recognition, 1998. Proceedings. Fourteenth International Conference on* (Aug 1998), vol. 1, pp. 509–514 vol.1. 79

[110] WELLS, W. M. Efficient synthesis of gaussian filters by cascaded uniform filters. *Pattern Analysis and Machine Intelligence, IEEE Transactions on PAMI-8*, 2 (March 1986), 234–239. 79

[111] WIEHE, A., SØNDROL, T., OLSEN, O., AND SKARDERUD, F. Attacking Fingerprint Sensors. Tech. rep., NISlab/Gjovik Univ. College, Dec. 2004. vii, 7, 11, 12, 13

[112] YAMBAY, D., GHIANI, L., DENTI, P., MARCIALIS, G., ROLI, F., AND SCHUCKERS, S. LivDet 2011 - Fingerprint liveness detection competition 2011. In *5th IAPR International Conference on Biometrics (ICB)* (2012), pp. 208–215. xi, 11, 27, 28, 29, 31, 34

[113] YAU, W.-Y., TRAN, H.-L., AND TEOH, E.-K. Fake finger detection using an electrotactile display system. In *10th International Conference on Control, Automation, Robotics and Vision (ICARCV 2008)* (2008), pp. 962–966. 21

[114] YOUNG, I. T., AND VAN VLIET, L. J. Recursive implementation of the Gaussian filter. *Signal Processing 44*, 2 (1995), 139151. Available from: `http://www.sciencedirect.com/science/article/pii/016516849500020E`. 79, 85

[115] ZHANG, Y., TIAN, J., CHEN, X., YANG, X., AND SHI, P. Fake Finger Detection Based on Thin-Plate Spline Distortion Model. In *Advances in Biometrics*, vol. 4642 of *LNCS*. 2007, pp. 742–749. 19, 31

[116] ZWIESELE, A., MUNDE, A., BUSCH, C., AND DAUM, H. BioIS study. Comparative study of biometric identification systems. In *34th Annual International Carnahan Conference on Security Technology* (2000), pp. 60–63. 7